Open-path and fiber-based Cavity Ringdown Spectroscopy

Daniel E. Vogler

Diss. ETH No. 16278

Open-path and fiber-based Cavity Ringdown Spectroscopy

A dissertation submitted to the
SWISS FEDERAL INSTITUTE OF TECHNOLOGY
ZURICH

for the degree of
Doctor of Natural Sciences

presented by

DANIEL EDGAR VOGLER

Dipl. Phys., ETH Zürich
born on the 27th February 1975
citizen of Lungern, Obwalden

accepted on the recommendation of

Prof. Dr. M. W. Sigrist, examiner
Prof. Dr. U. Keller, co-examiner
Dr. H. Brändle, co-examiner

2005

Dedicated to my family

Contents

Abstract

This thesis concerns the use of the cavity ringdown technique in the near-infrared range. The cavity ringdown method is an extremely precise spectroscopic technique which determines the light intensity decay time within a cavity formed by highly-reflective dielectric mirrors. Measurements of acetylene impurities in pure ethylene gas and the determination of optical losses in fiber cavities by the cavity ringdown technique are the content of this thesis.

For the production of polymers, high-purity ethylene gas is required. In order to detect smallest concentrations of impurities in ethylene, a complete cavity ringdown setup was constructed and the corresponding software for the data analysis was developed. The setup is based on a continuous-wave near-infrared external cavity diode laser, an acousto-optic modulator and a cavity whose length can be swept in the nanometer range by a piezo-electric transducer. A minimum detectable absorption coefficient of $6.2 \cdot 10^{-6}$ m^{-1} (SNR = 3) could be achieved. This corresponds to an acetylene concentration of 67 ppbV in synthetic air at 100 mbar gas pressure and at a wavelength of 1530 nm. Smallest acetylene concentrations in a gas flow configuration could also be analyzed successfully at the same wavelength and a detection limit of 460 ppbV in ethylene was measured at 20 mbar. Furthermore, a linear dependence of the absorption coefficient on the acetylene concentration was found. The cavity ringdown setup was also successfully applied to the determination of isotope ratios. As example, an isotope ratio of $^{13}C^{12}CH_2$ to $^{12}C_2H_2$ of acetylene was determined in agreement with the natural abundance of 2.47 ± 0.13 % ratio.

The cavity ringdown technique was implemented in silica-based single-mode fibers for the first time by our group. Thereby, facets of fiber connectors were coated with dielectric mirrors in order to form the cavity within the fiber. This way, minute bending losses in fibers were determined. The experimental results were compared with values based on a theoretical model yielding excellent agreement. Bending loss modulation with respect to the curvature radius of the fiber predicted by the model could be verified experimentally. A detection limit of $1.72 \cdot 10^{-3}$ dB per cavity pass was achieved in a 10 m-long fiber cavity. Compared to bend insensitive fibers with a loss < 0.05 dB for 30 turns around a 20 mm thick cylinder, this limit is one order of magnitude smaller. Furthermore, the fiber cavity ringdown scheme was successfully used for the measurement of hydrogen diffusing in or out of the fiber cavity. Thereby, a hydrogen saturated fiber cavity showed an additional loss of 1.2 dB/km at 1586 nm. A theoretical consideration confirmed the temporal evolution of the measured losses in a fiber cavity during the diffusion process. In addition, the diffusion constant of hydrogen in silica could be evaluated experimentally as $D_{H_2-silica} = (3.02 \pm 0.07) \cdot 10^{-15}$ m^2/s at 30° C in agreement with diffusion constants of hydrogen in silica found in literature.

This thesis starts with a general overview of spectroscopy and concerns theoretical and experimental considerations of one particularly spectroscopic method, namely the cavity ringdown technique. A short theoretical treatment of the cavity ringdown method is given in chapter two whereas the third chapter describes our near-infrared based, open-path cavity ringdown experiment in detail. This chapter also depicts and discusses results of measurements accomplished. Furthermore, chapter four introduces the newly developed fiber cavity ringdown technique accompanied with the presentation of loss measurements in bent fibers and measurements of hydrogen diffusion in or out of a fiber cavity. Finally, the thesis closes with a conclusion and an outlook.

Zusammenfassung

Die vorliegende Arbeit befasst sich mit der Cavity Ringdown Technik im nahen Infrarotbereich. Die Cavity Ringdown Methode ist eine sehr präzise spektroskopische Messtechnik, die auf der Bestimmung der Lichtintensitätzerfallszeit innerhalb einer Kavität beruht. Die Kavität wird dabei von hochreflektierenden dielektrischen Spiegeln geformt. Die Messung von Acetylenverunreinigungen in reinem Ethylengas und die Bestimmung von optischen Verlusten in Glasfasern mittels der Cavity Ringdown Methode bilden den Inhalt dieser Arbeit.

Für die industrielle Herstellung von Polymeren wird reinstes Ethylengas benötigt. Um kleinste Konzentrationen von Verunreinigungen, insbesondere von Acetylen, in Ethylen messen zu können, wurde ein vollständiges Cavity Ringdown System aufgebaut und die entsprechende Auswertungssoftware entwickelt. Das System basiert auf einem kontinuierlichen, nah-infraroten Diodenlaser mit externer Kavität, einem akusto-optischen Modulator und einer Messkavität, deren Länge mit Hilfe eines piezoelektrischen Umwandlers im Nanometerbereich verändert werden kann. Ein minimaler detektierbarer Absorptionskoeffizient von $6.2 \cdot 10^{-6}$ m^{-1} (SNR = 3) wurde erreicht. Dies entspricht einer Acetylenkonzentration von 67 ppbV in synthetischer Luft bei 100 mbar und einer Wellenlänge von 1530 nm. Geringste Acetylenkonzentrationen in einem Durchströmungsversuch konnten bei derselben Wellenlänge ebenfalls erfolgreich untersucht werden, wobei eine Detektionslimite von 460 ppbV in Ethylen bei 20 mbar gemessen werden konnte. Es wurde eine lineare Abhängigkeit des Absorptionskoeffizienten von der Acetylenkonzentration gefunden. Die Messanordnung eignet sich zudem für die Bestimmung von Isotopenverhältnissen.

Als Beispiel wurde ein Acetylenisotopenverhältnis von $^{13}C^{12}CH_2$ zu $^{12}C_2H_2$ von $2.47 \pm 0.13\,\%$ nachgewiesen. Dieser Wert stimmt mit Literaturwerten überein.

Die Cavity Ringdown Technik wurde von uns erstmalig in einmodigen Glasfasern, wie sie in der Telekommunikation verwendet werden, implementiert. Dabei wurden zwei Facetten von Fasersteckern mit dielektrischen Spiegeln versehen, um eine Kavität in einer Glasfaser erzeugen zu können. Auf diese Weise konnten geringste Krümmungsverluste in Glasfasern ermittelt werden. Die experimentellen Daten wurden mit Werten, die auf einem theoretischen Modell beruhen, verglichen, und eine sehr gute Übereinstimmung der Daten konnte aufgezeigt werden. Modulationen der Krümmungsverluste in Abhängigkeit des Krümmungsradius, die vom theoretischen Modell vorausgesagt werden, konnten experimentell bestätigt werden. In einer 10 m langen Faserkavität wurde ausserdem eine Detektionslimite von $1.72 \cdot 10^{-3}$ dB pro Kavitätsdurchgang erreicht. Vergleicht man diesen Wert mit einer speziellen Glasfaser, die gegenüber Krümmungen unempfindlich ist, d.h. einen Krümmungsverlust von < 0.05 dB bei 30 Windungen auf einem 20 mm dicken Zylinder aufweist, so liegt unsere Nachweisgrenze eine Grössenordnung unter diesem Wert. Die Faserkavitätsanordnung wurde ebenfalls erfolgreich eingesetzt, um Wasserstoff, welcher in die Faserkavität ein- oder ausdiffundiert, nachzuweisen. So wies eine wasserstoff-gesättigte Faserkavität einen zusätzlichen Verlust von 1.2 dB/km bei 1586 nm auf. Auch hier bestätigten theoretische Betrachtungen die gemessenen Verluste in der Faserkavität während des Diffusionsprozesses. Ausserdem konnte die Diffusionskonstante von Wasserstoff in Quartz aus den experimentellen Daten evaluiert werden: $D_{H_2 - silica} = (3.02 \pm 0.07) \cdot 10^{-15}$ m^2/s bei 30° C in Übereinstimmung mit Literaturwerten für Diffusionskonstanten von Wasserstoff in Quartz.

Diese Arbeit beginnt mit einer allgemeinen Übersicht über die Spektroskopie und behandelt theoretische und experimentelle Aspekte von einer spektroskopischen Methode im Speziellen; der Cavity Ringdown Technik. Eine kurze theoretische Betrachtung dieser Methode wird im Kapitel zwei besprochen. Kapitel drei beschreibt detailiert unser Nah-Infrarot Cavity Ringdown Ex-

periment. Das Kapitel zeigt zudem die gewonnenen Messergebnisse auf und diskutiert sie. Kapitel vier führt die neu entwickelte Faserkavität Ringdown Technik ein, welche von Verlustmessungen in gekrümmten Faserkavitäten und Messungen von Wasserstoffdiffusion aus einer Faserkavität begleitet wird. Eine Schlussfolgerung und einen Ausblick beenden schliesslich diese Arbeit.

Chapter 1

Introduction to spectroscopy

1.1 Motivation

Petrochemical industries are seeking alternatives to measure impurities in ethylene and propylene products down at concentration of 10 ppbV or less. Present measurements, whose incentive is to avoid problems in the polymer plants downstream, are carried out by gas chromatography working, however, at its limit of detection. Alternatives to gas chromatography would also be attractive if they offer ways of multiplexing which could determine different impurities on one spectrometer [Con03]. Another industrial branch, the fiber industry, is interested in an accurate and non-destructive detection scheme in order to determine a low intrinsic loss in fibers. Thereby, the measurement of bending losses in special bend-insensitive fibers has a special relevance since opto-electronic devices become smaller and smaller [Fre03]. Moreover, the determination of minute optical losses in fibers provide a wide application field in fiber sensor technology.

This work focuses on one spectroscopic technique which is believed to be a potential answer for both industrial demands described above. The method is called cavity ringdown and is assigned to a laser spectroscopic method. Therefore, we start with a brief history of spectroscopy and the spectroscopic application fields. Advantages of laser spectroscopy are emphasized, followed

by a theoretical background of the cavity ringdown technique. The main part of the thesis is devoted to the presentation of the experimental results carried out by an open path cavity ringdown arrangement and by a new fiber cavity based ringdown setup. Finally, an outlook completes this thesis.

1.2   History of spectroscopy

In the year of 1666, Sir Isaac Newton accomplished the first spectroscopic experiment by collecting sunlight through a hole after which, a prism broke the light up into a continuous band of colors. Newton called this band a spectrum. Nearly one hundred years later, color bands with dark spaces between, i.e., a discontinuous spectrum, were observed for the first time by Thomas Melvill [Mel52]. He used the Newton prism method for the study of bright light of salt burning in a flame.

The Newton method was improved for the first time in 1802 when Wollaston replaced the round hole by a slit resulting in a purer and clearer spectrum. Thereby, he saw not a continuous sun spectrum as Newton had thought to see but dark lines in the solar spectrum. However, the explanation of this observation was first given by Joseph Fraunhofer a decade later. He examined the sun spectrum through a telescope allowing the observation of brighter spectra in more detail. The pioneer work of Fraunhofer was not only based on the discovery and mapping of hundreds of the dark sun lines, but also on finding them in the spectra of the planets and on observing similar lines in the spectra of a few of the brighter stars. A further step in the history of spectroscopy was the discovery of the missing of entire bands in the spectrum when Sir John Herschel observed light shining through certain colored glasses. Ten years later, a material was finally assigned to an absorption spectrum for the first time. Brewster studied light passing through certain types of gases and he found out in the comparison of the solar spectrum that the atmosphere of the sun contained among other things "nitrous acid gas".

A significant improvement of the spectrum clarity dates from 1839. A lens, i.e. a collimator, was introduced into the spectroscope independently by Swan and Simms. The collimator arranged the incoming light in such a way that all rays felt on the prism with the same orientation ensuring an identical refraction of the different colors. After this upgrade, the spectroscope, however, found its use not in the investigation of the origin of absorption or emission lines but as an ideal monochromatic light source for experiments like microscopic observations without chromatic aberration. It was not until the late 1850s, when Robert Bunsen and Gustav Kirchoff stated together the general principle that the line positions in a spectrum are characteristic for a specific substance. The science of optical spectroscopy was born.

Unfortunately, there was no theory before the 20th century that could satisfactorily explain the origin of the spectra of the elements or the reason why different elements have different spectra. It was Johann J. Balmer who found a simple numerical pattern following the frequency spectrum of hydrogen. Johannes R. Rydberg revised the pattern and smoothed the way for a first theoretical model presented by the Danish physicist Niels Bohr. The model predicting quantized energy levels was in good quantitative agreement with a measured hydrogen spectrum. In 1925, a new revolutionary theory, the so-called quantum mechanics explaining the discrete, quantum nature of the spectra, was developed by the physicists Werner Heisenberg and Erwin Schrödinger. Finally, the quantum mechanics has been extended to the quantum electrodynamics by Dirac, Heisenberg, and Pauli. It describes the interaction of radiation with matter completely [Din51, EBS, Joh91].

1.3 Spectroscopic applications

Today, a very wide application area is covered by spectroscopic techniques analyzing all kinds of samples qualitatively and / or quantitatively. The qualitative analysis implies the identification of a single unknown sample or of different components in an unknown mixture. Thereby, the characteristic

energy transitions of an atom or molecule, i.e. the characteristic absorption lines or its characteristic fingerprint, provide the explicit sample identification. The quantitative analysis determines the concentration of a known substance or component and is achieved in consideration of the absorbed or transmitted intensity of the incident light or by the determination of the intensity of light emitted by the sample. Figure 1.1 summarizes the two types of spectroscopic analyses.
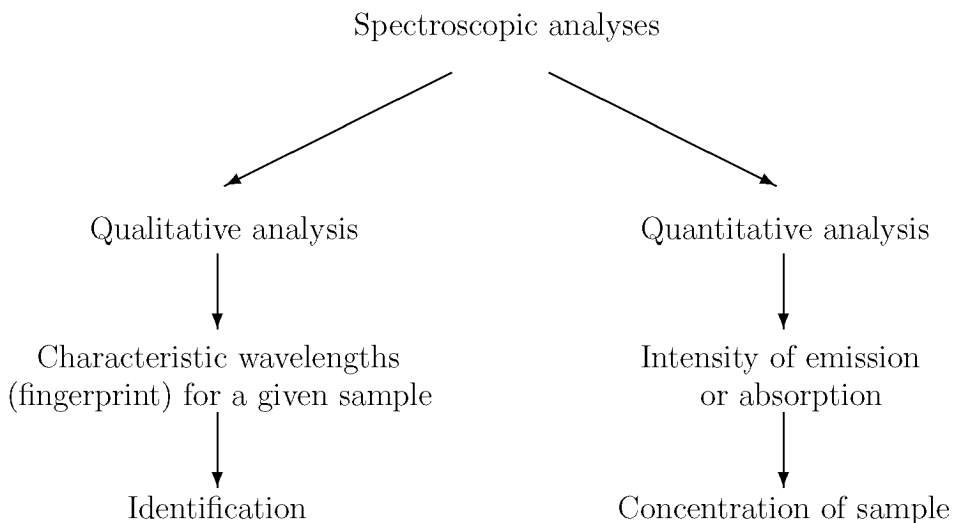

Figure 1.1: Spectroscopic analyses

Very often, both spectroscopic analyses are simultaneously applied for the study of, e.g., environmental and industrial processes, for security and safety issues or for medical diagnoses. The following section describes the spectroscopic applications in these fields in more detail. Figure 1.2 summarizes these applications areas.
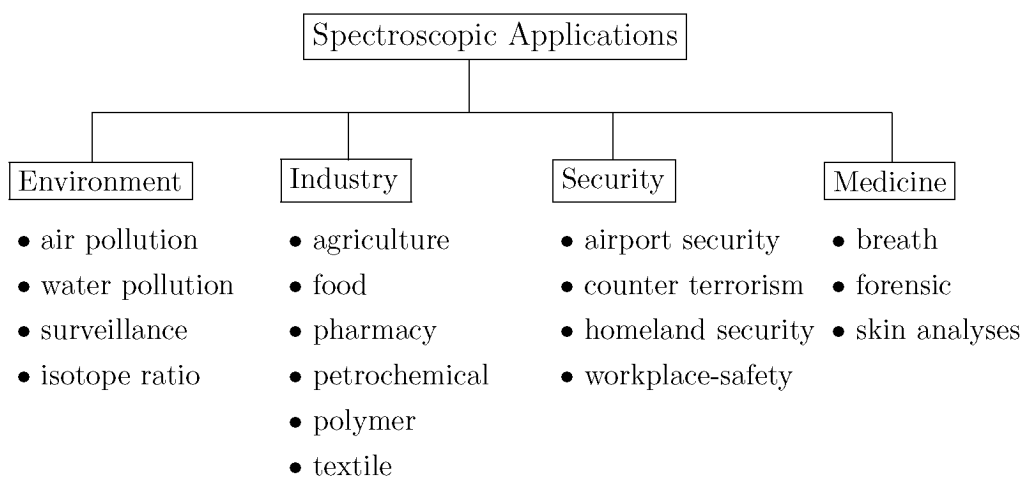
```
                    ┌─────────────────────────┐
                    │ Spectroscopic Applications │
                    └─────────────────────────┘
```

┌─────────────┐	┌──────────┐	┌──────────┐	┌──────────┐
│ Environment │	│ Industry │	│ Security │	│ Medicine │
• air pollution	• agriculture	• airport security	• breath
• water pollution	• food	• counter terrorism	• forensic
• surveillance	• pharmacy	• homeland security	• skin analyses
• isotope ratio	• petrochemical	• workplace-safety	
	• polymer		
	• textile		

Figure 1.2: Examples of spectroscopic applications

Environmental analyses imply the identification, the concentration determination, and the surveillance of trace gases and pollutants in air [Fis04, Mar03] or on water surfaces [Bun01]. Furthermore, spectroscopic techniques enable the study of chemical processes within the atmosphere by greenhouse gases, by primary pollutants and by solar UV radiation [Sig94], but they allow also the measurements of stable isotopic ratios of carbon, hydrogen, nitrogen, oxygen etc. The main purpose of isotopic measurements is aimed at the determination of carbon sources and sinks, at the study of photosynthesis and at the surveillance of eruption-endangered volcanos [Cas04, Wei05]. Last but not least, spectroscopic methods are well-established in astronomical observations [Dem01].

From food to polymer industries, spectroscopic methods are applied in divers industrial sectors. Food and agriculture industries use spectroscopy for fast and non-invasive food analyses (fruits and vegetables, sugar cane, coffee, tea, grain crops, baking and brewing products, meats, etc. [AlA04]). Spectroscopy is employed in textile industry to identify fibers, to determine re-

ducing sugars on the surface of cotton fibers, it is applied for process control, etc. [McC03]. Pharmaceutical industry takes also the advantages of non-invasive spectroscopic methods for the identification of pharmaceutical raw materials and the determination of agent and moisture content of medicaments. In addition, physical properties of a medicament like its size and density can be controlled by spectroscopic techniques. A critical review covering the near-infrared spectroscopy applications in the pharmaceutical industry can be found in [Bla98]. Cosmetic applications of spectroscopic techniques range from the determination of skin moisture to raw material testing and the analysis of product composition [McC03]. The analysis of petroleum products by the use of infrared spectroscopy has become an essential tool of hydrocarbon processing and refining. Motor and pump octane number, cetane, ethanol, lead, sulphur, etc. were successfully measured in such products as gasoline, diesel fuels, and jet fuels [Wor96]. Furthermore, polymer and chemical industries apply spectroscopic methods for the examination of raw materials and additives, for monitoring configurations and conformations of polymer molecules and in order to determine the chemical structure of a repeat unit [Koe01].

Sensors have been developed in order to detect and prevent terroristic threats to both military and civilian population at check-points, at military base and at public places like airports and train or metro stations. These sensors are often based on spectroscopic techniques and find their applications in the field of homeland security. They detect and identify hazardous materials like biological and chemical warfare agents [DeL05] or explosives (TNT, TATP, etc.) [Tod02]. Spectroscopic methods are used to monitor potentially hazardous gas concentration at work places and to ensure a safe work place with gas concentrations below the maximum permissible work place concentrations [Suva].

Trace gas is not only analyzed in air but also in human breath for diagnostic purposes. Ethane, for example, is regarded as a volatile marker for lipid peroxidation [Bas03, San03, Mur05] and methylamine absorption lines are a target to extend non-invasive diagnostic tools [Mar05]. Volatile gas emission from

the skin can also be studied with spectroscopic methods. As example, nitric oxide formation in human skin was examined which can influence erythema and edema formation or premature aging [Pau05]. Finally, spectroscopic techniques are applied in forensic science [Eyr02, Fer00].

1.4 Laser spectroscopy

A new revival of spectroscopic investigation started with the development of the laser technology in 1960 when the first lasing process, i.e. monochromatic light, was observed [Mai60]. Since then, many types of lasers have been constructed at different wavelengths at which laser light may interact with matter. Light assigned to the middle-infrared (MIR) range (2.5 μm - 25 μm) can excite fundamental bonding vibrations of molecules. Thereby, the absorbed photon energy matching the natural vibrational energy of the molecules serves to increase the amplitude of the vibration motion of bonds in molecules. However, only those bonds that have a dipole moment which changes as a function of time are capable of absorbing infrared radiation (infrared-active molecules). Overtone vibrations of molecules can be excited by photon absorption processes in the near-infrared (NIR) region (770 nm - 2.5 μm). Reliable and intense infrared lasers offering wide tunability are therefore preferable sources for spectroscopic measurements.

The advantages of laser spectroscopy can be enumerated as follows. The monochromatic light of a laser makes monochromators redundant and permits a selective atom or molecule detection. Furthermore, the coherent laser light implies a collimated beam propagation which is well suited for remote or in-situ measurements. Coherent light allows also spectroscopic analyses based on the extraction of phase information. In addition to that, an intense laser promises a fast and accurate data acquisition and hence, a good temporal and sensitive resolution which is required for on-line monitoring. If the laser additionally features a wide wavelength tunability and a narrow linewidth, a good spectral resolution over a certain spectral range can be achieved resulting in the op-

portunity for multicomponent analysis or detection. Since the infrared range is partly accessible by robust, reliable and portable lasers, they are well suited for field measurement. Reliable and cost-effective telecommunication semiconductor lasers cover the near-infrared range. They are often fiber-coupled what eases the beam guidance and the handling of the experimental alignment. Compared to the conventional wideband sources, laser technology and especially wavelength-tunable lasers increase the spectral resolution and the spectroscopic sensitivity by several orders of magnitude.

Various detection schemes have been introduced for laser-spectroscopic studies in the history such as multipass absorption spectroscopy, intra-cavity absorption spectroscopy [Dem03] or photoacoustic spectroscopy [Mic03]. A more recent method is the so-called cavity ringdown spectroscopy (CRDS) determining the time-dependent intensity decay of light leaking out of a high-finesse cavity, i.e. the lifetime of photons within a cavity [OKe88]. Hence, a time measurement allows an accurate determination of optical cavity losses. Today, the cavity ringdown technique is well established and known as a sensitive spectroscopic method.

In the following chapters, the theoretical and experimental background as well as the applications of the CRDS technique are discussed in more detail.

Chapter 2

Cavity Ringdown Technique

2.1 Origin of the cavity ringdown technique

The origin of the cavity ringdown method goes back to sensitive measurements of optical reflectance at the end of the eighties. The reflectance played an important role in the design and construction of ring laser gyros [San77] and of high-power infrared (IR) laser systems based upon electronic transitions [Her81]. In such laser systems, the gain was so low that mirrors in excess of 99.95% reflectivity were required for an initial lasing demonstration. In 1977, a first reflectivity measurement for low-loss laser mirrors was reported based on a technique which involved two intralaser cavity measurements, one with the sample mirror and one without [San77]. The comparison between the two measured results allowed a determination of the sample mirror reflectivity, i.e. the determination of the additionally induced loss by the sample mirror with an accuracy of 100 ppm. Three years later, the so-called cavity-attenuated phase-shift or shortened CAPS-method was described for the first time [Her80]. In this method, a sinusoidal-amplitude-modulated continuous-wave laser beam is coupled into a cavity formed by two highly reflective mirrors. With respect to a reference beam propagating outside the cavity, the cavity induced a phase shift depending on the time for which the photons were trapped in the resonator. A cavity loss measurement below 100 ppm was achieved. Originally, this method was invented for the development and characterization of laser mirrors in the

near and mid-infrared range [Her81, Kwo82] and although a relation to the effects of absorption, scattering and transmission from elements in the cavity was attributed to the CAPS-method already then, it took nearly eight years until a cavity-enhanced measurement found its way to spectroscopic applications.

Before cavity-enhanced spectroscopic measurements were introduced, Anderson et al. had reported on a mirror reflectometer measuring directly the photon lifetime in a cavity with a fast power meter in 1984 [And84]. The photon lifetime defines a characteristic intensity decay time of light within the cavity which makes a conclusion to the reflectivity of the mirrors possible. A total loss resolution of 5 ppm was demonstrated and the described experiment already contained most devices found in an actual continuous-wave (cw) cavity ringdown experiment. A cw laser was used as a monochromatic light source. A fast light amplitude modulator interrupted the light very quickly when the laser frequency was in accordance with a fundamental longitudinal cavity mode. This allowed a record of an undisturbed intensity decay in the cavity. Furthermore, mode-matching lenses were implemented in the experiment for an improved excitation of the fundamental cavity mode and for an improved suppression of higher transversal modes and last but not least, a fast detector recorded the ringdown event.

Finally, in 1988, O'Keefe et al. published a paper that described the cavity ringdown technique (CRD) for spectroscopic applications [OKe88]. Oxygen was measured with a dye laser at 690 nm and 630 nm. The sensitivity was about 450 ppm and 75 ppm, respectively, corresponding to a minimum detectable absorption coefficient of $\sim 10^{-6}$ cm^{-1}. Since the cavity length was fixed, a pulsed laser (10 ns pulse duration) was used for a good light injection into the resonator (see section 2.2 for further information.) A first trace gas detection using the pulsed cavity ringdown technique was reported in 1995 [Jon95]. An ammonia detection at the 10 ppb level was stated in the near ultraviolet region and the paper abstract already announced: "Basic considerations regarding the use of CRD for trace gas detection are given and it is concluded that CRD spectroscopy holds great promise for sensitive [(sub)-ppb]

and fast (kHz) detection of many small molecules [Jon95]." One year later, the pulsed cavity ringdown technique was combined with the multiplex advantage of a Fourier Transform (FT) spectrometer. A broadband dye laser pulse was coupled in a cavity and the light exiting the cavity was guided to a FT-spectrometer resulting into an interferogram, i.e in a spectrum [Eng96].

The way for a continuous-wave cavity ringdown experiment was smoothed by Rempe et al. in 1992 [Rem92]. They presented a measurement of ultra-low losses in an optical interferometer, in this case a cavity, formed by two mirrors. One of them was mounted on a piezoelectric transducer allowing a slow scan of the cavity length in order to match the laser frequency with a fundamental longitudinal cavity mode. This mechanism was necessary since the linewidth of a cw laser is much narrower than the one of a pulsed laser (for further information, please consult section 2.2). In addition, an acousto-optical modulator turned off the cw laser light within 45 ns when a fundamental cavity mode matched the laser frequency. This way, the lowest observed mirror loss of 1.6 ppm was announced corresponding to a mirror reflectivity of 99.99984 %. The technique of a swept cavity was later adopted by Romanini et al. reporting on a measurement of weak HCCH overtone transition near 570 nm in 1997 [Rom97₁]. Thereafter, numerous papers have been published presenting measurements of different gases or cavity ringdown experiments with different laser sources and at different wavelengths [Sch95, Rom97₂, Ber00, He00, Pal00] (representing just a small selection).

Further extensions and developments of the cavity ringdown technique have continued. In 1997, a first evanescent-wave cavity ringdown spectroscopy with a total-internal-reflection (TIR) minicavity was proposed. A monolithic, polygonal, TIR-ring resonator extended the cavity ringdown concept to surfaces, thin films, liquids and condensed matter spectroscopy [Pip97₁]. Shortly after, this proposal was realized and surface processes were probed by cavity ringdown method through the absorption of the evanescent wave [Pip97₂]. Finally, completely solid-state cavities were employed in cavity ringdown experiments and minute fiber losses could be measured in fiber cavities [Ler00]. In 2002,

liquid samples were analyzed with the cavity ringdown technique. Cuvettes with the liquid were placed in a high-finesse cavity whereby a minimum detectable absorption of 10^{-6} cm^{-1} corresponding to picomolar concentrations for strong absorbers was achieved [Hal02] or simply, the cavity was entirely filled with the corresponding liquid [Xu02].

Today, the cavity ringdown technique is known as a sensitive and reliable method for spectroscopic applications. Good summaries and reviews about the cavity ringdown technique are given in [Sch97, Whe98, Bus99, Ber00]. However, for a deeper understanding of this method, we are also bound to consider it from a theoretical point of view. The following sections will treat the theoretical background of the cavity ringdown technique in more detail.

2.2 Theory of the cavity ringdown technique

In order to understand the theoretical background of the cavity ringdown technique, we begin with a short theoretical summary covering the most important subjects of mirrors and cavities. The treatment is mainly based on [Sie86], otherwise, the source is announced in the text.

2.2.1 Mirrors and cavities

To trap light between two or more mirrors, their alignments have to fulfill the stability condition of a cavity. The condition depends on the ratio of the cavity length L to the mirror curvature radius $\mathcal{R}_M$. By introducing a g-parameter of the mirror:

$$g_j = \left(1 - \frac{L}{\mathcal{R}_{M_j}}\right), \tag{2.1}$$

where j denotes the jth mirror forming the cavity, the stability condition for a two mirror cavity is expressed as:

$$0 \leq g_1 g_2 \leq 1. \tag{2.2}$$

Here, we consider only cavities formed by two mirrors featuring the same curvature radius, i.e. symmetric cavities where $g_1 = g_2 = g$. Therefore, the criteria to form a stable symmetric cavity is then:

$$L \leq 2\mathcal{R}_M. \tag{2.3}$$

Consequently, the length of a stable cavity has to be shorter than twice the mirror curvature radius. For example, a 0.52 m-long or shorter cavity formed by two confocal mirrors featuring a curvature radius of $\mathcal{R}_M = 1$ m fulfills the stability condition and allows a stable back and forth reflection of light between the mirrors. The examples in this section are based on values which can be found in our experiment (see chapter 3).

We restrict our further theoretical consideration of the cavity ringdown technique on monochromatic light propagating in a cavity. Continuous-monochromatic light, expressed by the intensity I_{inc} or by the electric field E_{inc}, is coupled into a resonator formed by two mirrors as shown in Fig. 2.1. After the light transmission through the first mirror, the field amplitude E_o in the cavity is given as:

$$E_o = i\sqrt{T_1}E_{inc}, \tag{2.4}$$

where i represents the 90° phase-shift between the incident and the transmitted field arising from the measurement of the amplitudes at two different reference planes and T_1 denotes the intensity transmission coefficient of the first mirror.
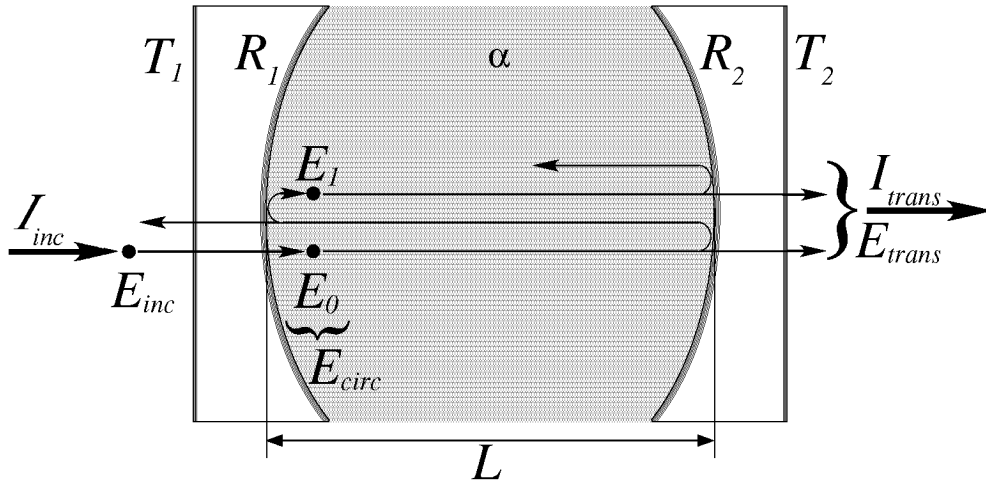

Figure 2.1: Electric field in a cavity

Schematic picture of a two mirror cavity of the length L with the incident E_{inc}, the transmitted E_{trans} and the partial E_j field amplitudes as well as the incident and transmitted intensities I_{inc} and I_{trans}. $R_{1,2}$, $T_{1,2}$ and α denote the intensity reflection, transmission and the absorption coefficient, respectively.

The light passes the cavity length following the Beer-Lambert law (see Appendix for it), i.e. the field amplitude is reduced by the factor $e^{-\frac{1}{2}\alpha L}$ where α stands for the intensity absorption coefficient of a medium filling the whole space between the mirrors and L denotes the cavity length. After passing one distance between the mirrors, the light reaches the second mirror and is reflected back with an intensity reflection coefficient R_2. It passes the cavity again and is finally reflected forth by the first mirror featuring a reflectivity R_1 towards the second one. Therefore, the field E_1 after one round trip is given as (see also Fig. 2.1):

$$E_1 = \sqrt{R_1 R_2} e^{-\alpha L} e^{-i\frac{2\omega L}{c}} E_o, \tag{2.5}$$

where ω denotes the angular light frequency and c the speed of light.

The amplitude E_{circ} of the circulating field in the cavity is the superposition of the partial field amplitudes, i.e. of the incident field and of all the reflected fields with different numbers of round trips:

$$\begin{aligned} E_{circ} &= \sum_j E_j \quad \left(\text{with } E_j = \left(\sqrt{R_1 R_2} e^{-\alpha L} e^{-i\frac{2\omega L}{c}} \right)^j E_o \right) \\ &= \frac{E_o}{1 - \sqrt{R_1 R_2} e^{-\alpha L} e^{-i\frac{2\omega L}{c}}} \stackrel{(2.4)}{=} \frac{i\sqrt{T_1} E_{inc}}{1 - \sqrt{R_1 R_2} e^{-\alpha L} e^{-i\frac{2\omega L}{c}}}. \end{aligned} \tag{2.6}$$

The circulating light intensity I_{circ} in the cavity is given by the absolute value $|E_{circ}|^2$:

$$I_{circ} = |E_{circ}|^2 = \frac{T_1 I_{inc}}{\left(1 - \sqrt{R_1 R_2} e^{-\alpha L} \right)^2 + 4\sqrt{R_1 R_2} e^{-\alpha L} \sin^2\left(\frac{\omega L}{c}\right)} \tag{2.7}$$

and depends on the incident light frequency. Since not any light frequency interferes constructively in a cavity, the laser frequency ν has to match a cavity resonance frequency so that I_{circ} is maximum and $\sin(\frac{\omega L}{c}) = 0$, i.e. $\frac{\omega L}{c} = q\pi$ or $\nu = q\frac{c}{2L} = q\nu_F$, where q denotes an integer and ν_F is the so-called free spectral range, i.e. the frequency distance between two maxima of the circulating intensity in a cavity. One technique to bring the laser frequency in coincidence with

the cavity resonance frequency is to sweep slightly the cavity length resulting in a different free spectral range and in a shift of the cavity resonance frequencies.

The transmission of the cavity $\mathcal{T}$ is defined by the ratio of the transmitted and incident intensities:

$$\mathcal{T} = \frac{I_{trans}}{I_{inc}} = \frac{T_2 I_{circ}}{I_{inc}} = \frac{T_1 T_2}{\left(1 - \sqrt{R_1 R_2}e^{-\alpha L}\right)^2 + 4\sqrt{R_1 R_2}e^{-\alpha L}\sin^2(\frac{\nu}{\nu_F}\pi)}. \quad (2.8)$$

Figure 2.2 depicts a comparison between a laser mode featuring a linewidth of 300 kHz which corresponds to a typical external cavity diode laser (ECDL) linewidth and a longitudinal mode of a 0.5 m-long cavity formed by two mirrors with a reflectivity of 99.99 %. The linewidth of the cavity mode is about 10 times smaller than the laser mode. Consequently, only about 10 % of the laser power can be coupled into the cavity.

The maximum transmission $\mathcal{T}_{max}$ of a cavity is achieved if the frequency of the incident light is a multiple of the free spectral range $\nu = q\nu_F$, i.e.:

$$\mathcal{T}_{max} = \frac{T_1 T_2}{\left(1 - \sqrt{R_1 R_2}e^{-2\alpha L}\right)^2}. \quad (2.9)$$

If we consider an empty cavity formed by two identical mirrors with no absorbing medium between the mirrors so that $R_1 = R_2 = R$, $T_1 = T_2 = T$ and $\alpha = 0$, and by taking into account the energy conservation ($R + T = 1$), the maximal transmission of a cavity is $\mathcal{T}_{max} = 1$. Unfortunately, this is only the case if $R < 1$ and $T > 0$, i.e. if the mirror absorptions are neglected. Since highly reflective mirrors $R \approx 1$ are made by dielectric layers with different refractive indices, light is absorbed during the propagation through the dielec-
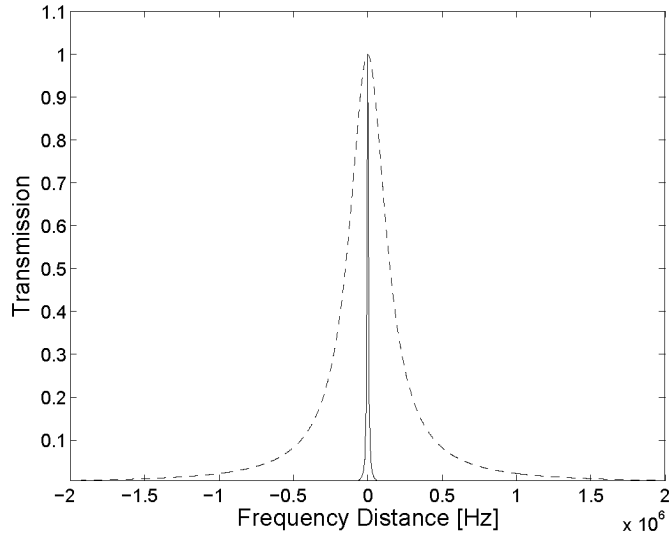
Figure 2.2: Cavity transmission

Laser mode featuring a linewidth of 300 kHz (– –) and a cavity mode formed by mirrors with $R = 99.99$ %, $L = 0.5$ m and $R + T = 1$ (——)

tric mirror resulting in $\mathcal{T}_{max} < 1$. Furthermore, the linewidth of the incident light is usually broader than the linewidth of the cavity mode which also reduces the maximum transmission (see Fig. 2.2).

A useful expression describing the quality of a cavity is the so-called finesse $\mathcal{F}$ defined by the reflectivity of the mirrors forming the resonator and by the losses within the cavity. We consider cavities without or with an absorbing medium with negligible absorption between the mirrors. Thus, the finesse can be expressed by the mirror reflectivities only:

$$\mathcal{F} = \frac{\pi \sqrt[4]{R_1 R_2} e^{-\frac{\alpha L}{2}}}{1 - \sqrt{R_1 R_2} e^{-\alpha L}} \approx \frac{\pi \sqrt[4]{R_1 R_2}}{1 - \sqrt{R_1 R_2}}. \tag{2.10}$$

The finesse is a measure of the effective path length covered by the trapped light and for high-finesse cavities, the effective path length L_{eff} is a multiple

of the cavity length and given as [He02]:

$$L_{eff} = \frac{2\mathcal{F}}{\pi} L. \qquad (2.11)$$

For example, the effective optical length of a cavity with a finesse of $3.1 \cdot 10^4$ ($R = 99.99$ %) results in $L_{eff} = 2 \cdot 10^4 \cdot L$. By considering a 0.52 m-long cavity, the effective length amounts to about $L_{eff} = 10.4$ km. Since the light absorption in a medium is described by the Beer-Lambert law, the sensitivity of a cavity-enhanced absorption measurement is enormously improved by the elongation of the optical path.

For a better understanding of the light propagation in a cavity, we consider the formation of resonant modes in optical cavities and assume that the paraxial condition is always fulfilled. Resonant modes describe standing waves within the cavity where the electric vector of the oscillating light wave is zero at the boundaries. In general, the modes in a cavity can be classified in two types: longitudinal and transversal modes. The longitudinal modes determine the resonant oscillation frequencies satisfying the wavelength requirements of the cavity along a given optical path. Transverse modes propagate over slightly different optical paths and affect the intensity pattern and divergence of the propagating beam. The labeling of the transverse electromagnetic modes (TEM) follows the rules: TEM_{uwq} with $u = $ azimuth, $w = $ radial and $q = $ longitudinal mode numbers. Fundamental longitudinal TEM_{00q} modes in cavities have always the shape of a Gaussian beam. Higher order transverse modes are described by Hermite-Gaussian modes in a cavity with a rectangular cross-section whereas Laguerre-Gaussian modes are excited in a cylindrical symmetrical cavity. We will focus our attention to cavities formed by mirrors with a circular cross section since this kind of cavities are employed in our cavity ringdown spectroscopy experiment.

Following the consideration of [Bus99], the resonance condition of longitudinal modes in a cavity with length L is:

$$\nu_{00q} = \nu_q = \left(q + \frac{\triangle\zeta}{\pi} \right) \frac{c}{2L} \qquad (q = 1, 2, 3, ...), \qquad (2.12)$$

where $\triangle\zeta = \arccos(\pm\sqrt{g_1 g_2})/\pi$ denotes a phase shift due to the Gaussian shape of the beam (see also Eq. (2.14)). Hence, the free spectral range ν_F or the frequency difference between two neighboring longitudinal modes is given by:

$$\nu_F = \nu_{q+1} - \nu_q = \frac{c}{2L}. \qquad (2.13)$$

The resonant transverse modes TEM_{uwq} in a cavity with circular cross section depends on the g-parameters and fulfill the condition:

$$\nu_{uwq} = \left[q + (u + 2w + 1) \frac{\arccos\left(\pm\sqrt{g_1 g_2}\right)}{\pi} \right] \frac{c}{2L} \qquad (2.14)$$

and consequently, the mode spacing ν_T between two neighboring transverse modes is:

$$\nu_T = \nu_{u+2w+1} - \nu_{u+2w} = \left[\frac{\arccos\left(\pm\sqrt{g_1 g_2}\right)}{\pi} \right] \frac{c}{2L}. \qquad (2.15)$$

The frequency distance between two successive transverse modes is usually much smaller than the frequency spacing between two successive longitudinal modes: $\nu_T < \nu_F$. For example, a cavity with a length of 0.52 m features a longitudinal free spectral range of about $\nu_F = 300$ MHz and a transverse free spectral range of $\nu_T = 98$ MHz ($\mathcal{R}_M = 1$ m). Therefore, by employing a laser with a bandwidth of about 500 kHz in a CRDS experiment, maximum one mode can be excited at the same time. In a CRDS experiment with a pulsed laser where the bandwidth of the incident light is determined by the laser pulse duration, the simultaneous excitation of different modes results in a mode beating within the cavity and in a multiexponential decay of the ring-down event [Mar96]. Mode beating was also observed in our cavity caused by its imperfect alignment. Fig. 3.5 depicts a recorded mode beat event. Since such a decay prevents an accurate ringdown time determination, only a single fundamental longitudinal mode is preferred to be excited leading to an simple exponential decay of the event. However, degenerate transverse modes $\nu_{uwq} = \nu_{u^\star w^\star q^\star}$ can occur in a cavity if the following statement for the mode numbers is valid:

$$q + (u + 2w)\frac{\arccos\left(\pm\sqrt{g_1 g_2}\right)}{\pi} = q^\star + (u^\star + 2w^\star)\frac{\arccos\left(\pm\sqrt{g_1 g_2}\right)}{\pi}. \quad (2.16)$$

A schematic picture of the transverse mode degeneracy in a extrafocal cavity, i.e. $L \neq \mathcal{R}_M$, is depicted in Fig. 2.3.

The degenerate transverse modes can be separated by introducing a slight misalignment of the cavity. The frequency distance between the disturbed or non-degenerated transverse modes is then in the kHz range. A further special case in the transverse mode degeneracy can be found in a confocal resonator where $L = \mathcal{R}_M$ ($g_1 = g_2 = 0$). The term with arccos in Eq. (2.15) becomes 0.5 and consequently, the frequency of transverse modes with $u + 2w + 1 = even$
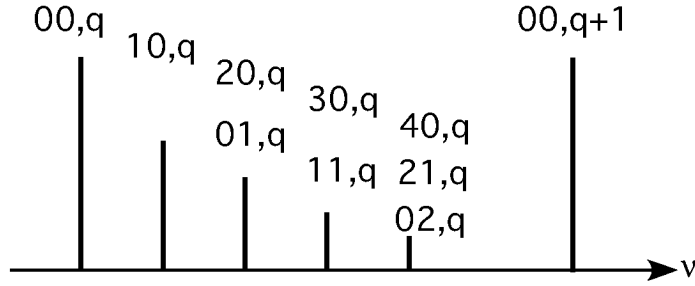
Figure 2.3: Transverse mode degeneracy

Schematic diagram of transverse mode degeneracy in an extrafocal cavity formed by circular mirrors.

falls together with a frequency of a longitudinal mode, whereas the frequency of modes with $u + 2w + 1 = odd$ lies exactly in the middle of two neighboring longitudinal cavity modes. This degeneracy can be prevented by leaving the confocal condition. A 0.52 m-long cavity formed by two mirrors featuring a curvature radius of $\mathcal{R}_M = 1$ m do not show confocal degeneracies.

The fundamental TEM$_{00}$ mode in a cavity has the shape of a Gaussian beam whose wavefront curvature matches the mirror curvature. In order to achieve a good conversion from the laser beam to the fundamental cavity mode, the Gaussian beam profile is briefly considered. The waist radius W_o and the end mirror spot radius W_e of the Gaussian beam depend on the length of the cavity, the wavelength λ of the enclosed light, and the g-parameter [Sie86]:

$$W_o = \frac{L\lambda}{\pi}\sqrt{\frac{1+g}{4(1-g)}}, \qquad W_e = \frac{L\lambda}{\pi}\sqrt{\frac{1}{1-g^2}}. \qquad (2.17)$$

In a symmetric cavity, the waist of the beam is always in the center of the resonator and features a plane wavefront. Therefore, mode matching lenses focus the laser beam at the waist of the cavity mode ensuring a plane wavefront of the incident light, i.e. a good mode conversion between the laser and

the longitudinal cavity mode, and a suppressed excitation of possible transverse modes.

Consequently, the design of our cavity cell take into account the curvature radii of the mirrors and the length of the cavity to exclude mode degeneracy within the cavity. Furthermore, a mode matching lens in front of the cavity is advisable since it helps to prevent the excitations of higher order cavity modes and ensures a good mode conversion from the laser to the cavity mode. Further details about our employed optical devices in order to achieve a good mode conversion are given in chapter 3.

2.2.2   Cavity ringdown theory

The cavity ringdown technique links the photon lifetime within a cavity with the cavity loss. The loss depends on the mirror reflectivity and the absorbing medium between the mirrors. In order to measure accurately the photon lifetime, the cavity-incident light has to be switched off very quickly after trapping sufficient light within the resonator. Therefore, our further consideration is slightly different from one related to the cavity transmission discussed above in section 2.2.1. The intensity loss factor per round trip ρ can still be written as:

$$\rho = R_1 R_2 e^{-2\alpha L} = e^{-2\alpha_t L} \qquad \text{with} \qquad \alpha_t = -\frac{1}{2L}\ln(R_1 R_2) + \alpha, \qquad (2.18)$$

where α_t is called the mean loss factor. In order to ease the understanding of the cavity ringdown technique, the trapped light is not considered as a cavity mode but as a single light bullet or ping-pong ball reflecting back and forth within the cavity. This consideration is valid as long as the duration of the laser pulse is assumed to be shorter than the roundtrip time of the cavity resulting in no field superposition within the cavity. Other considerations are

discussed in section 2.3. Figure 2.4 shows a schematic picture of a cavity with trapped light where the circulating light is no longer a superposition of fields originating from different round trips.
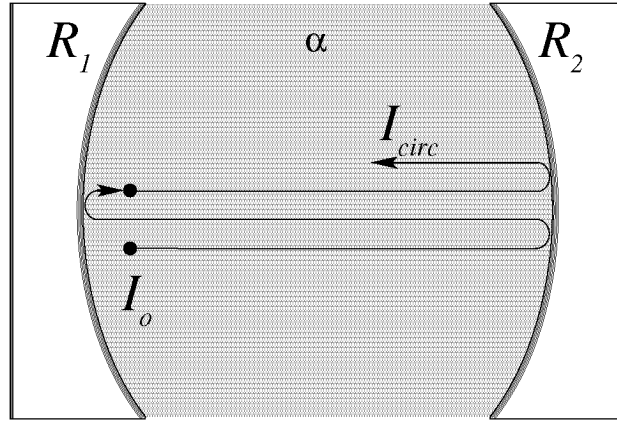

Figure 2.4: Intensity in a cavity

Schematic picture of a cavity formed by two mirrors with intensity reflectivity coefficients of R_1 and R_2. Initial I_o and circulating I_{circ} intensities in a medium featuring an absorption coefficient α

First of all, we are considering a cavity with two identical mirrors, so that $R_1 = R_2 = R$. The decay of the circulating intensity $I_{circ}(t)$ after the time t is given by the number of cavity round trips t/t_r, where t_r denotes the time for one round trip, i.e. $t_r = 2L/c$.

$$I_{circ}(t) = \rho^{\frac{t}{t_r}} I_o = I_o \exp\left(-2\left[\frac{1}{L}\ln\left(\frac{1}{R}\right) + \alpha\right] L\frac{t}{t_r}\right), \qquad (2.19)$$

where I_o denotes the initial intensity in the resonator. We rearrange Eq. (2.19) and assume that no absorbing medium is present between the mirrors so that $\alpha = 0$. In addition, an insightful interpretation is added:

$$I_{circ}(t) \quad = \quad I_o \exp\left(\qquad -2 \qquad\right) \exp\left(\ln\frac{1}{R}\right) \exp\left(\frac{t}{t_r}\right)$$

$$\text{(2.20)}$$

$$I_{circ}(t) \quad = \quad I_o \exp\left(-\frac{\text{number of reflections}}{\text{round trip}}\right) \exp\left(\frac{\text{loss}}{\text{reflection}}\right) \exp\left(\text{number of round trips}\right)$$

Since the mirrors used in the cavity ringdown spectroscopy are highly reflective, i.e. R $\approx$ 1, the logarithmic expression can be approximated as follows: $\ln(R^{-1}) \approx (1 - R)$ [Bro95]. Equation (2.19) is then:

$$I_{circ}(t) \approx I_o \exp\left(-\frac{c(1-R)}{L}t\right) = I_o \exp\left(-\frac{t}{\tau_o}\right),\qquad\text{(2.21)}$$

where τ_o denotes the ringdown time of a cavity with no absorbing medium between the mirrors. Hence, the intensity of trapped light within a cavity decays exponentially and is reduced by the factor $1/e$ within the ringdown time τ_o. This time constant depends on the reflectivity of the mirrors and on the length of the empty cavity:

$$\tau_o = \frac{L}{c(1-R)}.\qquad\text{(2.22)}$$

The ringdown time τ of a cavity filled with an absorbing medium featuring the absorption coefficient α can be written as follows:

$$\tau = \frac{L}{c[(1-R)+\alpha L]}.\qquad\text{(2.23)}$$

The higher the absorption within the cavity, the shorter the ringdown times become. By regarding Eqs. (2.22) and (2.23), we extract the absorption coefficient α and get:

$$\alpha = \frac{1}{c}\left(\frac{1}{\tau} - \frac{1}{\tau_o}\right). \qquad (2.24)$$

In general, we can write the ringdown time as a function of different absorbing species within the cavity:

$$\tau = \frac{L}{c[(1-R) + \sum_j \alpha_j l_j]}, \qquad (2.25)$$

where α_j denotes the absorption coefficient of the medium j and l_j is the length within which the loss takes place. The detection limit of the absorption coefficient depends on the acquired ringdown time deviation. The more accurate the ringdown time can be measured, the better the detection limit of the absorption measurement since a small absorption within the cavity changes the long ringdown time just a little bit. The detection limit of the cavity ringdown method is given as [Zal95]:

$$\alpha_{min} = \frac{1}{c}\left(\frac{1}{\tau_o - \triangle\tau} - \frac{1}{\tau_o}\right) = \frac{(1-R)\triangle\tau}{L(\tau_o - \triangle\tau)}, \qquad (2.26)$$

where $\triangle\tau$ denotes the minimum deviation in the ringdown time that can be accurately detected. For a SNR = 3, $\triangle\tau$ is equal to six times the standard deviation of the measured ringdown time without an absorbing sample present between the mirrors. So, the minimum absorption coefficient measured with

the CRDS technique is limited by the mirror reflectivity and the minimum deviation of the ringdown time τ_o.

2.3   Pulsed vs. cw cavity ringdown technique

Depending on the application of the cavity ringdown technique, both pulsed and continuous-wave laser systems are used. The advantages and disadvantages of both systems are summarized in the following section.

A pulsed cavity ringdown system is easier to build-up since firstly, no modulator is needed and secondly, no piezoelectric transducer has to be implemented in the cavity in order to sweep the cavity length to match cavity modes [Ber00]. In this system, two different cases can be distinguished. One case corresponds to the ping-pong model in which the duration of the laser pulse is shorter than the round trip time of the cavity (see subsection 2.2.2). The other case considers a laser pulse featuring a short rise time (shorter than the ringdown time) whose duration is, however, longer than the cavity round trip time. In this case, the electric fields within the cavity superpose each other and the broad spectral bandwidth of the pulse causes simultaneous excitations of several cavity modes. Therefore, the simplicity is introduced at the cost of sensitivity (excitation of several cavity modes) and selectivity (broad bandwidth of the laser pulse coupled in the cavity) of the measurement. As discussed above in section 2.2.1, the simultaneous excitations of several transversal cavity modes yield a multi-exponential decay of the ringdown event and a mode beating effect within the cavity, i.e. an interference effect between the different excited modes and hence, an inaccurate ringdown time acquisition [Zal95, Mar96]. In order to prevent the excitations of too many modes, short cavities are employed which feature a large free spectral range [Zal95]. However, a short cavity decreases the effective optical path of the light within the sample and therefore the sensitivity of the absorption measurement. The sensitivity is further limited by the duty cycle of the laser pulse system. In addition, the pulse duration limits the build-up time of the light inten-

sity within the cavity. Therefore, the intensity leaking out of the cavity is lower compared to the intensity achieved in a continuous-wave setup. The use of a continuous-wave laser in a cavity ringdown system also increases the selectivity of the experiment due to the narrower linewidth [Ber00]. In order to excite a cavity mode, the cavity length or the laser frequency has to be modulated. Usually, a piezoelectric transducer sweeps the length of the cavity and ensures the excitation of a single fundamental longitudinal cavity mode. Furthermore, the continuous-wave laser allows a sufficiently long build up of the cavity mode and therefore, a more accurate ringdown event acquisition and hence, a more accurate ringdown time determination. However, for a smooth ringdown event detection, an acousto- or an electro-optical modulator has to be introduced which switches off fast the laser beam after the incident laser frequency matched a frequency of a fundamental longitudinal cavity mode [Rom97i]. In addition, the repetition rate of the ringdown event is given by the modulator and the sweeping frequency of the cavity [Ber00]. The advantages of both systems are summarized in Tab. I.

Table I: Overview of pulsed and cw cavity ringdown spectroscopy

Cavity ringdown technique	
pulsed	continuous-wave
simplicity of experimental setup	acousto- or electro-optical modulator and cavity or laser frequency modulation required
broadband $\Rightarrow$ multimode excitation $\Rightarrow$ multiexponential decay	monochromatic $\Rightarrow$ single-mode excitation $\Rightarrow$ high spectral resolution
large tuning range of pulsed lasers	small tuning range of cw lasers
short cavity $\Rightarrow$ reduced multimode excitation	long cavity $\Rightarrow$ high sensitivity
pulse repetition rate of laser	high repetition rate possible $\Rightarrow$ sensitivity
short energy build-up time in cavity	long energy build-up time in cavity $\Rightarrow$ improved signal-to-noise

2.4 General conclusion

The cavity ringdown technique offers a wide variety of advantages compared to other laser spectroscopic methods. Since the cavity ringdown technique analyses the photon lifetime in a high-finesse cavity and not the absolute value of the light intensity leaking out of the cavity, this method is insensitive to laser power fluctuations [Ber00]. In addition, the comparison between the ringdown time of a cavity without an absorbing sample and the ringdown time of a cavity with a sample yields directly the absolute absorption coefficient of the sample (see Eq. (2.24)). Hence, neither reference nor calibration measurements are required in order to determine absolute sample concentrations [Bus99]. Furthermore, available highly reflective mirrors enhance the effective optical absorption path length within the sample by a multiple and provide a slow intensity decay in the cavity. It results an accurate determination of the ringdown time and a high sensitivity [OKe88] (see Eq. (2.26) and Appendix for it). Pulsed or continuous-wave laser systems can be employed in a cavity ringdown system depending on the given task, the application and the required sensitivity and / or selectivity [Ber00]. Further advantages of this technique are the opportunity to detect the ringdown event in a single-ended detection scheme which can be necessary for sensing applications in harsh environments, the detection of hazardous samples or measurements at low pressure, i.e. in the range of millibars [He01]. However, there are also drawbacks of this technique. The laser beam and the cavity have to be exactly aligned. Otherwise, no accurate measurements are possible or no signal can be recorded at all. The mirrors have to be realigned before every measurement as experienced by our own experiment (see chapter 3). In addition, the mirrors with dielectric coatings forming the cavity feature only a high reflectivity in a relatively small wavelength range (see Fig. 3.9 below), i.e. other pairs of mirrors may be required for wavelength ranges of interest.

In general, the employed spectroscopic scheme has to be appropriate for the fulfillment of the given task and conditions.

Chapter 3

Open-path Cavity Ringdown Spectroscopy

3.1 Introduction

The daily confrontation of polyethylene products like plastic bags, polyethylene terephthalate (PET) bottles, car interior etc. emphasizes the impact of plastics nowadays. The basis for the largest single class of plastics is formed by ethylene (C_2H_4) which is the simplest member of the olefinic hydrocarbon series (group of hydrocarbon compounds that has one or more double or triple bonds between carbon atoms in the linear chain). Furthermore, ethylene is one of the most important raw materials of the organic chemical industry and occurs in both petroleum and natural gas [EBE]. Since the production of plastics demands pure ethylene, ethylene plant operators are seeking ways to measure on-line impurities in ethylene product streams down at concentrations of 10 ppbV or less. Up to the present, the measurement of the impurities like acetylene, CO and CO_2, ethane and methane to mention only a few of them, is carried out by gas chromatography working at its limit with respect to sensitivity and time resolution. Therefore, alternative techniques are explored to fulfill the industrial requirements. Here, the sensitive cavity ringdown technique is considered which would further allow a real time concentration determination of different impurities in a pure ethylene stream [Con03]. The

following chapter describes our near-infrared based cavity ringdown setup, its characterization and its potential use in the petrochemical industry. In order to fulfill the given task, the experimental design is based on a continuous-wave CRDS setup. This ensures a high selectivity due to the narrow linewidth of the laser and a high sensitivity caused by the excitation of only one fundamental longitudinal cavity mode and by a higher repetition rate of the ringdown events. The advantages of the cw CRDS are summarized in section 2.3.

3.2   Near-infrared cavity ringdown experiment

3.2.1   Experimental setup

In order to analyze gas streams, our open-path cavity ringdown spectroscopy (CRDS) experiment is designed for the near-infrared range allowing the use of reliable and cost-effective optical devices as well as the use of silica-based single-mode fibers for easy light handling. The schematic CRDS setup is shown in Fig. 3.1.
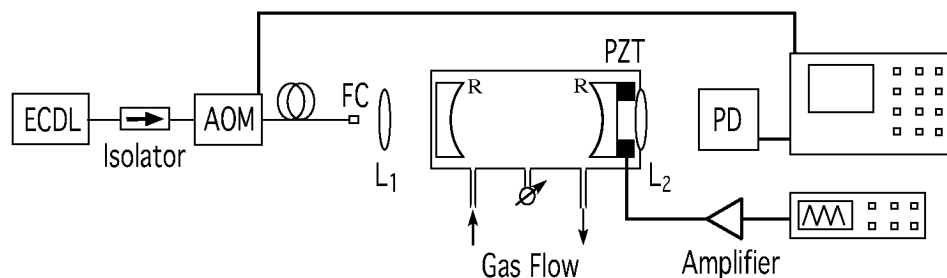
Figure 3.1: Schematic setup of the open-path CRDS

ECDL: external cavity diode laser; AOM: acousto-optical modulator; FC: fiber collimator; L: lens; PZT: piezo-electric transducer

As monochromatic tunable light source, two different fiber-coupled external cavity diode lasers can be employed: an EOSI laser (Newport, EOSI 2010) with a tuning range from 1520 nm to 1550 nm and a Santec laser (Santec,

TSL-210) tunable between 1520 nm and 1600 nm. The maximum output power of the lasers amounts to 1.5 mW and 9 mW, respectively, and both laser are coupled with a silica-based single-mode fiber. After the laser, an optical isolator prevents back reflections of light into the laser cavity and thus a distortion of the lasing process. The monochromatic light is then guided forward to an acousto-optical modulator (AOM; Infra Action, FCM-401E5C) allowing a fast amplitude modulation in case of a mode match between the laser and a cavity resonance frequency. After the AOM, a fiber collimator is used to couple the light out of the fiber with a small divergence angle ($\sim$ 0.8 mrad) in order to achieve a collimated free-space Gaussian laser beam. The focused waist of such beam is located in the focus spot of the lens [Sie86]. Therefore, an anti-reflection (AR) coated lens (L_1) featuring a 400 mm focal length focuses the laser beam in the middle of the hermetically sealable cell where the waist of the cavity mode can also be found. The cavity in the cell being made up of stainless steel is formed by two mirrors (Los Gatos Inc.) featuring a reflectivity of $>$ 99.99 % in the range of 1550 nm.

The body of the cell can be built up by one, two or three 150 mm-long stainless steel tubes whose inner diameter measures 35 mm. This modular configuration permits a variation of the cavity length and hence, cell bodies with lengths of 150 mm, 300 mm and 450 mm are realizable. Furthermore, two or three connections depending on the cell configuration offer the possibility to add a pressure sensor and hoses for the in and out flow of gases. However, the length of the cavity is not only given by the cell body itself but also by a self-designed cell end part mounted onto the cell body. Therefore, the total gas cell lengths amount to 27 cm, 42 cm or 57 cm whereby the distances between the mirror measure 22 cm, 37 cm or 52 cm. The longest configuration features a cell volume of 540 cm^3. A photo of the home-made cell is depicted in Fig. 3.2.

One end of the cavity cell consists of a commercial mirror mount (Los Gatos Inc.) allowing a mirror alignment by three screws from outside the cell. In this mount, the mirror lays directly on an O-ring which seals the cell from ambient air. The opportunity to align directly the mirror from outside
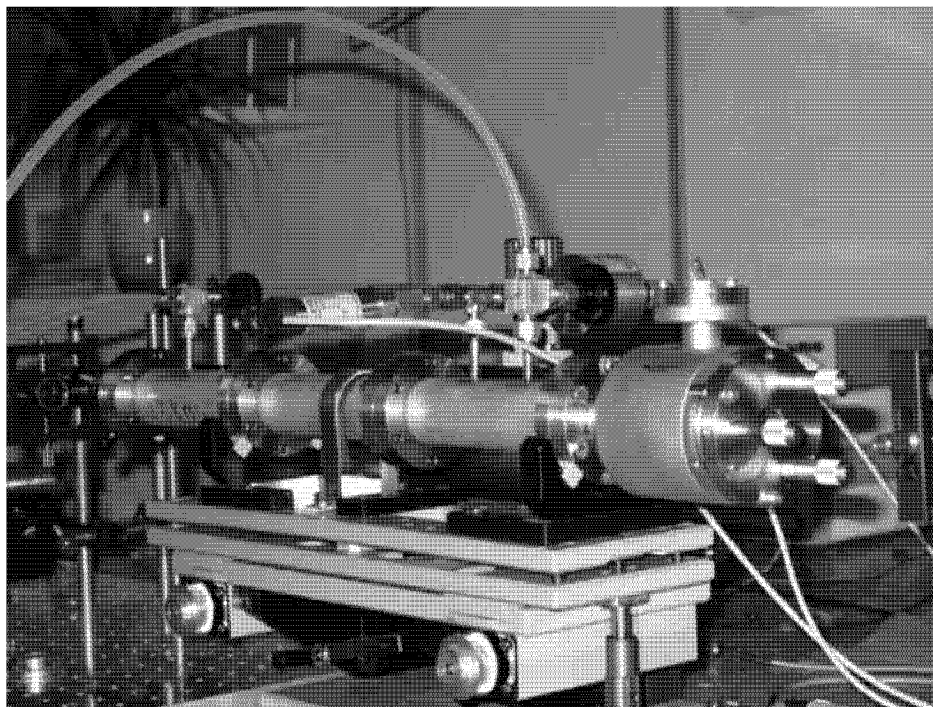
Figure 3.2: Home-made cavity ringdown cell

the cell provides an easy access to the alignment screws and a realignment of the cavity without opening the cell. The other end of the cell is sealed by a self-designed and home-made mount enclosing a piezo-electric ring transducer (PZT; Piezomechanik HPSt 1000/25-15/15 VS35). In this mount, the mirror is fixed on the high-voltage PZT which is screwed on a plate whose orientation can also be changed by three micrometer screws making the alignment of the mirror from outside the cell possible. An O-ring between the cell body and the PZT plate ensures a good cell sealing. Pressure changes of less than 1 mbar per hour were observed. In addition, the mount features an electric input for the PZT drive. Figure 3.3 shows the schematic home-made PZT mount.

After the PZT, the plate-embedded AR lens (L_2) focuses the light leaking out of the cavity on an InGaAs-photodiode (PD; New Focus, Model 1811) placed 25 cm after the cell (see Fig. 3.1). The 3 dB bandwidth of the photode-
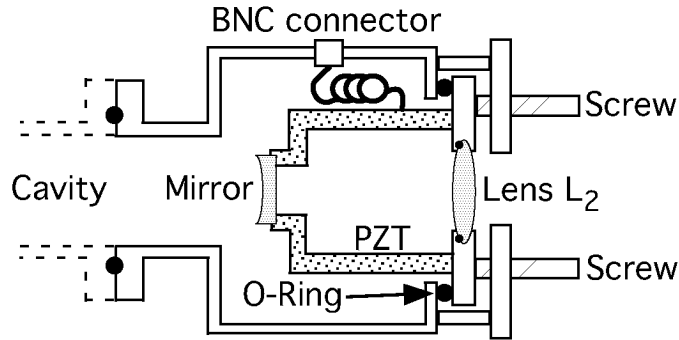
Figure 3.3: Schematic PZT mount

tector amounts to 125 MHz ensuring an accurate detection of ringdown events with a characteristic ringdown time of about 20 μs. The photon-induced diode current is internally amplified by a transimpedance amplifier with a gain factor of $4 \cdot 10^4$ and acquired by an oscilloscope (Tektronix, TDS 620). A trigger level which can be set on the oscilloscope controls the fast amplitude modulation in the AOM in case of a matching between the laser and cavity mode frequency. The digitized ringdown event is finally sent from the oscilloscope to a computer by which the event is analyzed.

3.2.2 Cavity alignment

The success of a sensitive and reliable gas spectrum measurement in a CRDS scheme depends crucially on a correct alignment of the mirrors forming the cavity. In order to get a stable cavity by two mirrors, both of them have to be perpendicularly oriented to the laser beam. The achievement of the mirror orientations is simplified by the introduction of a three arms fiber coupler (FCP) and a fiber-coupled photodiode (Thorlabs, D400 FC) in the experimental setup as shown in Fig. 3.4. A fiber coupled arrangement of the experiment proves now to be an advantage for the alignment procedure since it allows an easy change between the alignment and measurement setups. The fiber coupler features an intensity ratio of 99 % to 1 %, i.e. 1 % of the reflected light power is deflected to the fiber-coupled photodiode, the other 99 % are
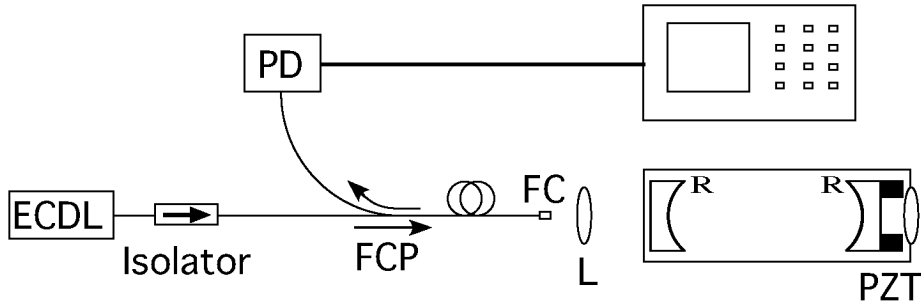
suppressed by the isolator.

Figure 3.4: Schematic setup for the cavity alignment

ECDL: external cavity diode laser; FC: fiber collimator; FCP: fiber coupler; L: lens; PZT: piezo-electric transducer

The actual alignment procedure takes place as follows. First, the PZT mount is screwed onto the open cell and its mirror is aligned by observing the reflected light intensity at the fiber-coupled photodiode. A perpendicular orientation of the mirror to the light beam is reached if the reflected light power shows a maximum. After the maximization of the reflected light, the cell is closed with the second mirror mount and that mirror is adjusted by the same procedure. Since the mirrors are directly or indirectly resting on an O-ring, the mirror alignment changes slightly with changing pressure in the cell. Therefore, the ultimate alignment has to be done immediately before the actual measurement at the corresponding cell pressure. In this phase, mode beating has to be prevented by a correct alignment of the mirrors. As discussed in section 2.2.1, mode beating occurs when different modes are simultaneously excited in the cavity whose different frequencies interfere resulting in a characteristic beat signal as shown in Fig. 3.5. A rough alignment process which is observable by the eyes can also be achieved by introducing a HeNe laser beam overlaping the near-infrared beam.
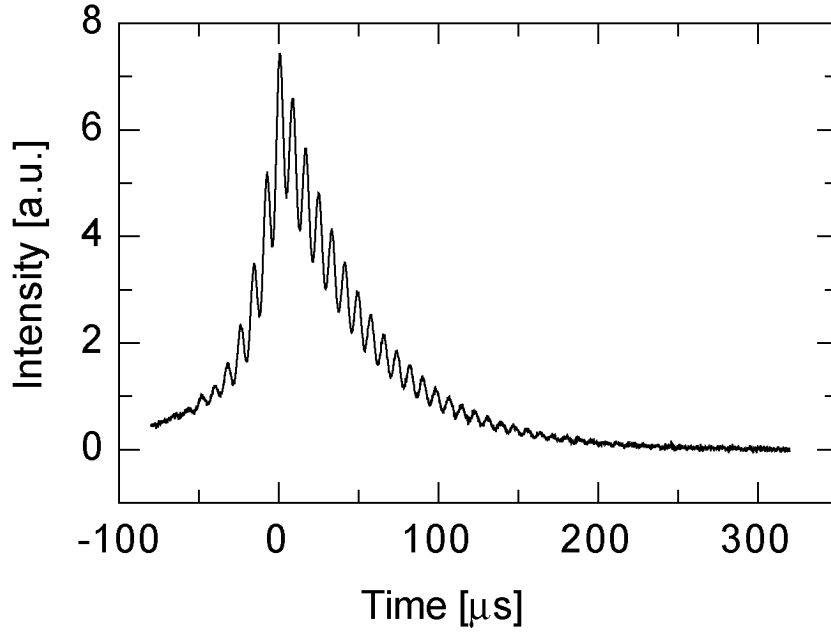
Figure 3.5: Mode-beating event

Mode beating during a ringdown event due to simultaneous excitation of different modes in the cavity caused by imperfect mirror alignment

3.2.3 Cavity ringdown event analysis

The analysis of the ringdown event is based on a fast fitting algorithm for a single exponential function [Mat87, Hal04]. Since the integration of an exponential function is again an exponential function, the original function can be expressed by the integrated form (method of successive integration). According to [Hal04]:

$$y(t) = y_o e^{-kt} + b = \underbrace{y_o + b}_{=:A} \underbrace{-k}_{=:B} \underbrace{\int_0^t y(\xi)d\xi}_{=:X} + \underbrace{kb}_{=:C} t$$

$$y(X, t) = A + BX + Ct, \tag{3.1}$$

whereby the integration X is further approximated by the trapezoidal numerical integration. The best fit coefficients A, B and C to the data set of the linear two-dimensional Eq. (3.1) can be calculated analytically by the method of the least squares leading to a linear equation system with three unknowns. The system can then be solved by the Gaussian Elimination technique. Further details are given in [Hal04].

The advantage of this algorithm, in the following we call it Matheson-Halmer algorithm, is its fast calculation time. It needs only a few hundreds microseconds for a dataset of about 2000 points and is therefore about 700 times faster than the nonlinear Levenberg-Marquardt fit provided by LabView [Hal04]. We implemented the algorithm with a C++ program and embedded it in the LabView program which solves then the resulted linear system. The single exponential function evaluated by the algorithm yields an excellent fit with the measured intensity decay (an average of 50 ringdown events) as shown in Fig. 3.6. Such an agreement is a further criterion for a correct cavity alignment. However, ringdown times of good exponential events may vary after a new cavity alignment. A ringdown time variation between 16 μs and 26 μs is observed in the 52 cm-long cavity. The reason for this broad variation is not clearly understood yet. Local variations of the reflectivity of the mirrors may be possible, the alignment and/or the incident location on the mirror may also vary the ringdown time.

Furthermore, ringdown events of the 52 cm-long cavity filled with synthetic air are also recorded in the range of 1531.72 nm and fitted with both the nonlinear Levenberg-Marquardt procedure provided by LabView and the Matheson-Halmer algorithm. Thereby, the average ringdown time of the baseline of synthetic air evaluated by the Levenberg-Marquardt (LM) procedure amounts to 26.97 μs $\pm$ 263 ns whereas the Matheson-Halmer (MH) algorithm yields an average time of 26.96 μs $\pm$ 264 ns. So, the difference in the results is only minor but the Matheson-Halmer algorithm works much faster as already mentioned. In addition, both results are compared at each wavelength, i.e. the normalized differences in respect of the Matheson-Halmer algorithm ringdown
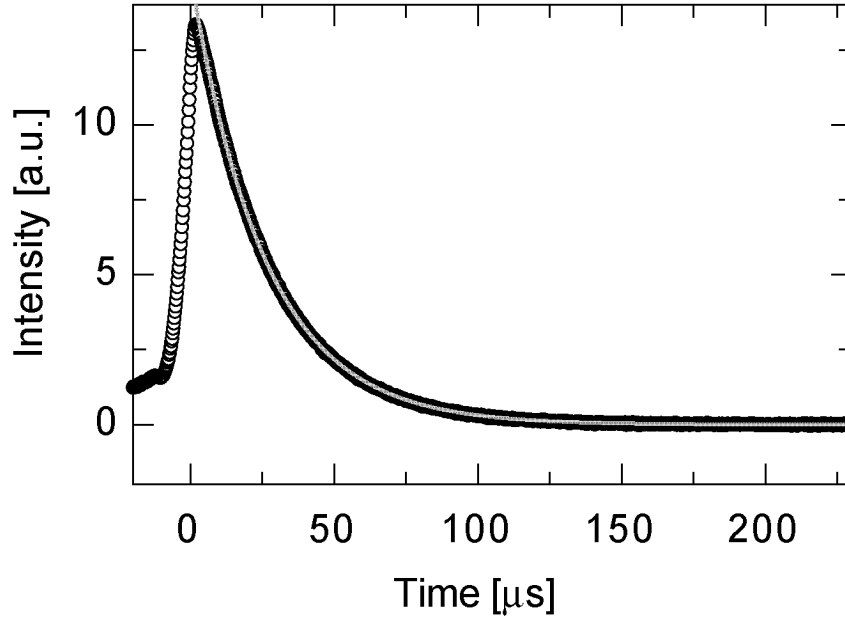
Figure 3.6: Ringdown event and exponential fit

Excellent agreement between the recorded ringdown event (o) and the exponential fit function (—). The determined ringdown time of this event amounts to **25.8** μs.

times, i.e. (LM data - MH data)/MH data, are evaluated and depicted in Fig. 3.7.

The normalized difference scatters in the range of $\pm$ 0.4 % and we find a minor average standard deviation of 13.5 ns between the ringdown times evaluated by the Matheson-Halmer procedure and by the Levenberg-Marquardt procedure. After the confirmation of the reliability of the self-written software, we start with the characterization of the hardware.
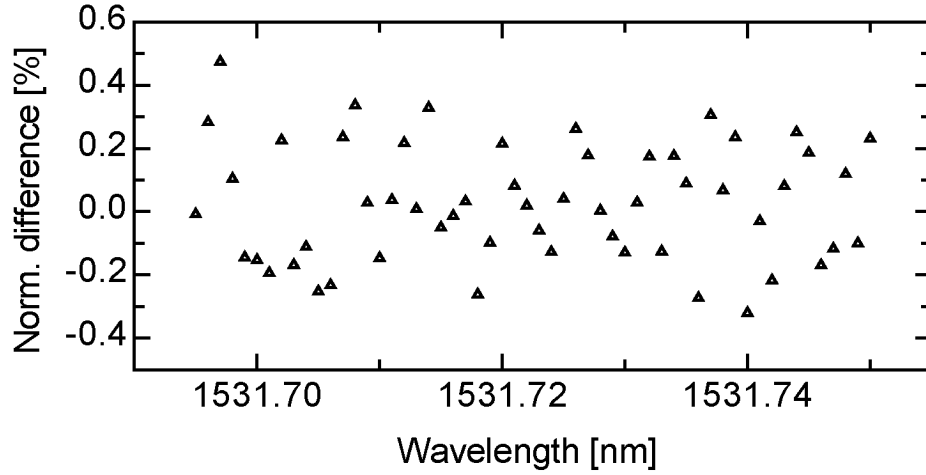
Figure 3.7: Comparison of ringdown time evaluation algorithms

Normalized difference [%] of analyzed ringdown events between the nonlinear Levenberg-Marquardt evaluation and the Matheson-Halmer algorithm. The average standard deviation in respect of the two different algorithm is only 13.5 ns for ringdown times in the range of 1531.72 nm.

3.2.4 Mirrors and cavity

The reflectivity of the employed mirrors may be determined with the measurement of the cavity ringdown time in an evacuated cell and with Eq. (2.22), i.e.:

$$R = 1 - \frac{L}{c\tau_o}. \tag{3.2}$$

Thereby, the Santec laser was tuned from 1520 nm up to 1600 nm in steps of 0.5 nm featuring an output power of 4 mW. This power is provided over the whole wavelength range. The evaluated ringdown times τ_o of the 52 cm-long cavity reach values from 15.9 μs up to 20.3 μs. Consequently, the reflectivity of the mirrors amounts to about 99.989 % at 1520 nm and increases to about 99.992 % at 1600 nm. The measurement results are depicted in Fig 3.8.
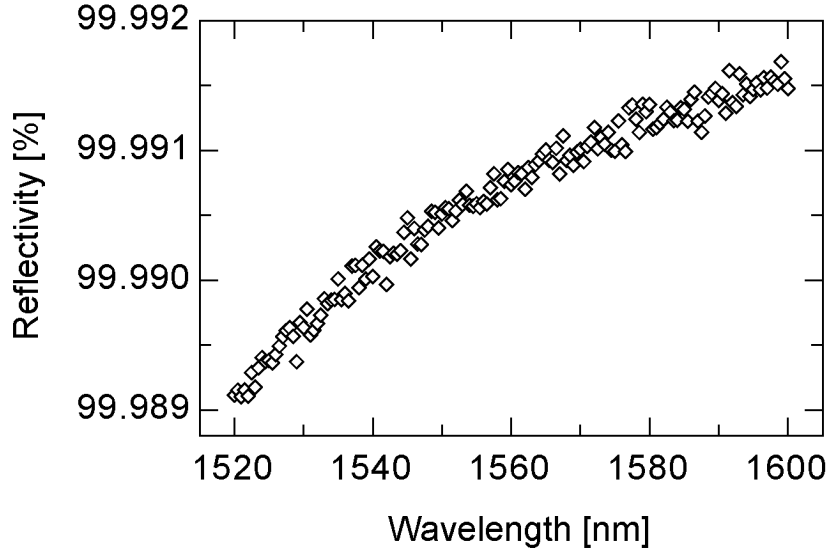
Figure 3.8: Measured mirror reflectivity vs. wavelength
Measured reflectivity of the dielectric mirrors forming the cavity in the
gas cell vs. wavelength

The manufacturer specification announces a mirror transmission of 0.01 %
at 1530 nm decreasing to about 0.004 % at 1600 nm as shown in Fig. 3.9.
The resulting discrepancy may be within the error range of the manufacturer
specification which is not known and the light absorption within the dielectric
mirrors.

Furthermore, a mode spectrum of the high finesse cavity was recorded at
1520 nm by tuning the cavity PZT in the gas cell over a range of about 80 V
with a bias offset of 280 V. The offset ensures a better linearity of the displace-
ment behavior of the PZT. The recorded spectrum is given in Fig. 3.10. The
excitation of fundamental longitudinal cavity modes is clearly detectable and
also a few suppressed higher order modes occur (see section 2.2.1). The reliabi-
lity of the mode appearance is good but since we have no cavity lock scheme,
not every fundamental longitudinal cavity mode is excited during a tuning
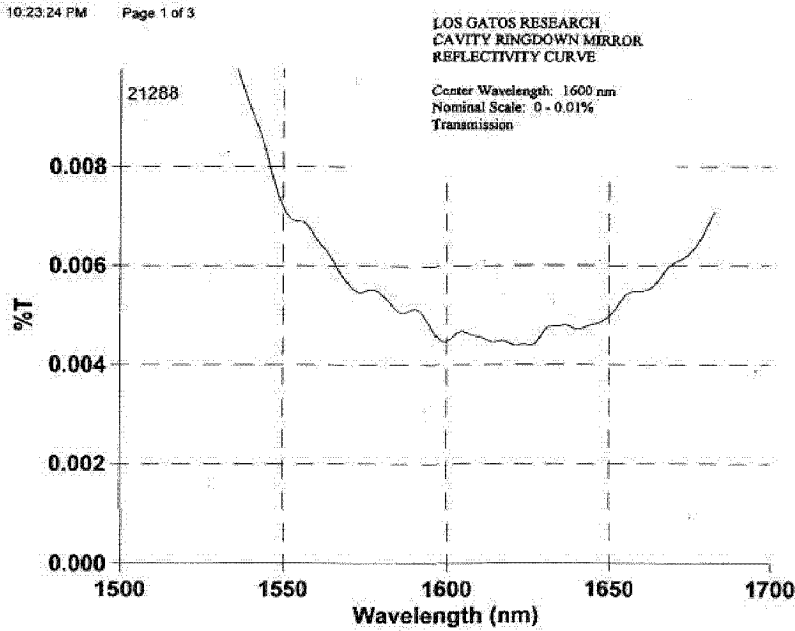period. The distance between two fundamental modes is found to amount to

Figure 3.9: Manufacturer specification of the mirror transmission

a voltage difference of about 43 V. The employed PZT features a maximum displacement of 17 μm with an applied bias of 1000 V. Since the linearity of the displacement vs. applied bias is given, 43 V causes a displacement of about 730 nm. This distance corresponds to about the half wavelength of the incident light and consequently to a neighboring fundamental longitudinal mode. Hence, good agreement between the theoretical consideration and our measurement is found. The next consideration concerns the maximum velocity of the mirror, i.e. the maximum tuning frequency which can be applied to the PZT. This frequency depends on the electric capacity of the PZT and the maximal average output current of the employed amplifier (Piezomechanik GmbH; SQV 1/500). The average current which is used to drive the PZT is given by $I_a = U_{max}Kf$ where U_{max} denotes the maximum bias, K is the actuators capacitance and f is the applied frequency [Pie98]. The maximum average output current of our amplifier amounts to 20 mA. Therefore, a maximum frequency of 300 Hz can be achieved with this amplifier ($U_{max} = 320$ V,

$K = 210$ nF). However, good mode excitation was ensured if the PZT was tuned with a lower frequency. In our experiment, a frequency of 10 Hz was applied resulting in a mirror velocity of 28 μm/s and a driving current of 0.63 mA. This low current provides a secure handling.

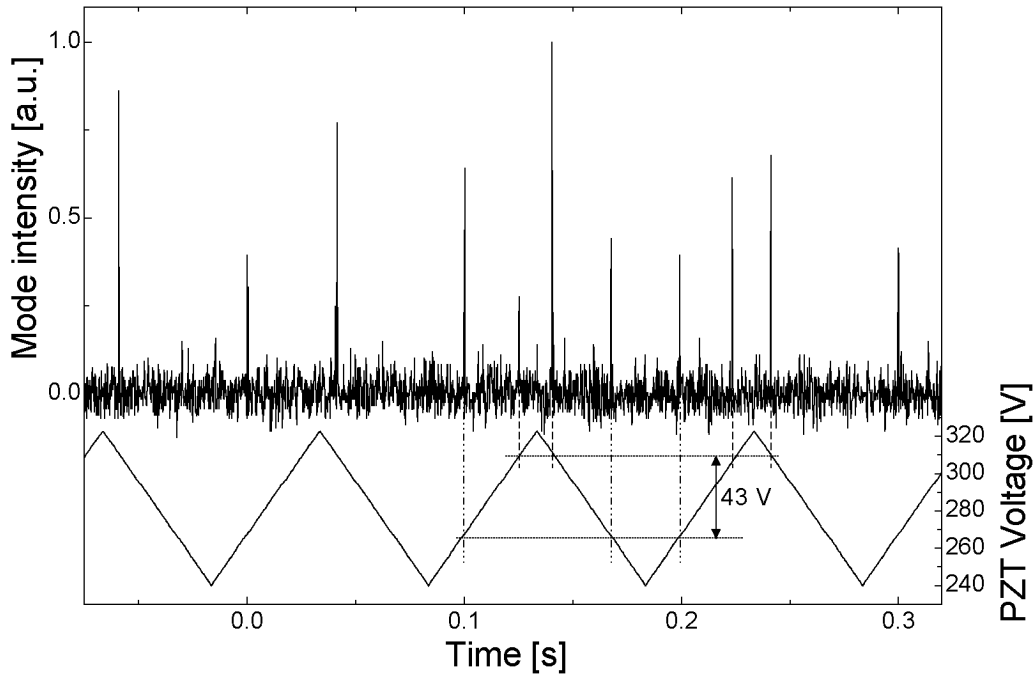Figure 3.10: Cavity mode spectrum

Recorded cavity mode spectrum by sweeping the cavity length by about 730 nm with a frequency of 10 Hz

3.3 Gas measurements

The following section concerns further characterization of the cavity ringdown setup and the detection of acetylene in synthetic air and in ethylene in view of applications in petrochemical industry as mentioned above in section 3.1.

3.3.1 Isotopomers

An appropriate method for testing the ECDL (EOSI) tuning behavior and the accuracy of the ringdown time acquisition of the near-infrared cavity ringdown setup (Fig. 3.1) is the determination of isotope ratios. Such a determination encloses a fine scan over two absorption lines of isotopes, the determination of the absorption coefficient and the determination of the absorption line area. For the determination of the acetylene isotopomer ratio of $^{12}C_2H_2$ and $^{13}C^{12}CH_2$, two absorption lines which are close together are chosen in order to record the absorption lines in a single scan.
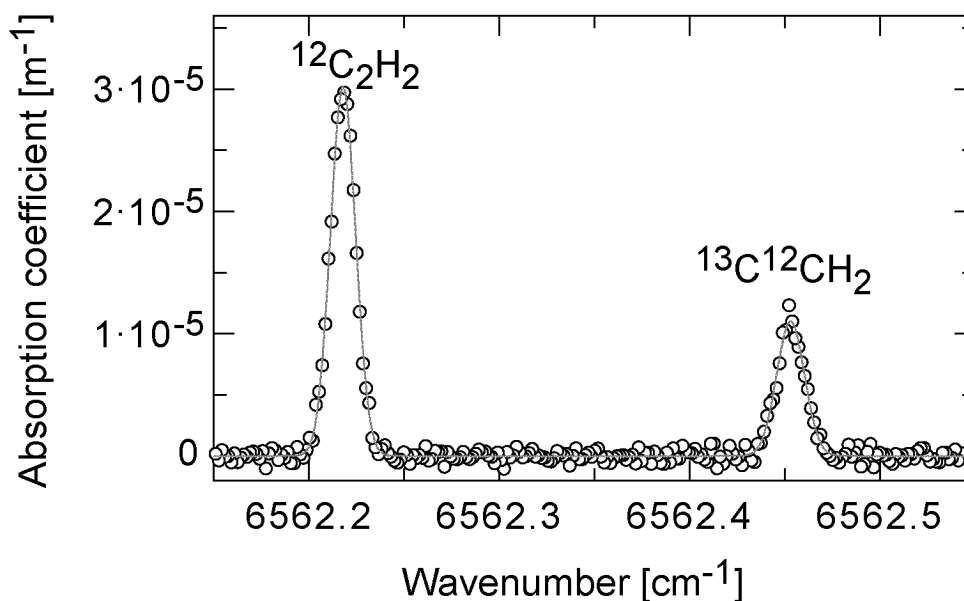

Figure 3.11: C_2H_2 isotopomer measurement

Absorption peaks of the $^{12}C_2H_2$ and $^{13}C^{12}CH_2$ molecules. Recorded spectrum (○), Gaussian fit (——)

Fig. 3.11 shows the recorded isotopomer measurement of 100 ppmV acetylene in synthetic air (O_2 20.5 %, H_2O < 5 ppm, KW < 0.1 ppm, NO_x < 0.1 ppm, CO and CO_2 < 0.5 ppm, N_2 rest) at a total pressure of 5 mbar. The low pressure prevents an overlapping of the two absorption lines.

In this measurement, 200 ringdown events were averaged for the evaluation of one ringdown time by the Matheson-Halmer algorithm. The laser output power was 1.4 mW. The strong absorption peak at 6562.2189 cm^{-1} is assigned to the R$_f$(14) line of the ^{12}C$_2$H$_2$ molecule whereas the weaker absorption line belongs to the R(8) line of the isotopomer ^{13}C^{12}CH$_2$ at 6562.4544 cm^{-1} [Hac02]. Due to the low gas pressure, the two absorption lines show pure Gaussian profile [Dem88]. Therefore, the recorded spectrum was fitted with two Gaussian curves resulting in a χ^2 of only 5.1·10^{-11} m^{-1}. This small value indicates the fine tuning behavior of the laser, i.e. of the PZT scan of the EOSI laser. By increasing the applied PZT voltage by 0.2 V after every ringdown time measurement, the wavenumber distance between two measured points amounts to 0.00165 cm^{-1} or about 0.4 pm. Since a PZT scan with an increment of 0.1 V is possible, a spectral resolution of 0.2 pm is achievable and thus, a high selectivity is warranted. In addition, no mode hopes are observed within a PZT scan. The ratio of the acetylene isotopomers ^{12}C$_2$H$_2$ and ^{13}C^{12}CH$_2$ was determined by the calculation of the area below the fitted curve resulting in a ratio of 2.47 ± 0.13 %. In literature, the natural abundance of this acetylene isotopomer ratio is given as 2.176 % [Hac02]. However, values of isotope ratios may vary at different locations. Therefore, a second measurement was performed in order to affirm the first ratio. The second ratio amounts to 2.44 ± 0.37 % which is very similar to the first value.

3.3.2 Gas mixture

After the confirmation of the good tuning behavior of the laser, a gas component in a gas mixture, i.e. 10 ppmV acetylene in 16 % CO$_2$, 0.85 % water vapour and synthetic air was measured at a total pressure of 20 mbar. The pressure was again chosen in such a way that there is no overlap between the different absorption lines of the gas components. We scanned the 6550 cm^{-1} range where the different components show their characteristic absorption lines with the PZT function of the EOSI laser at 1.4 mW. The recorded spectrum is given in Fig. 3.12. The measured spectrum is compared with the Hitran

database [Hit03], in which the absorption lines of acetylene are not available yet. We find an excellent agreement between the calculated CO_2 and H_2O absorption lines by Hitran and the measured spectrum. Once again, the tuning behavior and the progression of the spectrum are convincing. Furthermore, we could assign the absorption lines to the P(3) absorption line ($\nu_1 + \nu_3$ excitation) at 6549.328 cm^{-1} and to the R$_f$(8) line at 6549.935 cm^{-1} of acetylene [Hac02].
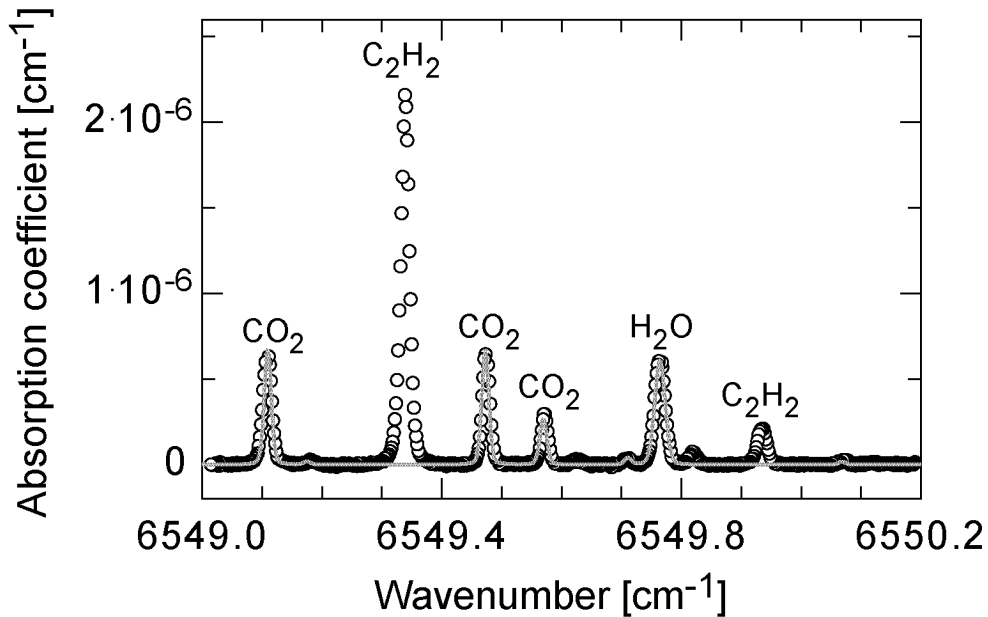

Figure 3.12: NIR spectrum of a gas mixture

Gas mixture of CO_2 (16 %), C_2H_2 (10 ppmV) and water (0.85 %) in synthetic air at a total pressure of 20 mbar and at room temperature. Measurement (o), Hitran (—)

3.3.3   Acetylene

As mentioned above in section 3.1, acetylene is one of the potential impurities during the ethylene production and therefore a potential trouble maker in the polymer plants. Since acetylene features a strong absorption behavior in the

1530 nm range, it is well suited for the characterization and the study of our near-infrared cavity ringdown system. The P-branch of the $\nu_1 + \nu_3$ excitations lies in the wavelength range between 1525 nm and 1544 nm [Gil01] whereas the R-branch is located in the 1511 nm - 1525 nm range. Since the tuning ability of our Santec ECDL covers completely the P-branch, an acetylene spectrum from 1525 nm up to 1544 nm was recorded with the cavity ringdown system presented in Fig. 3.1. 200 ringdown events were averaged every 5 pm and the ringdown events were analyzed by the Matheson-Halmer algorithm (see section 3.2.3). The laser output power amounted to 4 mW over the whole wavelength range and the cell was filled with 5 ppmV acetylene diluted in synthetic air at a total pressure of 300 mbar. The whole measurement lasted about 40 h due the averaging process and the high number of data points. The result is depicted in Fig 3.13 where the different absorption lines within the P-branch of acetylene are clearly detectable and identifiable [Hac02].
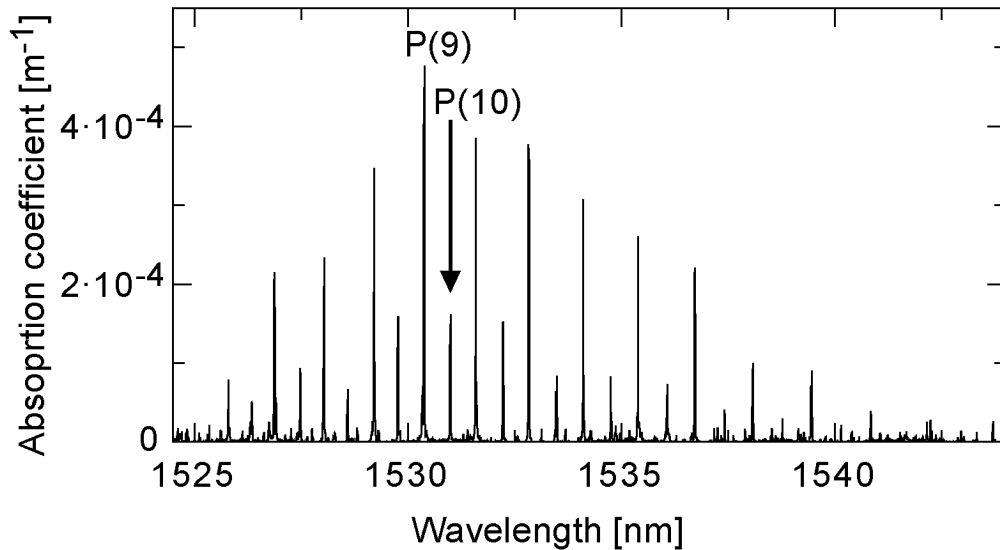

Figure 3.13: Measured NIR acetylene spectrum

5 ppmV acetylene (P-branch) diluted in synthetic air, from 1524.5 nm to 1544 nm at 300 mbar total pressure

Next, we focus our attention to the determination of the minimal detectable acetylene concentration with our setup. This was accomplished by recording the P(10) absorption peak of 10 ppmV acetylene at 1530.977 nm [Gil01] and at a total pressure of 100 mbar. This line provides a more accurate detection of the ringdown times at the corresponding concentration than the P(9) line whose absorption is too strong to record ringdown events at the peak of the line. In order to scan a narrow band in the near-infrared range, the EOSI laser was used whereby the mirror of the external laser cavity was finely tuned by a PZT, the output power was about 1.4 mW. The cell was filled with synthetic air and the baseline of the ringdown times was measured around the P(10) line of acetylene. The average ringdown time of the stable baseline in this range was determined as 28.3 μs with a standard deviation of the mean of 236 ns. Afterwards, the cell was filled with 10 ppmV acetylene diluted in synthetic air and the measurement was repeated. Figure 3.14 shows the result of the two measurements.
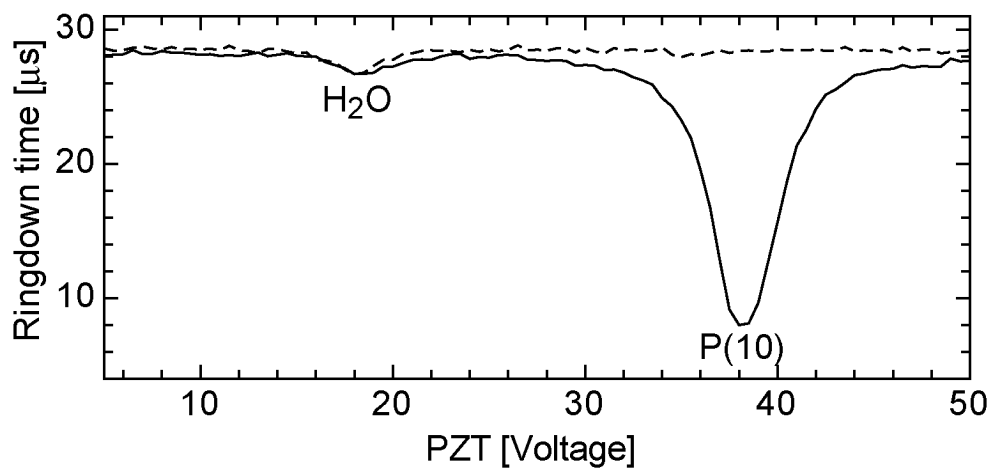

Figure 3.14: CRDS sensitivity evaluation

Synthetic air (equivalent baseline) (———), 10 ppmV acetylene in synthetic air (—) at a total pressure of 100 mbar

By taking a signal to noise ratio of 1 or 3, i.e. twice or 6 times the stan-

dard deviation, the minimum accurate deviation $\Delta\tau$ in the ringdown time (see Eq. 2.22) of the baseline is 472 ns or 1.42 μs. According to Eq. (2.26), this results in a minimum detectable absorption coefficient of $9.9 \cdot 10^{-7}$ m^{-1} or $6.2 \cdot 10^{-6}$ m^{-1}, respectively. Since the cavity was swept by a frequency of 10 Hz during the scan, the ringdown events were collected at a maximum rate of 20 Hz. Compared to the cavity mode spectrum (Fig 3.10), the applied voltage difference was reduced in order to excite only one fundamental longitudinal cavity mode. Hence, the minimum detectable absorption coefficient can also be written as $1.38 \cdot 10^{-8}$ cm^{-1} Hz$^{-1/2}$ for SNR = 3. This limit is independent of the absorption line selected because it is determined only by the ringdown time τ_o and its deviation $\Delta\tau$ as indicated in Eq. (2.26). Our minimum absorption value is higher than limits which were reported recently. In [He02], a noise-limited absorption sensitivity of $2.5 \cdot 10^{-9}$ cm^{-1} Hz$^{-1/2}$ in a 45 cm-long cavity was claimed at 1530 nm. Thereby, the collection rate of the ringdown events measured approximately 500 Hz. Assuming that we drive the PZT at its maximum frequency of 300 Hz, we would also achieve a sensitivity of $2.5 \cdot 10^{-9}$ cm^{-1} Hz$^{-1/2}$. However, the CRDS system presented by [He02] did not enclose a modulator but the cavity was swept only. Another paper [Bae02] stated a CRDS detection sensitivity of even $3.1 \cdot 10^{-11}$ cm^{-1} Hz$^{-1/2}$ in the near infrared range. This result was achieved in an off-axis configuration at 500 Hz rate, with 10^4 sweep average, and at 1565 nm. The cell was 0.88 m long. The reason for the lower sensitivity achieved in our setup is found in the cell design. The cavity alignment described in section 3.2.2 proves to decrease the sensitivity considerably. The pressure difference applied on the mirror affects the accuracy of the ringdown time acquisition. Therefore, a cell totally enclosing the mirrors would increase the sensitivity performance but deteriorate the handling and alignment comfort. In view of the use of the setup in a petrochemical industry, these features can not be neglected. Further improvements are proposed later in the outlook.

The measured absorption peak of the P(10) acetylene line in Fig. 3.14 is fitted by a Lorentz curve due to the gas pressure of 100 mbar [Dem88] and
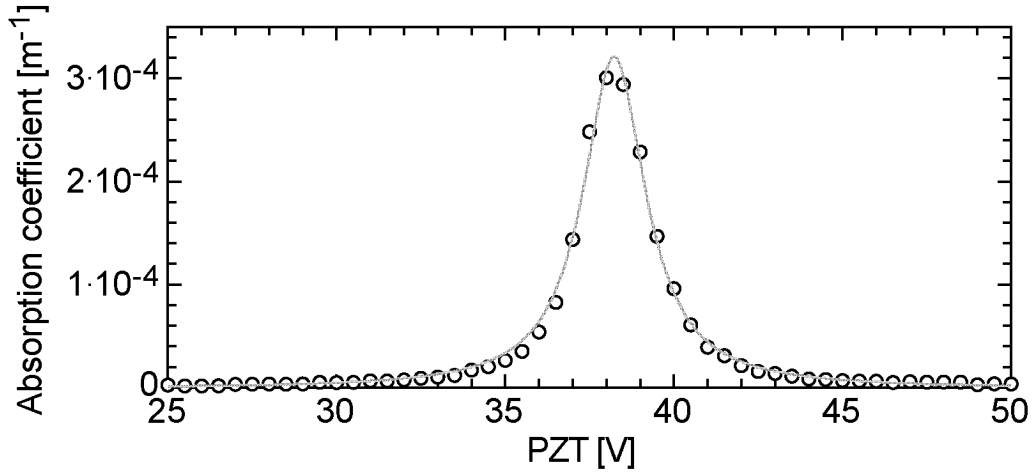
Figure 3.15: P(10) absorption peak

10 ppmV acetylene in synthetic air at a total pressure of 100 mbar. Measured P(10) absorption peak (○), Lorentz fit (—)

the maximum absorption coefficient of this fit, i.e. $3.21 \cdot 10^{-4}$ m^{-1}, corresponds to 10 ppmV of acetylene (see Fig. 3.15). Unfortunately, Hitran does not provide any data about acetylene in the near-infrared range yet. In order to evaluate the detection limit, we divide the maximal coefficient by $6.2 \cdot 10^{-6}$ m^{-1} (SNR = 3) and get a minimum detection limit of acetylene diluted in synthetic air of 193 ppbV at the P(10) line and at a total pressure of 100 mbar. Since the cross section of the stronger P(9) absorption line (1530.3718 nm [Gil01]) is 2.877 times [Hac02] larger than the P(10) one, it results an acetylene detection limit of 67 ppbV at 100 mbar.

3.3.4   Gas flow

In order to characterize the CRDS setup in a gas flow configuration, i.e. in a real-time monitoring configuration as it would come into operation in an industrial plant, acetylene was mixed with a synthetic air stream in a mass flow controller (Sierra Instruments Inc.). The mixture then flowed through the 52 cm-long cavity ringdown cell at a flow rate of 200 cm^3/min. The total cell

pressure was kept at 20 mbar during the flow procedure. However, first pure synthetic air was flown through the cell to record the baseline and its noise. Thereby, the wavelength of the Santec ECDL featured an output power of 7 mW whereby the wavelength of the laser was set on the strong P(9) absorption line of acetylene. Then, the acetylene concentration was increased in steps of 250 ppbV, later in steps of 500 ppbV with the mass flow controller every 5 min and the corresponding ringdown times were recorded. After 80 minutes, the acetylene concentration was set to zero again for checking the response time of the arrangement and the flow effect on the cavity alignment, i.e. on the baseline. The result of the 90 min-long measurement is depicted in Fig. 3.16.
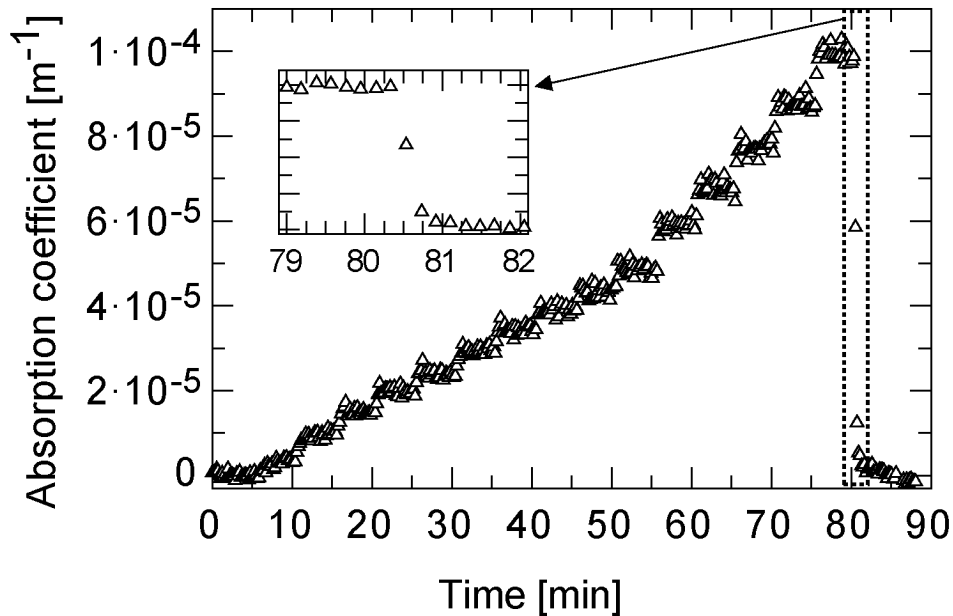

Figure 3.16: Acetylene flow measurement with synthetic air

Gas flow measurement of different acetylene concentrations in synthetic air. The flow rate amounts to 200 cm^3/min at 20 mbar total cell pressure. Inset: Magnification of the last few minutes where the setup response time of less than one minute is shown.

Every step of the small concentration increase can be resolved even at low concentrations and after 80 min, the measured absorption coefficient goes back to its original value. This indicates that the cavity alignment has not changed during the measurement. Furthermore, we find a response time of less than about a minute (for an absorption coefficient decrease of more than 90 %). Considering the cell volume of 540 cm^3 and the gas flow of 200 cm^3/min, this short time astonishes. Even if taking into account a dead volume of the cell of about 50 cm^3, the short response time is not completely understood yet.

The same procedure was not only done at the strong P(9) absorption line but also at the P(10) line featuring a smaller cross-section. Therefore, the measurement of the absorption coefficient at this line is more suitable when higher concentrations have to be measured. In this case, the acetylene concentration was increased in steps of 2.5 ppmV. A sharp step profile of the absorption coefficient is also found for the P(10) acetylene line. The recorded absorption coefficients of the P(9) and P(10) absorption lines are plotted versus the acetylene concentration and are given in Fig. 3.17.

The absorption coefficients of both lines show very good linear behavior whereby the extracted gradient of the P(9) line amounts to $1.97 \cdot 10^{-5}$ m^{-1} per ppmV. Considering the baseline noise of the first 5 minutes in our flow measurements (Fig. 3.16), we find a standard deviation of the ringdown time of $8.79 \cdot 10^{-8}$ s ($\tau_o = 23.20$ μs) resulting in a detection limit of $\alpha_{min} = 3.45 \cdot 10^{-6}$ m^{-1} (SNR = 3) (see Eq. 2.26). This limit is slightly lower than the one found in the previous spectrum measurement (Fig. 3.14) caused by a different alignment of the cavity. By taken into account the evaluated gradient of the P(9) line, the minimum acetylene detection limit in a flow configuration is 175 ppbV with synthetic air as background gas at a total cell pressure of 20 mbar. The standard deviation of the ringdown time in the measurement at the P(10) line is $1.079 \cdot 10^{-7}$ s ($\tau_o = 23.27$ μs). Hence, the limit amounts to $4.14 \cdot 10^{-6}$ m^{-1} (SNR = 3). The gradient of the P(10) absorption line is $8.04 \cdot 10^{-6}$ m^{-1} per ppmV resulting in a higher minimum detection limit of 514 ppbV at 20 mbar. The ratio of both gradients amounts to 2.45, which
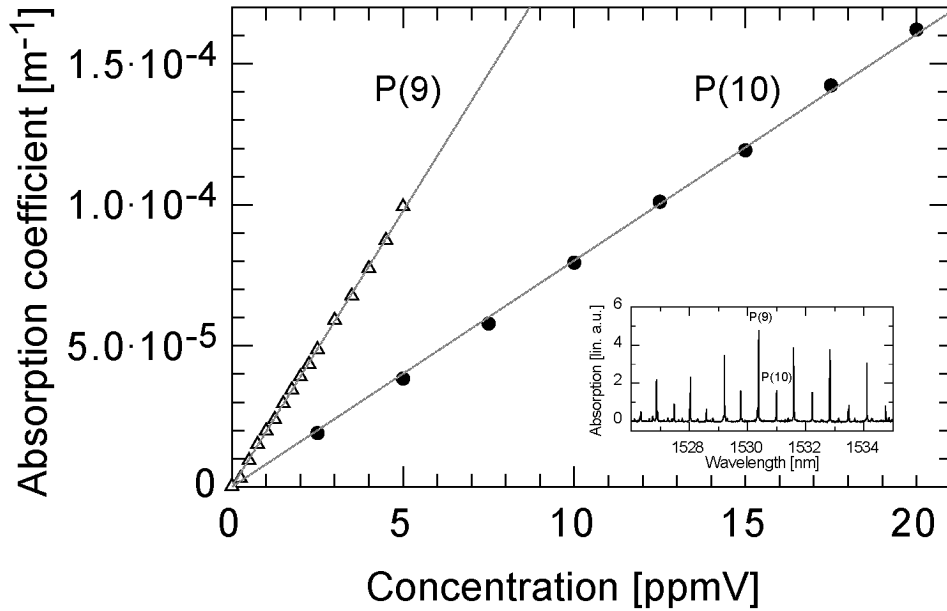
Figure 3.17: Linearity of C_2H_2 concentrations in synthetic air

Measured absorption coefficients vs. acetylene concentrations in synthetic air. The coefficients show very linear behaviors in respect to the concentration. P(9) absorption line of acetylene features a gradient of $1.97 \cdot 10^{-5}$ m^{-1} per ppmV and the P(10) line a gradient of $8.02 \cdot 10^{-6}$ m^{-1} per ppmV. Inset: Recorded spectrum around the P(9) and P(10) absorption lines of acetylene

is slightly lower than expected, since the gradient ratio corresponds to the ratio of the absorption cross-sections which is 2.88 [Gil01]. The reason for the smaller ratio can be found in the frequency of the Santec ECDL which is not totally coincident with the exact frequency of the absorption peaks.

3.3.5 Acetylene in ethylene

A ringdown time baseline for synthetic air was measured in the range of the P(9) line of acetylene and afterwards, the synthetic air was replaced by 99.95 % pure ethylene (C_2H_4). The range around the P(9) absorption line was scanned

again using the fine tuning opportunity provided by the EOSI laser. The output power of the laser was 1.4 mW. We averaged 100 ringdown events for the evaluation of one ringdown time at one piezo position. The total cell pressure amounted to 20 mbar. After this scan, the measurement was repeated under the same condition apart from additional 10 ppmV acetylene diluted in ethylene. Both obtained spectra are given in Fig. 3.18. We find a good congruence of the two spectra beside the P(9) acetylene line at 1530.3718 nm [Gil01]. The additional absorption at 1530.3718 nm caused by acetylene is accurately detectable. The total difference in the absorption coefficients is $2.0 \cdot 10^{-4}$ m^{-1} corresponding to $2.0 \cdot 10^{-5}$ m^{-1} per ppmV. This value is very close to the gradient found in Fig. 3.17. This emphasizes the reliability of our setup with respect to an accurate determination of absolute absorption coefficients. However, since the repeatability of the laser tuning is not perfect, the positions of the absorption peaks were manually shifted over each other. Furthermore, a small concentration of synthetic air was also introduced in the gas cell with the adding of acetylene. As a consequence, the absorptions in the mixed spectrum are slightly lower than in pure ethylene. In addition, the spectra show that the laser absorption within pure ethylene is never equal zero, i.e. the recorded ringdown times are always shorter than the ringdown times acquired in the cell filled with synthetic air. This means that it is not possible to determine the absolute acetylene concentration but the *additional* concentration only. The superposition of different absorption lines of different gas components within the mixture which are not completely known in advance prevents the determination of the absolute concentration.

In order to reduce the overlap of the different absorption lines, a pure ethylene and an acetylene-ethylene mixture spectra are measured at a pressure of only 5 mbar. This time, the wavelength range around the P(3) line of acetylene (6549.328 cm^{-1} [Hac02]) is considered. Figure 3.19 depicts both spectra which agree very well again apart from the additional absorption peak caused by the added 10 ppmV acetylene in the 99.95 % pure ethylene gas.

In spite of the low total pressure in the cell, all the different absorption
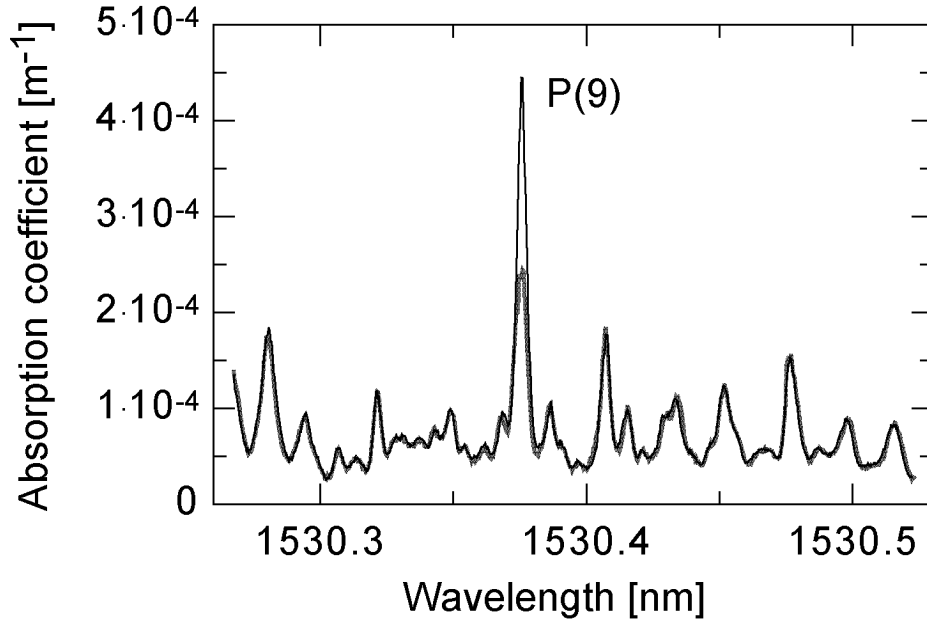
Figure 3.18: Acetylene-ethylene mixture spectrum around P(9)

99.95 % pure ethylene (——), 99.95 % pure ethylene plus 10 ppmV acetylene diluted in synthetic air (——). Both spectra are recorded around the P(9) acetylene line with the EOSI ECDL at 20 mbar total gas pressure. Apart from the additional acetylene absorption, evident at the P(9) line, the two spectra exhibit excellent agreement.

lines are still overlapping preventing an absolute concentration determination of one component. However, the absorption of the added acetylene is clearly detectable.

A flow measurement of different acetylene concentrations in ethylene instead of synthetic air was also performed with the Santec laser at an output power of 7 mW. The flow rate amounted again to 200 cm^3/min at a total cell pressure of 20 mbar. 100 ringdown events were averaged for each data point before the computer analyzed the ringdown times. The flow started with 180 cm^3/min 99.95 % pure ethylene and 20 cm^3/min synthetic air. Every 5 minutes, 500 ppbV acetylene were added to the ethylene-synthetic air mixture. After 55 min corresponding to a total addition of 5 ppmV of acety-
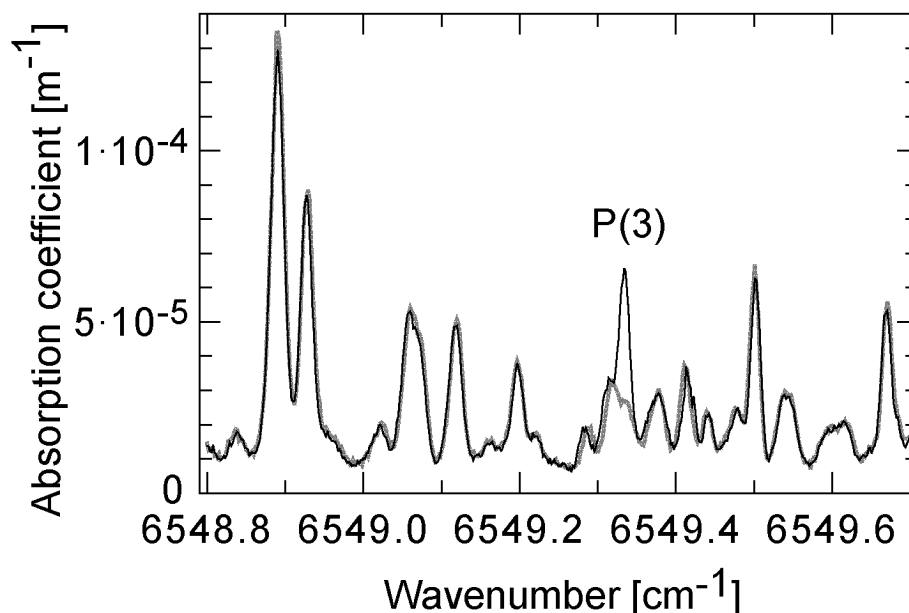
Figure 3.19: Acetylene-ethylene mixture spectrum around P(3)

99.95 % pure ethylene (——), 99.95 % pure ethylene plus 10 ppmV acetylene diluted in synthetic air (——). Both spectra are recorded around the P(9) acetylene line with the EOSI ECDL at 20 mbar total gas pressure. Apart from the additional acetylene absorption, evident at the P(3) line, the two spectra exhibit excellent agreement.

lene, the cell was flushed again with the pure ethylene-synthetic air mixture. Figure 3.20 shows the flow rate of the different gases connected to the mass flow controller (Sierra Instruments Inc.).

The evaluated absorption coefficients at the P(9) line during the 1 h-lasting measurement are depicted in Fig. 3.21. At the beginning, the measured ringdown time in pure ethylene and synthetic air is only about 11.72 μs due to a strong absorption in this range (see Fig. 3.18). The standard deviation of the ringdown time is 107 ns. Hence it results a minimum detectable absorption coefficient $\alpha_{min} = 1.65 \cdot 10^{-5}$ m^{-1} at the P(9) line and at a total pressure of 20 mbar. This value is higher than the limit of $\alpha_{min} = 3.45 \cdot 10^{-6}$ m^{-1} ob-
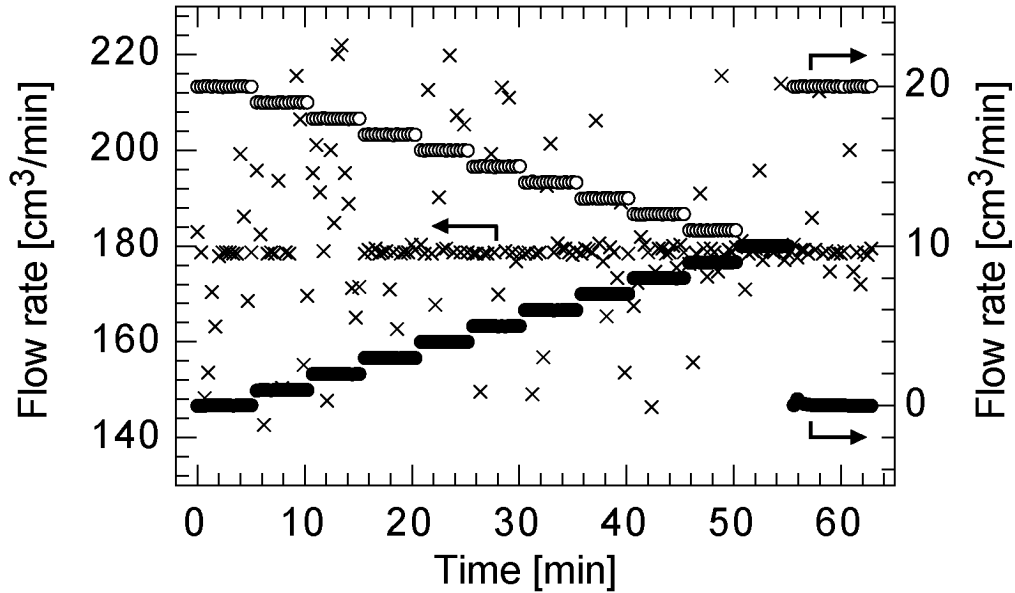
Figure 3.20: Gas flow rate during measurement

Gas flow rate during the measurement of different acetylene concentrations in ethylene. The total flow rate amounts to 200 cm^3/min at 20 mbar total cell pressure: 99.95 % ethylene flow rate (×; left axis), synthetic air flow rate (○; right axis), 100 ppmV acetylene diluted in synthetic air flow rate (●; right axis)

tained for acetylene in synthetic air. This difference can be explained by the additional absorption in ethylene, i.e. on the short ringdown time and on the resulting low ratio of $\Delta\tau/(\tau_o - \Delta\tau)$ in Eq. (2.26). Furthermore, the response time is again determined to about 1 min.

In addition, the measured absorption coefficient vs. the concentration is plotted and its linearity is verified. An excellent linear behavior is found once again and the fit procedure extracts a gradient of $3.58 \cdot 10^{-5}$ m^{-1} per ppmV. Thus, a detection limit of 460 ppbV for additional acetylene is achieved in an ethylene stream. The result is depicted in Fig. 3.22. The considerably steeper gradient compared to the case of acetylene in synthetic air is not completely understood yet. The apparent strong variation of the ethylene flow rate (see
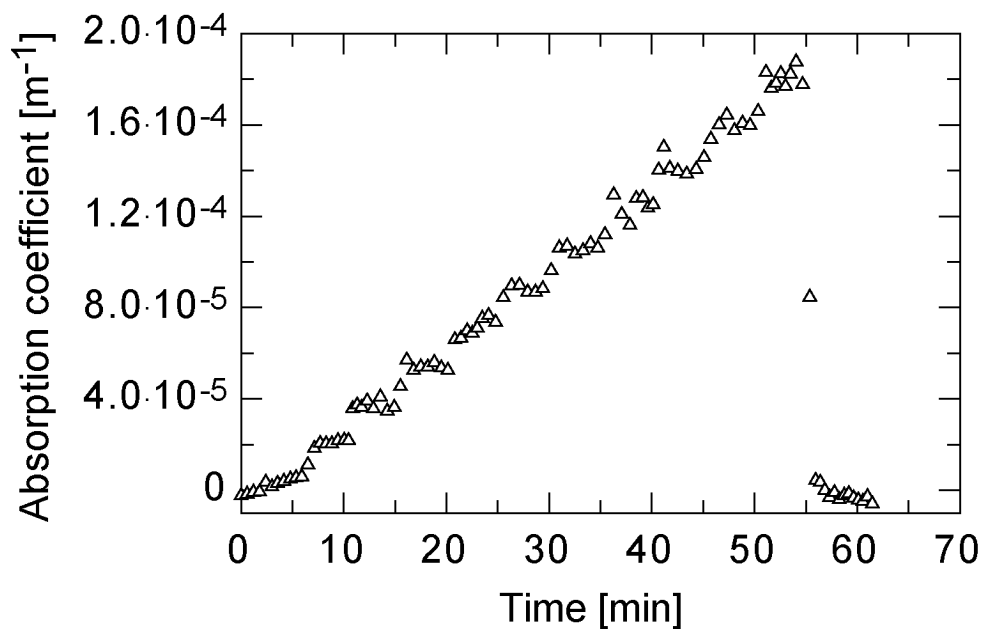
Figure 3.21: Gas flow measurement in ethylene

Gas flow measurement of different acetylene concentrations in ethylene. The flow rate amounts to 200 cm^3/min at 20 mbar cell pressure.

Fig. 3.20) affects an accurate determination of the additional acetylene concentration and thus, a strong deviation from a linear behavior but not from its slope itself would be expected.
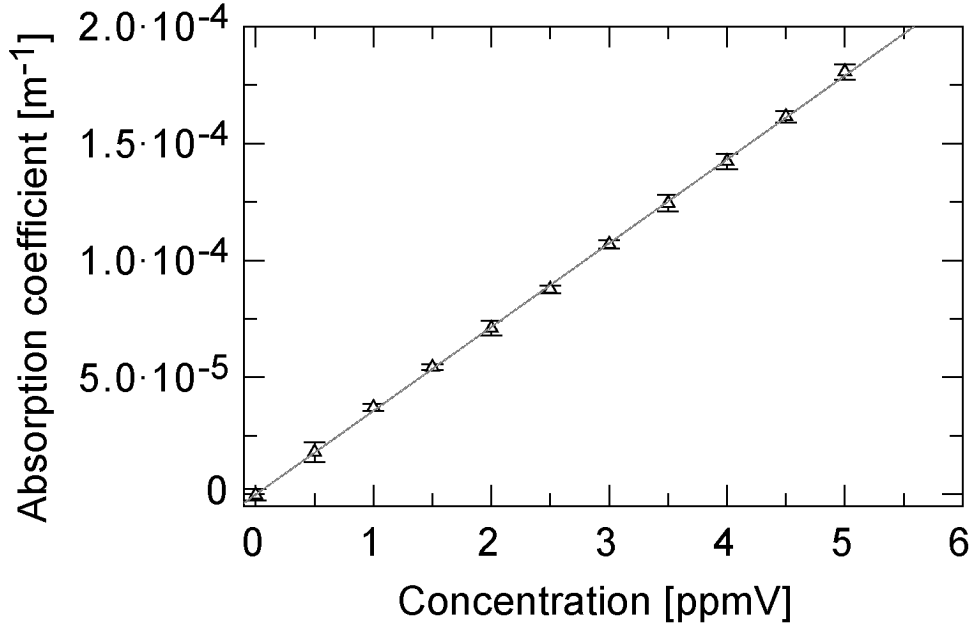
Figure 3.22: Linearity of C_2H_2 concentrations in ethylene

Measured absorption coefficients vs. acetylene concentrations in ethylene. The coefficients show a very linear behavior in respect to the concentration. P(9) absorption line of acetylene features a gradient of $3.58 \cdot 10^{-5}$ m^{-1} per ppmV in ethylene.

3.4 Conclusion

A near-infrared based cavity ringdown system was designed and built-up for the potential use in petrochemical industries. The design enclosed a reliable and cost-effective near-IR laser with a power of only a few mW, telecommunication approved fibers and a homemade gas cell providing an user-friendly cavity alignment. The cavity was formed by mirrors featuring a reflectivity of about 99.99 % and a curvature radius of 1 m. The distance between the mirrors amounted to 52 cm. An acetylene isotope was determined with good accuracy and a minimum detectable absorption coefficient of $6.2 \cdot 10^{-6}$ m^{-1} (SNR = 3) was achieved in a hermetically sealed gas cell. With a cavity modulation frequency of 10 Hz, a sensitivity of $1.38 \cdot 10^{-8}$ cm^{-1} $Hz^{-1/2}$ could be

reported. Furthermore, different components of a gas mixture were quantitatively and qualitatively analyzed and we found a very good agreement between the recorded spectrum and the Hitran database [Hit03]. In order to check our setup for its potential use in the petrochemical industry, acetylene diluted in synthetic air as well as in ethylene were measured in a gas flow configuration. An acetylene detection limit of 175 ppbV in synthetic air was evaluated and concentration differences of 250 ppbV were easily detectable in a stepwise concentration increase. Moreover, a detection limit for an additional acetylene concentration of 460 ppbV in ethylene was achieved and acetylene concentration increases of 500 ppbV were gradually resolved. Excellent linear behaviors of the absorption coefficients with respect to different acetylene concentrations in synthetic air and in ethylene were presented. However, the opportunity to align the cavity from outside the closed gas cell limited the sensitivity of this near-infrared setup considerably. In order to replace the gas chromatographs in petrochemical facilities, the detection limit and the stability of the cavity alignment are not sufficient yet. Nevertheless, useful information could be gained by this setup showing the way for further improvements which are described in the next section.

3.5   Outlook

In order to improve the sensitivity of our near-infrared based cavity ringdown system, the mirrors forming the cavity should be completely enclosed within the gas cell. Hence, no pressure difference will take effect on the mirror alignment during a measurement and this is believed to minimize the standard deviation of the acquired ringdown times. This improvement, however, would lessen the user-friendliness of the setup. Therefore, a self-alignment system based on a near-infrared camera could also be considered. Such a camera is able to detect the mode pattern on the mirror and hence, a correct or incorrect alignment of the cavity. Furthermore, one mirror could be fixed on a computer-controlled mirror mount which would automatically align the cavity by a camera feedback loop. A cavity self-alignment system is, however, only

realizable in case of a single-ended detection scheme. Such a scheme is the so-called optical heterodyne detection (OHD) in which the light reflected by the entry mirror interferes with the light leaking out of the cavity and generates an OHD signal which decays exponentially twice as slow as the cavity ringdown time. Hence, the decay time of this signal can be determined more accurately than the cavity ringdown time. The interference is due to the light frequency shift within the cavity caused by the moving mirror, i.e. by the Doppler effect. Apart from the slower OHD signal decay, another advantage of this scheme concerns its amplitude which is larger than the measured amplitude in a forward propagation detection due to the interaction of the intense reflected light with the light leaking out of the cavity. Both aspects improve the sensitivity of the cavity ringdown experiment. However, polarization control devices like beamsplitters or fiber-based circulators have to incorporate in heterodyne cavity ringdown experiments whereas no modulator is used anymore. More details about the OHD scheme applied in a cavity ringdown system can be found in [He02]. We think that the implementation of the OHD system would improve the detection sensitivity to the level required by the petrochemical industry.

Chapter 4

Fiber Cavity Ringdown Technique

4.1 Introduction

Not the demand for new high-capacity information transmission devices, but the fabrication purpose of fiber sensors gave reasons for the development of optically low-loss fibers in the 1960s. Since that time, numerous of researchers have focused their work on the development and on the production of a variety of fiber sensors providing an effective measurement of mechanical, chemical, biological and environmental parameters. The most familiar subdivisions of actual fiber sensors, namely of extrinsic and intrinsic fiber sensors, and their application fields are listed in Figs. 4.1 and 4.2 [Udd91]. In an extrinsic fiber sensor, the light is guided in a fiber indeed but the light interaction with the sample takes place outside the fiber. Contrary, in an intrinsic fiber sensor, the sensing element is embedded in the fiber itself. Intrinsic sensor applications include the measurement of rotation, strain, acoustic emissions, and vibration whereas extrinsic sensors are used more often for the linear and angular positioning in aircraft fly-by-light systems or to control processes by monitoring temperature, pressure, liquid level or flow rate. However, all fiber sensors have familiar characteristics: they are lightweight, low cost, immune to electromagnetic interference, they do not generate electrical hazards and they are

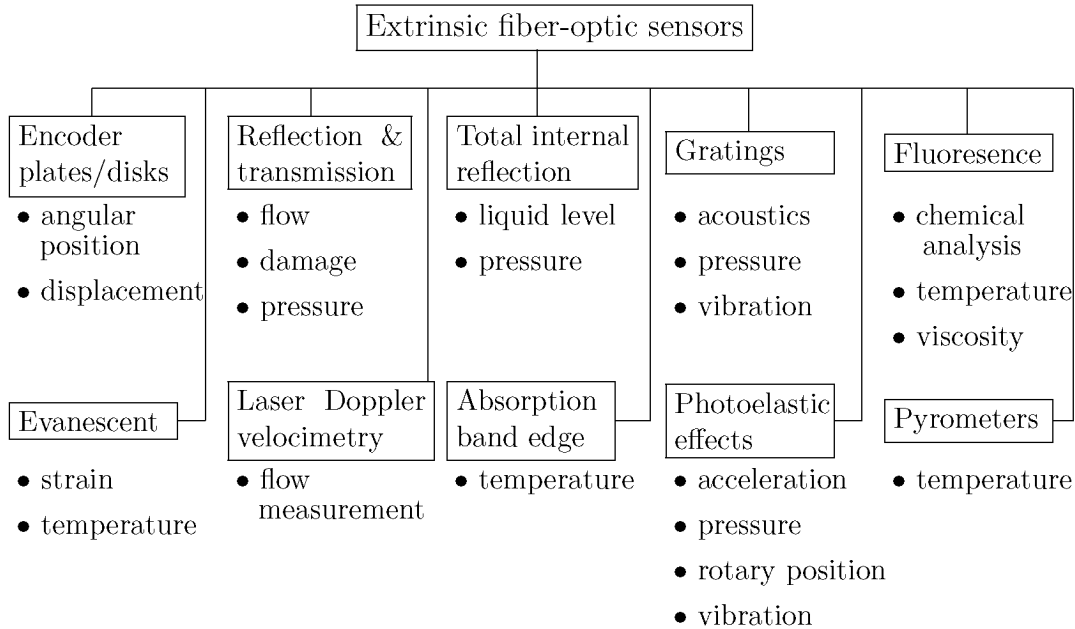compact, and as a result, they are minimally invasive [Gra00].

```
                    ┌─────────────────────────────┐
                    │ Extrinsic fiber-optic sensors │
                    └─────────────────────────────┘
```

Encoder plates/disks	Reflection & transmission	Total internal reflection	Gratings	Fluoresence
• angular position • displacement	• flow • damage • pressure	• liquid level • pressure	• acoustics • pressure • vibration	• chemical analysis • temperature • viscosity

Evanescent	Laser Doppler velocimetry	Absorption band edge	Photoelastic effects	Pyrometers
• strain • temperature	• flow measurement	• temperature	• acceleration • pressure • rotary position • vibration	• temperature

Figure 4.1: Extrinsic fiber-optic sensors

Subdivisions of extrinsic fiber-optic sensors and their application fields (after [Udd91])

One kind of intrinsic fiber-optic sensors uses fiber resonators as sensing elements whose studies have started in the early 1990s. First fiber resonators were created by fixing optical single-mode fibers between two mirrors. In this way, the feasibility of single-mode fibers in a Fabry-Perot geometry was demonstrated for metrology of single-frequency laser sources [Fra81] and in the same year, the sensitive behavior of fiber-optic Fabry-Perot interferometer with respect to phase modulation was reported [Pet81]. However, the finesse of such a resonator was very poor, just around 20. Even so, fiber interferometer schemes for sensor applications have been studied further and shortly after that, fiber-optic Fabry-Perot interferometers formed by coated end faces with a multilayer of dielectric films were tested for temperature, mechanical vibration, acoustic
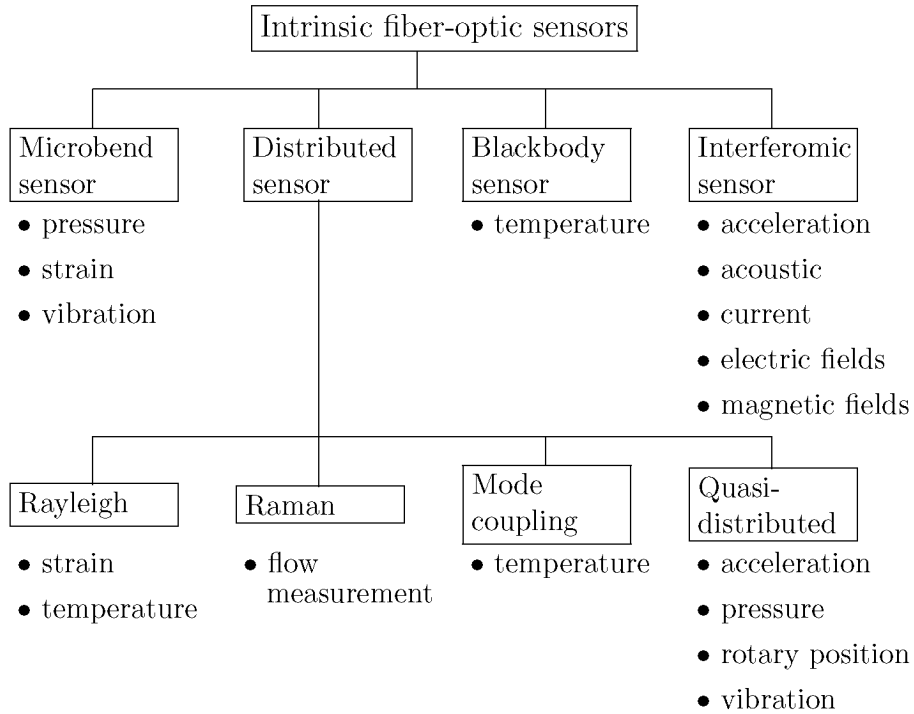
```
                    ┌─────────────────────────────┐
                    │  Intrinsic fiber-optic sensors │
                    └─────────────────────────────┘
```

Microbend sensor	Distributed sensor	Blackbody sensor	Interferomic sensor
• pressure • strain • vibration		• temperature	• acceleration • acoustic • current • electric fields • magnetic fields

Rayleigh	Raman	Mode coupling	Quasi- distributed
• strain • temperature	• flow measurement	• temperature	• acceleration • pressure • rotary position • vibration

Figure 4.2: Intrinsic fiber-optic sensors

Subdivisions of intrinsic fiber-optic sensors and their application fields (after [Udd91])

wave, voltage and magnetic field sensors [Yos82].

An improvement of the fiber cavity finesse was achieved when a fiber cavity was formed by the newly developed fiber directional couplers. "Single-mode optical fibers can be used to make a high-finesse optical resonator forming a short piece of fiber into a closed ring to constitute a low-loss cavity [Sto82i]." A finesse of 80 was measured within the formed fiber loop resulting in an expected cavity decay time of 25 ns per meter [Sto82i]. However, the ringdown time was only used for the estimation of the coherence length of the laser source in order to achieve resonant effects in the loop. These effects are similar to the effects in a Fabry-Perot resonator, i.e. sharp maximal output power whenever the optical input frequency matches the resonant condition. Furthermore, the fiber loop was extended with a phase modulator driven by a triangular wave

to ensure the fulfillment of the resonant condition and to achieve a resonator behavior similar to a scanning Fabry-Perot interferometer. In our open-path experiment, we fulfilled the resonant condition by scanning the cavity with a PZT as described in section 3.2. At that time, the authors believed to have found a good instrument for optical filters and spectrum-analyzers especially for nonlinear optics for which the high circulating-power enhancement and low cavity loss are ideal. However, there was no mention for using fiber resonators for spectroscopic applications.

A first fiber-based spectrum was finally recorded with an intra-cavity fiber laser scheme in 1993 [Böh93]. A broadband Nd^{3+}-doped fiber inserted in an external cavity was operated as an optically pumped laser. This scheme allowed a spectroscopic measurement of atmospheric absorption around 1100 nm by a stepwise tuning of an intra-cavity prism. An equivalent absorber path length of 15 km was reported for a 2 m-long doped single-mode fiber highlighting the advantage of cavity-enhanced spectroscopy.

But not only the fiber technology has moved towards spectroscopic applications but also the cavity ringdown technology has headed towards cavities within bulk materials. In 1997, an evanescent wave cavity ringdown spectroscopy with a total-internal-reflection (TIR) minicavity was proposed. A monolithic, polygonal, TIR-ring resonator enabled an extension of the cavity ringdown concept to surfaces, thin films, liquids and condensed matter spectroscopy [Pip97₁]. Shortly after, this proposal was demonstrated and surface processes were probed by cavity ringdown method through the absorption of the evanescent wave [Pip97₂]. (see also section 2.1). (At this place, we will not consider other works in the field of intra-cavity laser absorption spectroscopy. A reader interested in this subject will find more information in [Rom99].)

A first combination of the fiber technology with the cavity ringdown method was finally achieved in 2001. Cavity ringdown loss measurements were realized in an optical fiber loop. The loop had a length of several tens of meter and a 5 cm open path micro-optical gas cell for trace gas monitoring was incor-

porated in this loop [Ste01]. The high losses due the the cell coupling were compensated by a piece of an erbium-doped fiber in the loop. Pulsed as well as continuous-wave cavity ringdown measurement were demonstrated with this experimental setup.

The begin of the fiber cavity ringdown study in our laboratory falls also in this time. The idea of forming a fiber cavity by coating fiber end facets of fiber connectors with a dielectric mirror was patented in 2000 [Ler00] and a first feasibility study of the fiber cavity ringdown scheme was published in 2002 [Ler02₁]. Further studies of the fiber cavity ringdown technique done in our group are discussed in the following.

4.2   Theoretical consideration

The implementation of the cavity ringdown scheme into fibers demands for an extension of the previous cavity ringdown theory (see chapter 2) since the cavity is within an absorbing bulk material. In this case, the exponential decay time depends on both the reflectivity of the mirrors forming the cavity and the losses due to the absorbing medium between the mirrors. At the beginning, we consider a fiber cavity without an additionally induced loss, i.e only with the absorbing bulk material. According to [Bus99], Eq. (4.1) gives the ringdown time τ corresponding to a straight fiber cavity:

$$\tau = \frac{t_r}{2\left[\left(1 - \tilde{R}\right) + \alpha_o L\right]} = \frac{L n_{eff}}{c_o\left[\left(1 - \tilde{R}\right) + \alpha_o L\right]}, \qquad (4.1)$$

where t_r denotes the photon transit time for a single round trip in the fiber cavity and $\tilde{R} = \sqrt{R_1 R_2}$ is a measure of the mirror reflectivities R_i ($i = 1, 2$). The intrinsic loss coefficient of a straight fiber is given by α_o [m^{-1}] and L stands for the fiber cavity length. The speed of light in vacuum

is given by c_o and n_{eff} represents the effective group index of refraction in the fiber. Since $\tilde{R}$, α_o and n_{eff} are wavelength-dependent, the ringdown time τ is also a function of the wavelength. When an additional loss is introduced into the fiber cavity, e.g. by bending the fiber cavity or by exposing the fiber cavity to gaseous hydrogen, Eq. (4.1) has to be further modified resulting in a ringdown time τ_B:

$$\tau_B = \frac{t_r}{2\left[\left(1 - \tilde{R}\right) + \alpha_o L + \alpha_B l\right]},\tag{4.2}$$

where α_B [m^{-1}] denotes the additional loss coefficient and l is the length within the cavity where the additional loss takes place. The coefficient α_B is therefore in consideration of Eqs. (4.1) and (4.2):

$$\alpha_B = \frac{L n_{eff}}{l c_o}\left(\frac{1}{\tau_B} - \frac{1}{\tau}\right).\tag{4.3}$$

Equation (4.2) implies that a loss increase inside the cavity yields a ringdown time $\tau_B < \tau$. An additionally induced low optical loss within a fiber cavity can be determined more accurately with this method than a high loss since the longer the ringdown time the more accurate it can be measured. However, as discussed above in subsection 2.2.2, the ringdown time standard deviation $\Delta\tau$ of the cavity limits the sensitivity of the fiber cavity ringdown scheme expressed by the minimum detectable additional absorbance $(\alpha_B l)_{min}$ per cavity pass (see Eq. (2.26)). For a small number of ringdown time measurements, we consider the student's t-distribution and get, according to [Bus99], the following expression for the minimum detectable additional absorbance in a fiber cavity:

$$(\alpha_B L)_{min} = \frac{L n_{eff} \, \mathrm{t} \, \triangle \, \tau}{c_o \tau^2} \sqrt{\frac{2}{m}}, \qquad (4.4)$$

where m denotes the number of measurements yielding the average value of the ringdown time τ and t is the value of the student's t-distribution for $2m$ - 2 degrees of freedom for the desired confidence level. Consequently, bending losses are obtained by recording the ringdown times corresponding to a straight and a bent fiber cavity while the minimal detectable absorbance is derived from the ringdown time standard deviation of the straight fiber cavity.

4.3 Fiber-optic cavity sensing of bending loss

The trend to shrink packaging of optical components demands for fibers with small optical bending losses. Therefore, fiber manufacturers are focusing a lot of their research efforts on the development of fibers for tight-bend-radii applications [Fre03]. The test procedure for measuring optical macrobend attenuation in a fiber usually consists in wrapping 100 turns around a mandrel featuring a diameter of 50 mm. With such a wrapping, the typical induced loss in a standard silica-based single-mode fiber is less than 0.1 dB at 1550 nm [Cor1]. This corresponds to an optical attenuation of less than $6.37 \cdot 10^{-3}$ dB/m in the 15.7 m long coiled fiber. Special bend-insensitive fibers winded 30 turns on a mandrel with a 10 mm radius even show an additional, i.e. bend-induced, loss of < 0.05 dB at 1550 nm [Sto]. Hence, the determination of such a low loss requires a sensitive and reliable optical fiber measurement method. One approved technique is the well-known cut-back method [Mar81]. In this technique, the radiation of a suitable light source is coupled into a fiber at one end and a detector registers the optical output power at the other end of the fiber. Next, the fiber is cut back and the output power is measured again without changing the light source, detector or launch conditions. The ratio between the two different optical output powers allows the calculation of the optical

loss within the cut-away fiber. Unfortunately, this method destroys the fiber.

In this chapter, we present the promising, sensitive and nondestructive fiber cavity ringdown (FCRD) scheme as a novel method to measure optical attenuation in fibers. Bending losses in silica-based single-mode fiber cavities were analyzed with the cavity ringdown technique and compared with a theoretical model for the first time. The experimental results, advantages and limitations of this technique are discussed in the following sections.

4.3.1   Bending loss in a silica-based single-mode fiber

Fiber bending reshapes the guided field in the fiber core resulting in an increase of radiative outpropagating power, i.e. in additional optical losses. Bending losses do not show a smooth exponential increase with decreasing curvature radius as claimed by a first theoretical consideration in 1976 [Mar76], but a typical modulation [Mur78]. The modulation is due to coherent coupling between the core-propagating field and the fraction of radiated field reflected by the cladding coating or coating air interfaces.

According to [Fau97], a theoretical expression which describes bending losses in single-mode fibers is derived using an equivalent step-index approach. The derivation assumes a) a weak perturbation of the propagating field, b) a plane cladding coating boundary and c) the neglect of the reinjection of light at the coating air interfaces. With this assumption the scalar wave equation for a straight fiber is solved and the curvature of the fiber is taken into account by an introduction of a correction factor of the refractive indices of the fiber. The bending loss α_B is then:

$$\alpha_B = \frac{2\kappa^2}{\beta V^2 K_1^2 (a\gamma)} \int\limits_0^\infty \frac{\exp\left[-a\left(\gamma^2 + \zeta^2\right)^{1/2}\right]}{\left(\gamma^2 + \zeta^2\right)^{1/2}} \frac{Ai\left[X_2\left(0,\zeta\right)\right]}{Bi\left[X_2\left(a,\zeta\right)\right]} \cdot$$

$$\frac{\chi_2^{1/2} \chi_3^{1/2}}{\left[\chi_2 \cos^2\left(\theta(\zeta)\right) + \chi_3 \sin^2\left(\theta(\zeta)\right)\right]} d\zeta, \qquad (4.5)$$

where K_1 denotes the modified Bessel function and a is the core radius of the fiber. Ai and Bi represent the Airy-functions, two linearly independent solutions of a differential equation commonly appearing in physics, especially in optics, quantum mechanics and electromagnetics. The other coefficients are defined as follows:

$$\kappa = k\sqrt{n_1^2 - n_{eff}^2},$$

$$\gamma = k\sqrt{n_{eff}^2 - n_2^2},$$

$$\beta = kn_{eff} \quad \text{(propagation constant)},$$

$$V = ak\sqrt{n_1^2 - n_2^2} \quad \text{(normalized frequency)},$$

$$X_q(x,\zeta) = \left(\frac{\mathcal{R}_F}{2k^2 n_q^2}\right)^{2/3} \left[\beta^2 + \zeta^2 - k^2 n_q^2 \left(1 + \frac{2x}{\mathcal{R}_F}\right)\right],$$

$$\chi_q = \left(\frac{2k^2 n_q^2}{\mathcal{R}_F}\right)^{2/3} \left[-X_q(b,\xi)\right] \quad (q = 2,3),$$

$$\theta(\zeta) = \frac{2}{3}\left[-X_2(b,\zeta)\right]^{3/2} + \frac{\pi}{4},$$

where $k = 2\pi/\lambda$ represent the wave vector, $\mathcal{R}_F$ is the bending radius of the fiber, x gives the local coordinate, b denotes the radius of the cladding, n_{eff} the effective refractive index of the fiber and n_1, n_2 and n_3 denote the refractive indices of the core, cladding and coating, respectively. ζ is the integral variable.

In order to consider the geometric situation of the bent fiber, all fiber indices are corrected by the factor $(1 + x/\mathcal{R}_F)$, where $x/\mathcal{R}_F \ll 1$. In addition, fiber bending implies an elastic deformation and as a result, the elasto-optic effect changes the refractive fiber index profile [Nag78]. By introducing an effective bending radius $\mathcal{R}_{eff}$ in place of $\mathcal{R}_F$, we take the elasto-optic effect into account in the consideration of bending losses, too. Figure 4.3 depicts a schematic drawing of a bent fiber.
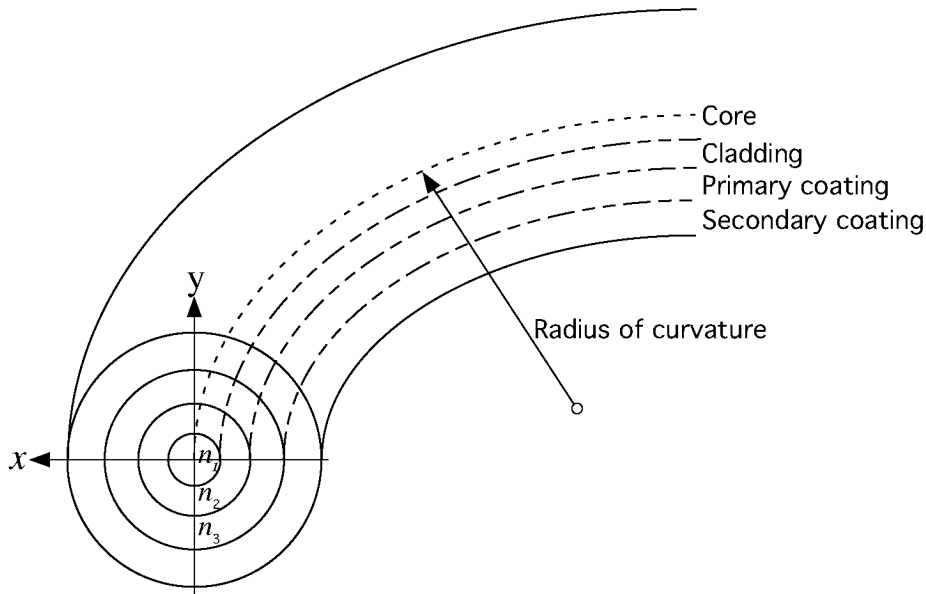

Figure 4.3: Schematic single mode fiber

According to [Sch89], the effective bend radius can be derived from the Hooke's law:

$$\sigma(x) = \frac{x}{\mathcal{R}_o}\mathcal{E}, \qquad (4.6)$$

where $\sigma(x)$ denotes the tensile strength, $\mathcal{R}_o$ is the geometric curvature radius of the fiber and $\mathcal{E}$ is the Young's modulus. The refractive index is related to stress influence via the elasto-optic coefficient ϕ. We consider only the stress induced change of the refractive indices normal to the fiber axis and write for the resulting refractive indices n_{res_i} ($i = 1, 2, 3$) [Sch89]:

$$n_{res_i}(x) = n_i + \underbrace{n_i\frac{x}{\mathcal{R}_o}}_{geometric} + \underbrace{\phi\frac{x}{\mathcal{R}_o}\mathcal{E}}_{elasto-optic\ correction} \qquad (i = 1, 2, 3), \qquad (4.7)$$

The resulting refractive indices of the bent fiber can also be expressed in terms of the new effective bend radius of the fiber $\mathcal{R}_{eff}$ taking into account the elasto-optic effect:

$$n_{res_i}(x) = n_i + n_i\frac{x}{\mathcal{R}_{eff}} = n_i\left(1 + \frac{x}{\mathcal{R}_{eff}}\right) \quad (i = 1, 2, 3). \qquad (4.8)$$

The comparison of Eq. (4.7) and Eq. (4.8) gives us an expression of the effective curvature fiber radius $\mathcal{R}_{eff}$ considering the stress induced refractive index change:

$$\frac{1}{\mathcal{R}_{eff}} = \frac{n_i + \phi\mathcal{E}}{n_i\mathcal{R}_o} \quad (i = 1, 2, 3). \qquad (4.9)$$

By inserting the following values for silica: $\phi = $ -4.2·10^{-12} m²/N [Pri59], $\mathcal{E} = 7.6 \cdot 10^{10}$ N/m² [Pri59] and a refractive index value of $n = 1.47$, the effective radius amounts to $\mathcal{R}_{eff} = 1.22 \cdot \mathcal{R}_o$. Hence, the elastic deformation of the refractive index profiles can be expressed by an effective bend radius which describes a bent fiber without stress. Since $\mathcal{R}_{eff} > \mathcal{R}_o$, the stress-induced refractive index change in a bent fiber reduces bending losses in a silica-based fiber.
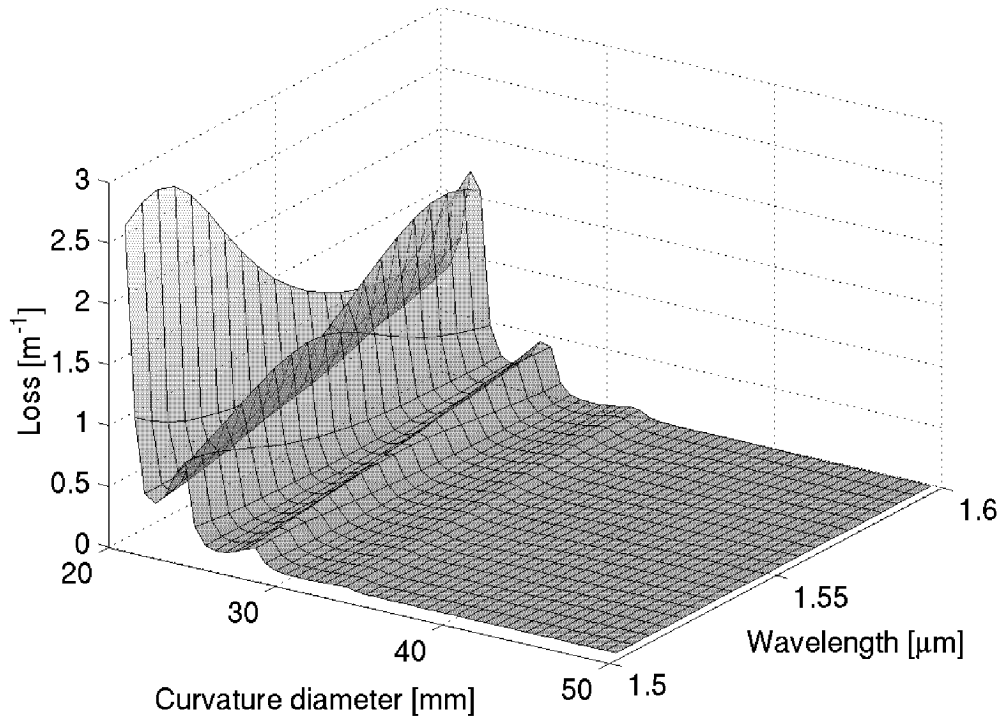
Figure 4.4: Calculated bending losses

Calculated bending losses in a silica-based single-mode fiber at different wavelengths and curvature diameters $2 \cdot \mathcal{R}_{eff}$. The values of the parameters used in the calculation can be found in Tab. II.

Figure 4.4 shows calculated bending losses with respect to different curvature diameters of the fiber in the near-infrared range. The pronounced

modulation behavior mentioned above is clearly visible. The values of the parameters used in the calculation correspond to our experimental situation. The data can be found below in Tab. II.

The losses have been calculated for the case in which the refractive index of the acrylate coating is higher than the index of the silica-based cladding. By removing the acrylate layer, a variation of the refractive index of the medium surrounding the cladding would also be possible (e.g. fiber in a solution with different sucrose concentrations).

4.3.2 Experimental setup

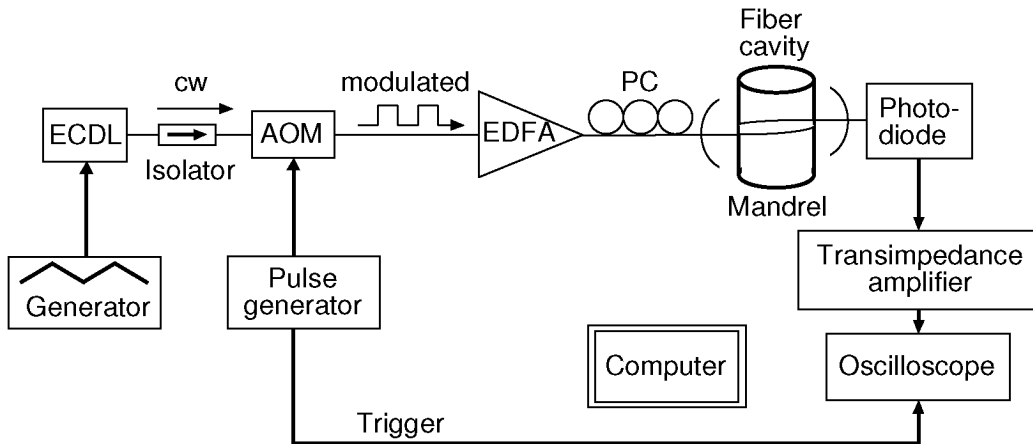A schematic diagram of the fiber cavity ringdown setup for bending loss measurements is depicted in Fig. 1.

Figure 4.5: Schematic setup for bending loss measurements
ECDL: external cavity diode laser, AOM: acousto-optical modulator, EDFA: erbium-doped fiber amplifier, PC: polarization controller

An external cavity diode laser (ECDL; Newport, EOSI 2010) was used as a cw-light source featuring a fiber-coupled output power of 1.3 mW at

1550 nm. Afterwards, the cw-beam was chopped by an acousto-optical modulator (AOM; Intra Action, FCM-401E5C) at a frequency of 10 kHz and amplified by an erbium-doped fiber amplifier (EDFA). After a polarization controller (PC; Thorlabs, FPC031), the modulated light was coupled into a fiber cavity formed by two FC/PC fiber connectors coated with highly reflective dielectric mirrors ($R_{1,2} = 99.5$ %) (Evaporated Coatings, Inc. USA). Index matching gel between the metallized and the ordinary FC/PC connectors as well as an additional fine tuning of the wavelength within 1 GHz by a triangle bias generator ensured an efficient coupling of the laser modes into the cavity. Cavities of three different lengths, i.e. 10 m, 1 m and 20 cm, respectively, were available. The fiber cavity and the fiber patch cables used in the setup are standard single-mode silica-based fibers ($\alpha_o \leq 0.3$ dB/km at 1550 nm [Cor1]) meeting the ITU 652 recommendation. An InGaAs photodiode (Thorlabs, D400 FC) detected the intensity leaking from the cavity. The electronic signal of the photodiode was amplified (Femto, HCA-40M-100K-C), acquired by an oscilloscope (Tektronix, TDS 620) and analyzed with a computer. The analysis of the exponential ringdown signal is based on a non-linear Newton fitting algorithm and can be found in [Ler02₂].

4.3.3   Results and discussion

First, the ringdown time τ of the 10 m-long straight silica-based single-mode fiber cavity was measured whereby the average ringdown times of 100 ringdown events were recorded 20 times allowing the evaluation of the mean value (MEAN) of the ringdown time and the standard error of the mean (SEM). The measured ringdown time of the straight 10 m-long single-mode cavity amounted to 7.2 ± 0.11 μs (MEAN ± SEM). According to Eq. (4.4) with t = 2.7 (99 % confidence level), this corresponds to a minimum detectable absorbance of $1.72 \cdot 10^{-3}$ dB per cavity pass. Compared to a bend-insensitive fiber exhibiting a bending loss of only $5 \cdot 10^{-2}$ dB [Sto], this limit is one order of magnitude better allowing an accurate determination of the bending loss even in this special fiber. Then, bending losses were introduced by coiling the fiber

cavity exactly once around a mandrel with a specified radius which is identical to the geometric curvature radius of the fiber $\mathcal{R}_o$, i.e. the circumference of the mandrel corresponds to the length where the loss takes place: $l = 2\pi \cdot \mathcal{R}_o$ (see Eq. (4.2)). When the radius of curvature was decreased from $\mathcal{R}_o = \infty$ (straight fiber) to $\mathcal{R}_o = 11.5$ mm, the ringdown time of the 10 m-long fiber cavity decreased to 2.2 ± 0.07 μs. Figure 4.6 depicts the measured ringdown times in the 10 m-long fiber cavity at different curvature radii $\mathcal{R}_o$ at 1550 nm. The modulation of the bending loss in dependence of the fiber curvature radius as predicted in Fig. 4.4 is already indicated by the modulation of the ringdown times.
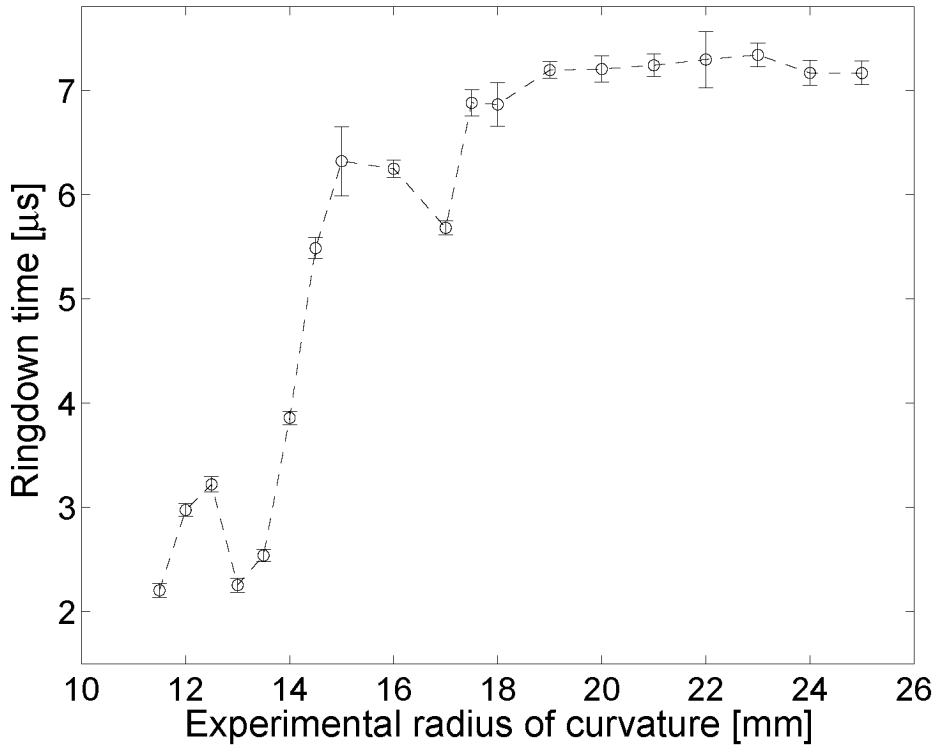

Figure 4.6: Ringdown times of a 10 m-long bent fiber

Ringdown times of a 10 m-long fiber cavity coiled on mandrels with different experimental curvature radii at a wavelength of 1550 nm

From the measured ringdown times corresponding to the straight and the

bent cavities, the experimental bending loss $\mathcal{A}_B$ [dB/m] = 4.343·α_B ([Agr92] and Eq. (4.3)) is obtained as a function of the mandrel radius, i.e. of the fiber curvature radius $\mathcal{R}_o$. Figure 4.7 shows the calculated bending losses versus the curvature radius of the bent single-mode fiber. The ringdown time decreases from $\mathcal{R}_o = \infty$ (straight fiber) to $\mathcal{R}_o = 11.5$ mm corresponds to an additional loss of 0.93 ± 0.1 dB/m. The detection of higher losses in the 10 m-long cavity is restricted by the total loss occurring in a single roundtrip within the fiber, i.e. by the term $\alpha_o L + \alpha_B l$ in Eq. (4.2). A high loss in a cavity causes an intensity leaking from the cavity that is too low to ensure an accurate detection of the ringdown events. The obtained bending losses with a curvature radius larger than 11.5 mm exhibit two local maxima around 13 mm and 17 mm as observed in Fig. 4.7 with an additional loss of 0.79 ± 0.08 dB/m and 0.074 ± 0.041 dB/m, respectively.

The derived losses are compared with the theoretical data calculated by the curvature loss formula given in [Fau97]. Thereby, the calculated data are plotted versus the experimental curvature radius $\mathcal{R}_o = \mathcal{R}_{eff}/1.2$. The comparison is depicted in Fig. 4.7. Table II lists the parameters used in the calculation in order to fit the measured bending losses, and the parameters found in literature.

With the exception of the refractive index difference between the fiber core and the cladding, which is not specified as a function of wavelength by the manufacturer, the parameters used for the calculation agree very well with literature data. Therefore, the measurement of bending losses and the comparison with the theoretical model give the opportunity to experimentally extract fiber parameters.

The bending loss measurements were repeated with silica-based single-mode fiber cavities of shorter lengths, namely 1 m and 0.2 m, to prove the reliability of the FCRD technique. In addition to the bending losses of the 10 m-long fiber cavity, these data and the modeled losses are depicted in
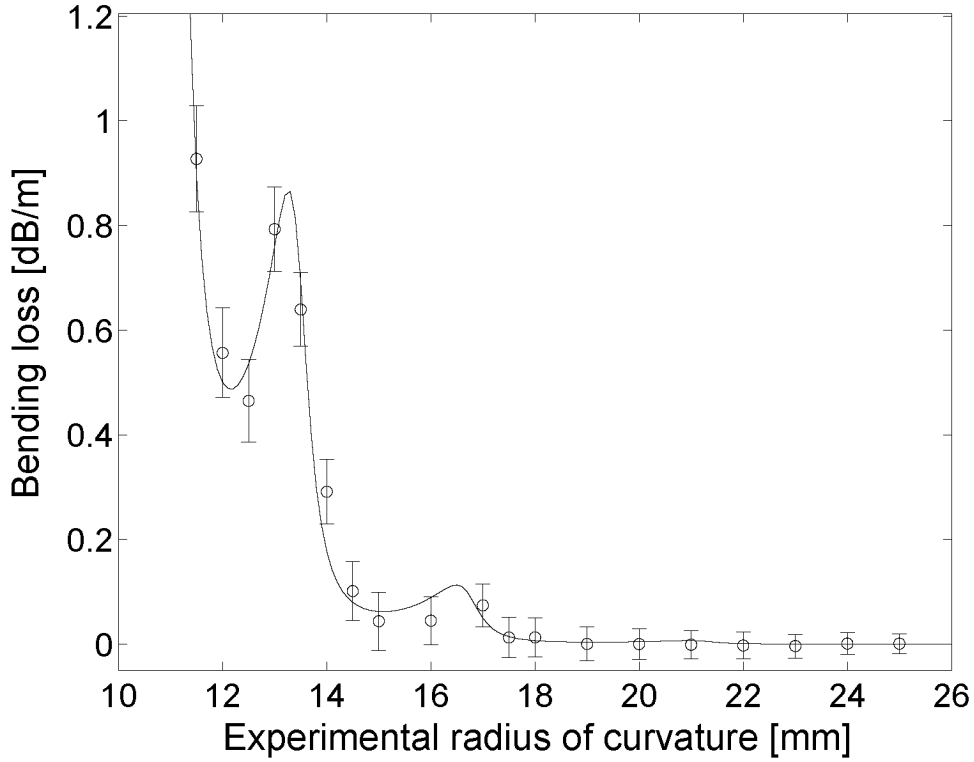
Figure 4.7: Bending loss of a 10 m-long fiber

Bending loss of a 10 m-long fiber cavity coiled on mandrels with different experimental curvature radii at a wavelength of 1550 nm. Measured bending loss (○), modeled bending loss with parameters given in Tab. II (—)

Fig. 4.8. The same parameters as listed in Tab II are used for the calculation. Good agreement is obtained between experimental and theoretical data in particular the modulation behavior is well documented.

Bending losses of these cavities show all the same oscillating behavior, i.e. two local maxima at curvature radii of approximately 13 mm and 17 mm. Consequently, FCRD does not depend on the length of the fiber cavity but shorter cavities are characterized by shorter ringdown times. The straight 1 m-long cavity features a ringdown time of 1.89 ± 0.16 μs that decreases to 0.2 μs when the bending loss increases up to 1.31 ± 0.097 dB/m for a cur-

Table II: Fiber parameter comparison

Comparison between the fiber parameters found in literature and the parameters used in the calculation of bending losses

Values	found in literature	used in model
Core radius [μm]	4.1 [Cor1]	4.1
Cladding radius [μm]	62.5 $\pm$ 0.5 [Cor1]	63
Effective group index of refraction	1.4682 @ 1550 nm [Cor1]	1.4682
Refractive index difference between fiber core and cladding	0.0036 [Cor1]	0.0025
Refractive index of primary coating	1.49 [Cor2, Sar]	1.49
Elasto-optical correction factor	1.22 (sec. 4.3.1) 1.28 @ 546 μm [Pri59, Sch89]	1.2

vature radius of 11.5 mm. The detection limit for loss measurements of the 1 m-long fiber cavity amounts to $3.63 \cdot 10^{-3}$ dB. The ringdown time of the straight 0.2 m-long fiber cavity is 0.96 ± 0.19 μs resulting in a minimum detectable additional absorbance of $3.35 \cdot 10^{-3}$ dB per pass through the cavity. This decay time decreases to 0.19 μs with decreasing curvature radius down to 14 mm. The detection limits in the 1 m-long and 20 cm-long fiber cavities are about twice of the detection limit in the 10 m-long fiber cavity which is due to the increased ratio of the ringdown time standard deviation to the ringdown time, i.e. $\Delta\tau/\tau$ in Eq. (4.4). Not only is the detection of low losses
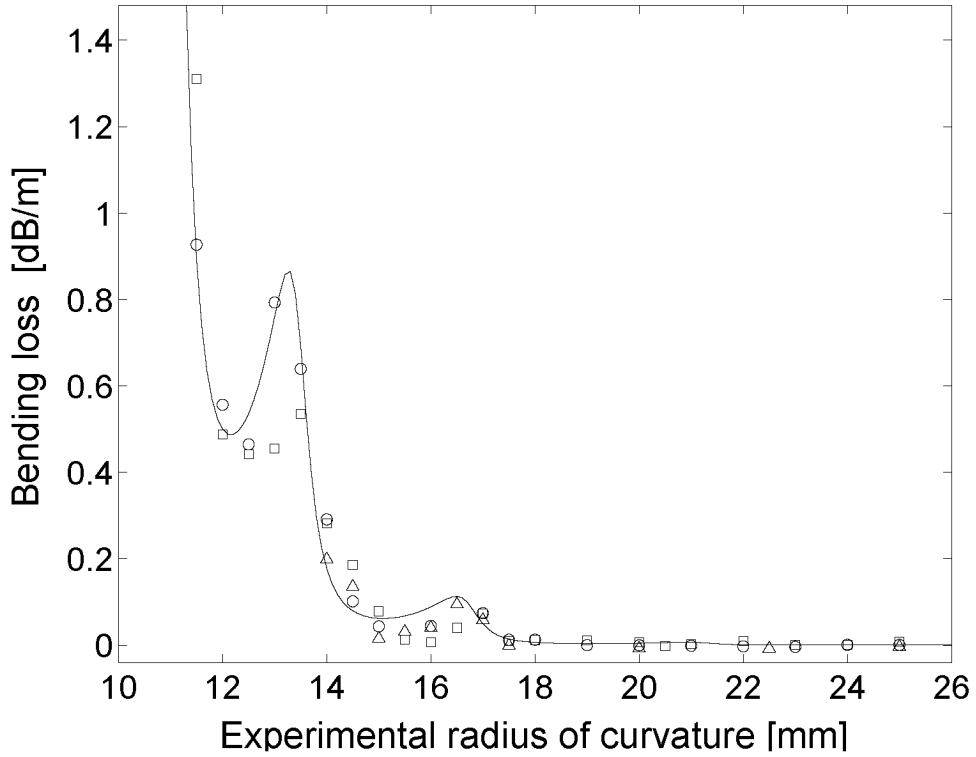
Figure 4.8: Bending losses of different cavities

Bending losses at different experimental curvature radii of cavities with different lengths at a wavelength of 1550 nm. Measured bending loss of a 10 m-long cavity (○), a 1 m-long cavity (□), a 0.2 m-long cavity (△), modeled bending loss with parameters given in Tab. II (—)

in short fiber cavities limited but also the detection of high losses is restricted by a too fast decaying ringdown signal. No measured ringdown time can be shorter than the fall time (150 ns) of the employed acousto-optical modulator. By comparing the fall time of the modulator with the ringdown time of the straight cavity, we find that the minimum required length of the fiber cavity is 15.3 cm in our case.

4.3.4   Conclusion

A sensitive and reliable method for the determination of any kind of optical attenuation in fiber cavities was presented. Bending losses in cavities with different lengths were measured and we found very good agreement between the experimentally derived fiber parameters and literature data. A minimum detectable absorbance of $1.72 \cdot 10^{-3}$ dB per pass through a 10 m-long fiber cavity was achieved. This limit is even low enough for an accurate determination of bending losses in bend-insensitive fibers. The sensitivity for loss measurements using the FCRD technique is reduced by shortening the cavity length but FCRD is not suited for too high loss determination since a high loss results in a too low intensity leaking from the cavity or in a too fast decay of the ringdown signal. Compared to the well-established cut-back method [Mar81], the FCRD technique only requires a short fiber cable for a sensitive loss measurement and does not affect the fiber. Other advantages of this method are the insensitivity to intensity fluctuations of the light source used for the measurement and the potential for remote fiber sensing.

4.4   Fiber-optic cavity sensing of hydrogen diffusion

The low transmission loss (≤ 0.3 dB/km @ 1550 nm [Cor1]) is one of the superior features of optical silica-based fibers. However, in 1982 first field-installed optical fibers showed an unexplainable loss increase in comparison to their loss at the time of installation two years previously [Tan84]. It was found that hydrogen gas produced by chemical reactions of constituents of the cable material such as corrosion of metallic materials and chemical decomposition of the fiber coating materials diffused into the fiber and caused the loss [Mit84]. The additional optical attenuation arose from the molecular hydrogen in the fiber as well as the hydroxyl (OH) bonds formed by chemical reaction between dissolved hydrogen (H_2) and the fiber glass [Ohm83]. The dissolved hydrogen in silica generates several loss peaks in the near infrared range. The peaks due

to the excitations of H_2-vibration are nearly independent of fiber glass material dopants [Sto82$_2$, Nog83] and are reversible, i.e. they disappear again if the hydrogen molecules diffuse out of the fiber glass [Nog85, Mur83]. Contrary, loss peaks at 1.39 μm (Si-OH bonds) and 1.41 μm (Ge-OH bonds) are caused by chemical reactions between the dissolved hydrogen and silica [Ito85]. They are therefore irreversible and depend on the fiber dopant [Nog85].

The phenomenon of the optical loss increase due to hydrogen was extensively studied in the past [Uch86, Kuw88, Iln90, Lem91, Hum96] and today, the discovered knowledge is very useful in the development of fiber-based hydrogen sensors whose demand is founded on the increasing importance of hydrogen as a clean energy source. But hydrogen is also utilized in hydrogenation processes, petroleum transformation, soldering, cryogenic cooling, rocket engines, etc. [Oka03].

This section discusses measurements of hydrogen diffusion out of a silica-based single-mode fiber with the fiber cavity ringdown scheme. To the best of our knowledge, this is the first demonstration of spectroscopic absorption measurements in a fiber-optic cavity.

4.4.1 H_2-diffusion in silica-based single-mode fibers

The mathematical theory of the diffusion in isotropic substances is based on the hypothesis that the transfer rate of a diffusing substance through a unit area of a section is proportional to the concentration gradient measured normal to the section. According to [Cra75], the diffusion rate s per unit area is:

$$s = -D \, \frac{\partial C\left(\vec{x}, t\right)}{\partial \vec{x}}, \tag{4.10}$$

where C denotes the concentration of the diffusing substance, $\vec{x}$ is the space

vector measured normal to the section and D is the diffusion coefficient of the adequate material. The negative sign in Eq. (4.10) arises because of the opposite direction of the diffusion process to the increasing concentration. The concentration satisfies the well known diffusion equation enclosing the Laplace operator Δ:

$$\frac{\partial C\left(\vec{x}, t\right)}{\partial t} = D \Delta C\left(\vec{x}, t\right). \tag{4.11}$$

Since the fibers show a mandrel form (see Fig. 4.13 below), it is advisable to rewrite the diffusion equation in cylindrical coordinates r, θ and z:

$$\frac{\partial C}{\partial t} = \frac{1}{r}\left[\frac{\partial}{\partial r}\left(rD\frac{\partial C}{\partial r}\right) + \frac{\partial}{\partial \theta}\left(\frac{D}{r}\frac{\partial C}{\partial \theta}\right) + \frac{\partial}{\partial z}\left(rD\frac{\partial C}{\partial z}\right)\right]. \tag{4.12}$$

Assuming that the substance diffuses homogeneously and radially in or out of the fiber, i.e., the concentration is a function of radius r and time t only, we simplify Eq. (4.12) to:

$$\frac{\partial C\left(r, t\right)}{\partial t} = \frac{1}{r}\frac{\partial}{\partial r}\left(rD\frac{\partial C}{\partial r}\right). \tag{4.13}$$

This differential equation is solved with the initial condition for a fiber exposed to a hydrogen atmosphere. At time $t = 0$ s, there are no hydrogen molecules inside the silica-based fiber. In contrast, the surface of the cladding is saturated with dissolved molecules starting their diffusion into the fiber. Hence, we write with C_s as the saturated concentration of hydrogen molecules

in silica and with b as the radius of the silica-based fiber, i.e. the outer radius of the fiber cladding (see Fig. 4.13), the initial condition as follows:

$$C(r,t) = C_s \quad for \quad r = b \quad and \quad t \geq 0; \tag{4.14}$$

$$C(r,t) = 0 \quad for \quad r < b \quad and \quad t = 0. \tag{4.15}$$

The solution of the differential Eq. (4.13) with the initial condition described by Eqs. (4.14), (4.15) for a fiber exposed to hydrogen molecules is [Cra75]:

$$C(r,t) = C_s - C_s f\left(\frac{r}{b}, \frac{Dt}{b^2}\right) \tag{4.16}$$

with

$$f(x,y) = 2 \sum_{n=1}^{\infty} \frac{J_o(j_n x) \, exp\left(-j_n^2 y\right)}{j_n J_1(j_n)}, \tag{4.17}$$

where j_n is the nth zero of the Bessel function $J_o(j_n) = 0$ ($j_1 = 2.4048$, $j_2 = 5.5201$, $j_3 = 8.6537$, $j_4 = 11.7915$ ... [Bro95]).

The evolution of the normalized concentration $C(r,t)/C_s$ of the dissolved H_2-molecules inside the fiber is therefore:

$$\frac{C(r,t)}{C_s} = 1 - 2 \sum_{n=1}^{\infty} \frac{J_o\left(j_n \frac{r}{b}\right) exp\left(-j_n^2 \frac{Dt}{b^2}\right)}{j_n J_1(j_n)} \tag{4.18}$$

and can be calculated if the hydrogen diffusion coefficient in silica $D_{H_2-silica}$ is known. $D_{H_2-silica}$ is a function of temperature and can be calculated by [Lem91]:

$$D_{H_2-silica} = 2.83 \cdot 10^{-4} \, exp \left(\frac{-40.19 \, \text{kJ/mol}}{\text{RT}} \right) \text{cm}^2/\text{s}, \qquad (4.19)$$

where R is the gas constant and T denotes the absolute temperature. Figure 4.9(a) depicts $D_{H_2-silica}$ at different temperatures whereby the calculated value for $D_{H_2-silica}$ at 303 K amounts to $D_{H_2-silica}$ (T = 303 K) = $3.336 \cdot 10^{-11}$ cm^2/s.

For the evaluation of the absolute hydrogen concentration $C(r,t)$ in the fiber, the solubility or the saturated concentration C_s of hydrogen in silica has to be known. This value is expressed by [Sha72]:

$$C_s = \left(\frac{h^2}{2\pi m k_B \text{T}} \right)^{\frac{3}{2}} \frac{p N_s}{k_B \text{T}} \left[\frac{exp \left(\frac{-h\nu}{2k_B \text{T}} \right)}{1 - exp \left(-h\nu/k_B \text{T} \right)} \right]^3 exp \left(\frac{-V_o}{\text{RT}} \right), \qquad (4.20)$$

where C_s [cm^{-3}] is the number of hydrogen molecules dissolved per unit volume of glass, h is the Planck's and k_B the Boltzmann's constant, m is the mass of one hydrogen molecule, p is the hydrogen partial pressure, N_s is the number of solubility sites available per unit volume ($N_s = 2.22 \cdot 10^{22}$ cm^{-3}), V_o denotes the binding energy per mol ($V_o = $ -3.04 kcal/mol) and ν is the vibration frequency of the dissolved hydrogen molecules ($\nu = 1.22 \cdot 10^{13}$ Hz) [Sha72]. The solubility of hydrogen at elevated room temperature T = 303 K is set to be equal to the saturated hydrogen concentration in silica: C_s(T = 303 K) = $2.59 \cdot 10^{18}$ molecules/cm^3. As we can see in Fig. 4.9(b), the solubility decreases

with increasing temperature.

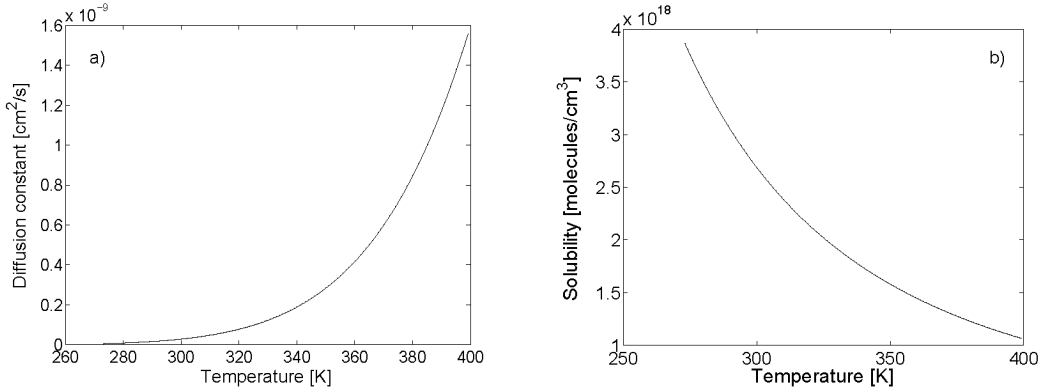**Figure 4.9: Diffusion and solubility coefficient of H$_2$ in SiO$_2$**
a) Diffusion coefficient of H$_2$ in silica at different temperatures
b) H$_2$-solubility in silica at different temperatures

The knowledge of the saturated concentration of the dissolved hydrogen molecules and of the hydrogen diffusion coefficient in silica at 303 K allows the calculation of the temporal evolution of the absolute hydrogen concentration inside a silica-based single-mode fiber exposed to hydrogen. Figure 4.10(a) depicts the concentration evolution vs. time inside the fiber core ($r = 2.5$ μm $< r_c$, $b = 62.5$ μm). Generally, the radius of a silica-based single-mode fiber core r_c is about 4.1 μm but the radius of the mode field is slightly larger than the core radius, i.e. a part of the mode propagates in the cladding of the fiber. Therefore, the mode field radius is about 5 μm [Cor1]. Figure 4.10(b) depicts the normalized concentration difference between the mode field edge and the central axis (see discussion below).

If we consider alternatively the case of a hydrogen saturated fiber kept at ambient air so that the hydrogen molecules can diffuse out of the fiber, and solve the differential Eq. (4.13) with the following initial condition:
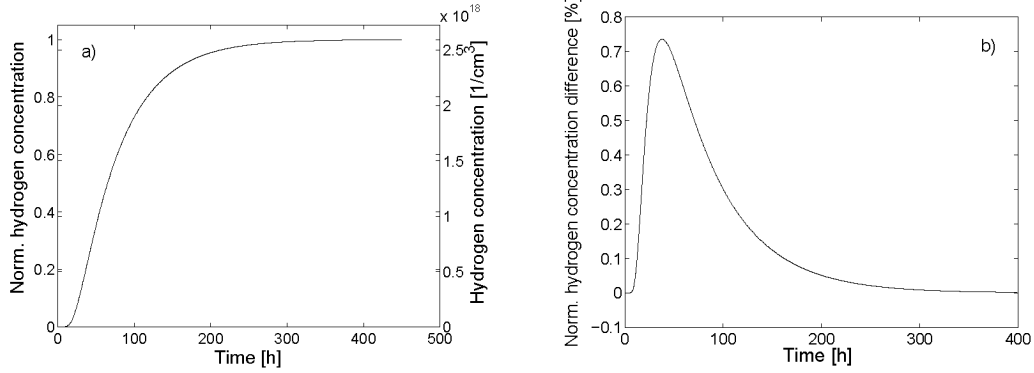
Figure 4.10: H$_2$ concentration in a silica-based single-mode fiber

a) Normalized and absolute H$_2$ concentration in the fiber core (r=2.5μm)
b) Normalized concentration difference $[C(r$=5μm,t)-$C(r$=0μm,$t]/C_{\rm s}$
vs. diffusion time

$$C = 0 \quad for \quad r = b \quad and \quad t \geq 0; \qquad (4.21)$$

$$C = C_s \quad for \quad r < b \quad and \quad t = 0, \qquad (4.22)$$

we get the solution [Cra75]:

$$C(r,t) = C_s f\left(\frac{r}{b}, \frac{Dt}{b^2}\right) = 2C_s \sum_{n=1}^{\infty} \frac{J_o\left(j_n\frac{r}{b}\right) exp\left(-j_n^2\frac{Dt}{b^2}\right)}{j_n J_1\left(j_n\right)}. \qquad (4.23)$$

The relative concentration $C(r,t)/C_s$ only is considered in the following treatment and the diffusion of the hydrogen molecules through the protective acrylate jacket surrounding the fiber cladding is neglected. The neglect is based on the fast diffusion process of hydrogen through the acrylate layer whose outer (inner) diameter is usually 250 μm (125 μm) [Cor1]. In order

to estimate the unknown diffusion constant $D_{H_2-acrylate}$ of hydrogen in acrylate polymer surrounding the silica-based fiber, we take the known diffusion coefficient $D_{H_2O-acrylate} = 5.8 \cdot 10^{-13}$ m^2/s of water in acrylate [Mro01]. This value is about two orders of magnitude higher than the diffusion coefficient $D_{H_2-silica}$ of H$_2$ in silica [Lem91, She77]. It is found experimentally that the diffusion coefficient D depends on the size of the diffusing gas molecule and that D decreases with increasing molecule diameter. Therefore, $D_{H_2O-acrylate}$ is smaller than the hydrogen diffusion $D_{H_2-acrylate}$ in acrylate and consequently, the diffusion of hydrogen through the acrylate polymer is at least two orders of magnitude faster than the diffusion process of hydrogen through silica. We can thus reasonably neglect the acrylate polymer jacket surrounding the silica fiber and concentrate on the modeling of the slow H$_2$ diffusion process in silica.

Since the light absorption beyond a wavelength of about 1.5 μm is only caused by the vibration excitation of diffused H$_2$ molecules in silica [Lem91], the normalized concentration $C(r,t)/C_s$ is assumed to be proportional to the additional loss $\alpha(t)$. This linear approach is justified since Eq. (4.18) implies that the relative concentration difference $[C(r = 5\ \mu\text{m},t) - C(r = 0\ \mu\text{m},t)]/C_s$ within the optical mode-field (radius of 5.2 μm [Cor1]) is smaller than 1 % during the H$_2$ diffusion process (see Fig. 4.10(b)). Hence, the hydrogen concentration inside the single-mode fiber core can be assumed to be homogeneous over the whole mode field. Consequently, we write:

$$\frac{C(r=0,t)}{C_s} = \frac{\alpha(t)}{\alpha_s} = 2 \sum_{n=1}^{\infty} \frac{exp\left(-j_n^2 \frac{Dt}{b^2}\right)}{j_n J_1\left(j_n\right)}, \tag{4.24}$$

where α_s stands for the additional hydrogen-induced loss in a H$_2$-saturated fiber. The calculation of the additional loss $\alpha(t)$ can be completed if the diffusion coefficient $D_{H_2-silica}$ of hydrogen in silica and α_s are known. Therefore, we revert to the temperature-dependent diffusion coefficient $D_{H_2-silica} = 3.336 \cdot 10^{-15}$ m^2/s at 30° C [Lem91] and determine experimentally α_s.

In the following, we focus our attention to a fiber cavity ringdown experiment in which the ringdown times, and thus the losses during a hydrogen out-diffusion process in a fiber cavity are measured. The results are discussed with respect to this theoretical treatment.

4.4.2   Experimental setup

In order to get a hydrogen-saturated fiber, a 10 m-long silica-based single-mode fiber cavity was coiled on a mandrel whose diameter (77 mm) was large enough to avoid bending losses as demonstrated in the previous section 4.3 and in [Ler02₁]. The mandrel was placed in a hermetically sealed container and the container was filled with gaseous hydrogen. Figure 4.11 shows a schematic picture of the container enclosing a pressure sensor, valves and the fiber output part sealed with hard cured resin.
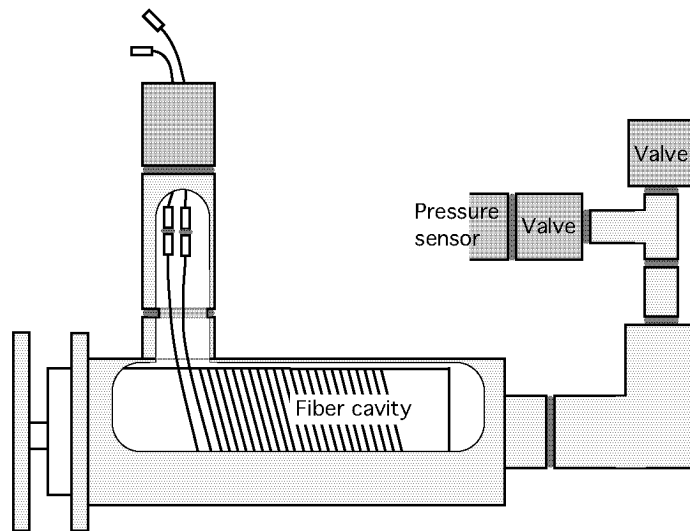

Figure 4.11: Container for H$_2$-saturation

Container for the H$_2$-saturation of a fiber cavity coiled on an inner mandrel

In this container, the fiber cavity was exposed to pure hydrogen for two weeks at room temperature and at a total pressure of 1 bar. This time period is long enough to ensure a hydrogen saturation of the fiber cavity. An estimation of the saturation time of hydrogen in silica follows later in this section. After these two weeks, the ringdown times of the cavity were recorded with the fiber cavity measurement setup depicted in Fig. 4.12.
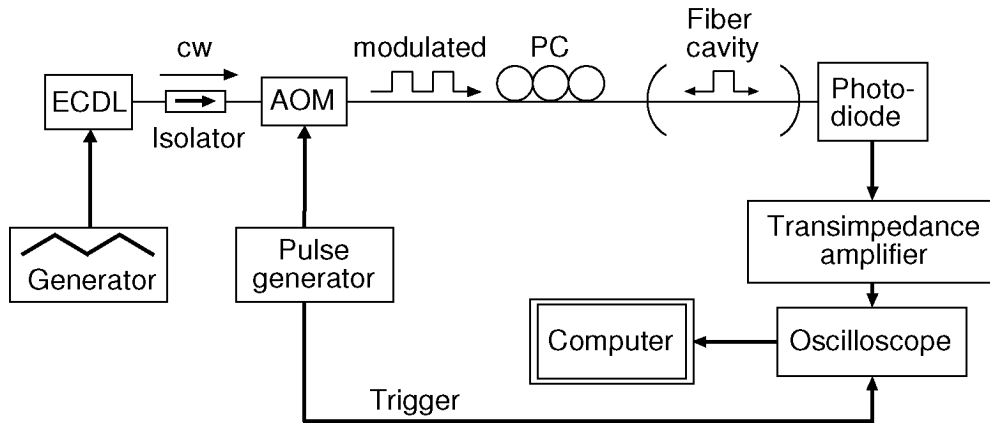

Figure 4.12: Schematic diagram of the H_2 measurement setup
ECDL: external cavity diode laser, cw: continuous-wave, AOM: acousto-optic modulator, PC: polarisation controller

An external cavity diode laser (ECDL; Santec TSL-210) was used as a tunable laser source (1520 nm - 1600 nm). A triangle bias generator applied to the laser fine tuned the wavelength to ensure an efficient coupling of the laser modes into the cavity. The emitted cw-laser beam (5 mW output power) was also modulated by an acousto-optic modulator (AOM; Intra Action, FCM-401E5C) with a frequency of 10 kHz. This frequency prevents an overlapping of consecutive ringdown events with typically observed ringdown times of ~ 10 μs. After the AOM, the modulated signal propagated through a polarization controller (PC; Thorlabs FPC031) and was then coupled into the 10 m-long fiber cavity. In order to form the cavity in the fiber, fiber connectors (FC/PC) of a ten meter fiber patch cable were coated with highly reflective dielectric mirrors (Evaporated Coatings, Inc. USA). The fiber itself was a

standard silica-based single-mode fiber meeting the ITU 652 recommendation [Cor1] and its core was doped with germanium atoms to get the light-guiding difference of refractive indices between the fiber core and the cladding. The radii of core and cladding were 4.1 μm and 62.5 μm, respectively. A schematic structure of a single-mode fiber is depicted in Fig. 4.13.
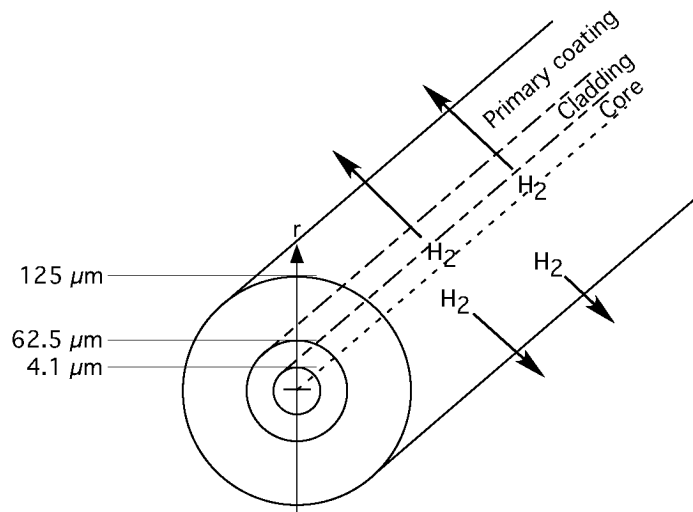

Figure 4.13: Schematic out-diffusion process in a single-mode fiber

Schematic cross-section of a single-mode fiber with out-diffusing hydrogen molecules: core (Ge-doped silica), cladding (silica), primary coating (acrylate)

An InGaAs photodiode (Thorlabs D400 FC) detected the light intensity leaking out of the cavity. The electrical signal of the photodiode was amplified (Femto, HCA-40M-100K-C) and monitored by a digital oscilloscope (Tektronix TDS 620). A computer collected and analyzed the data. The ringdown time determination from the exponential ringdown events was based on a non-linear Newton fit procedure and can be found elsewhere [Ler02$_2$].

4.4.3 Results and discussion

A first ringdown time spectrum was recorded in the wavelength range between 1520 nm and 1600 nm in steps of 2 nm after the hydrogen saturation of the 10 m-long silica-based single-mode fiber cavity was reached. During the measurement, the fiber cavity was still exposed to hydrogen. Then, the fiber was placed in an oven in a H_2-free atmosphere of ambient air at a temperature of 30° C. After an out-diffusion time of 360 h, the ringdown time spectrum of the fiber was recorded again between 1520 nm and 1600 nm. Thereby, the spectrum was found free of hydrogen contamination, i.e. the ringdown times after the hydrogen out-diffusion of the fiber cavity are equal to the ringdown times before the diffusion process in the cavity. The ringdown time measurements before and after the complete H_2-diffusion out of the silica-based fiber are depicted in Fig. 4.14.

The observed wavelength dependence of the ringdown times in the H_2-free fiber is based on the wavelength-dependent reflectivities of the dielectric mirrors on the fiber end faces. The standard deviation of the measured ringdown times is ~ 2 %. The recorded ringdown times τ after the out-diffusion process allow the extraction of the reflectivity $\tilde{R}$ of the fiber cavity mirror. The mirror reflectivity in the fiber cavity is given as (see Eq. (2.23)):

$$\tilde{R} = 1 - \frac{Ln_{eff}}{c_o\tau} + \alpha_o L, \qquad (4.25)$$

where $\tilde{R} = \sqrt{R_1 R_2}$ denotes a measure of the mirror reflectivities R_i ($i = 1, 2$), L is the length of the cavity, α_o denotes the intrinsic fiber loss coefficient, the effective refractive index of the cavity material is expressed by n_{eff}, and c_o is the speed of light in vacuum. The determination of $\tilde{R}$ underlies the assumption that the intrinsic loss inside the fiber cavity is $\alpha_o = 0.3$ dB/km for the entire spectral range of the ECDL [Cor1]. The reflectivity calculated with the measured ringdown times is depicted in Fig. 4.15.
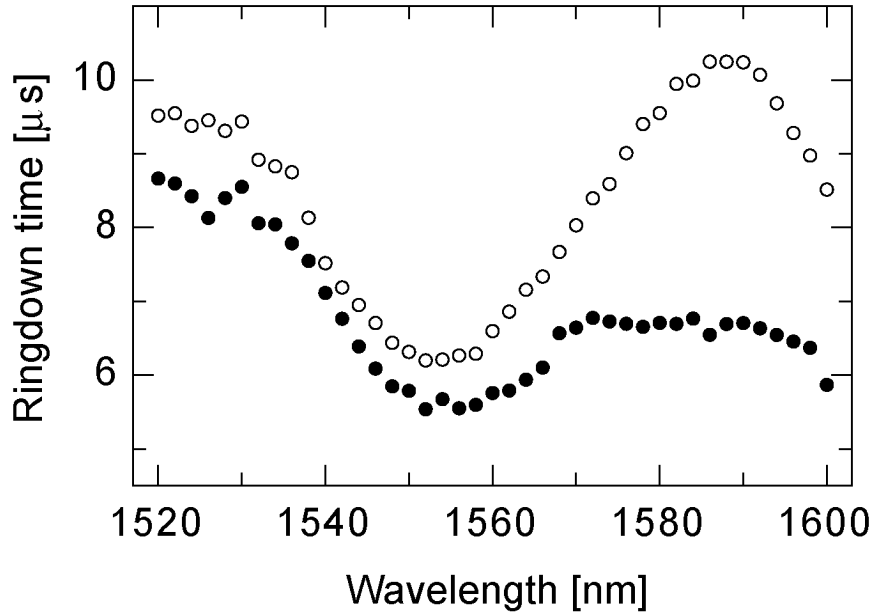
Figure 4.14: Ringdown times before and after H_2 diffusion

Ringdown times in a 10 m-long fiber cavity before (•) and after (○) the H_2 out-diffusion process at different wavelengths. The ringdown times follow the wavelength-dependent reflectivity of the fiber cavity mirrors.

A strong wavelength-dependence of the mirror reflectivity is found so that the reflectivity values range between 99.92 % and 99.96 % for wavelengths between 1520 nm and 1600 nm.

Figure 4.14 implies that the out-diffusion of H_2 is accompanied by a general increase of the ringdown time in the entire wavelength range between 1520 nm and 1600 nm. The increase of the ringdown time is correlated with a decrease of optical losses inside the cavity. Large differences in the ringdown times are observed in the range between 1560 nm and 1600 nm with a maximum at 1586 nm. Let's assume that the reflectivities of the mirrors are not influenced by hydrogen. Hence, the difference in the ringdown times at identical wavelengths before and after the diffusion process allows the calculation of the saturated additional loss α_s inside the cavity caused by hydrogen. According
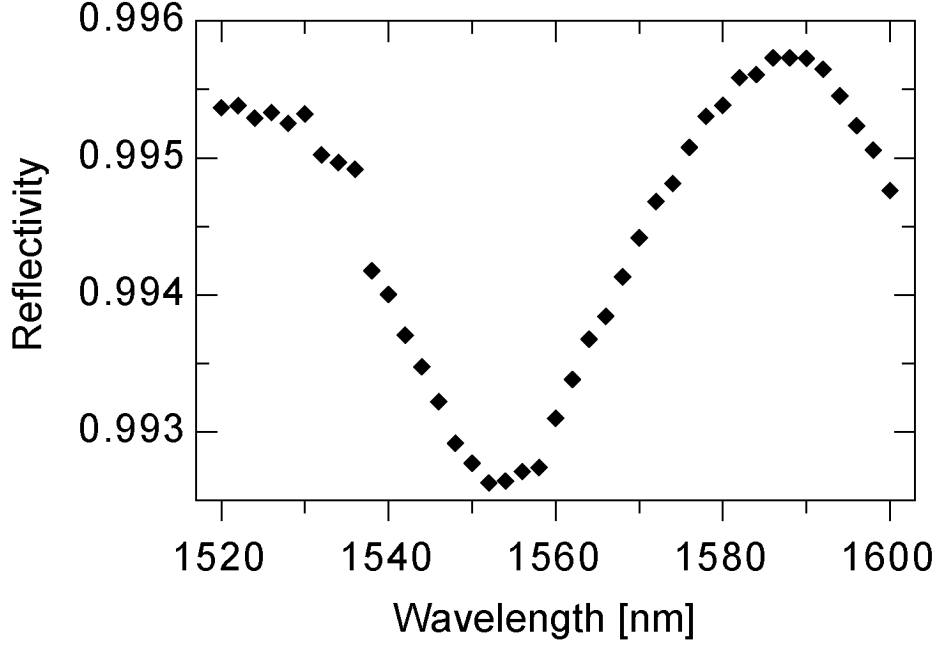
Figure 4.15: Reflectivity of the dielectric fiber mirror

to the theoretical consideration of the fiber cavity ringdown technique (see Eq. (4.3)), we get the following expression for α_s:

$$\alpha_s = \frac{n_{eff}}{c_o}\left(\frac{1}{\tau_{H_2}} - \frac{1}{\tau}\right),\qquad(4.26)$$

where τ denotes the ringdown time of a straight and unaffected fiber cavity and τ_{H_2} is the ringdown time of the hydrogen-saturated fiber cavity. The enhanced loss α_s derived from our data amounts to ~ 0.25 dB/km in the wavelength range between 1520 nm and 1550 nm. For longer wavelengths, the loss increases and reached its maximum at a wavelength of 1586 nm. At this wavelength, hydrogen induces an additional loss of 1.2 dB/km. A slight decrease of the loss can be observed up to 1598 nm and a new increase of the loss at 1600 nm. Hydrogen-enhanced losses are known to amount up to 0.6 dB/km at

1550 nm and 1.5 dB/km at 1590 nm [Bea83]. Hence, our results are approved by former studies of hydrogen-contaminated fibers. The increasing ringdown time differences and hence the rising additional loss with increasing wavelength can be attributed to the wings of absorption peaks of hydrogen between 1590 nm and 2500 nm. These peaks arise due to the excitation of combinations of the H_2 stretching vibration and the H_2 rotational vibrations or the combinations of the H_2 stretching vibration and the SiO_4 lattice vibration [Uch86] whereby the fundamental absorption peak of H_2 is located at 2420 nm [Bea83]. Figure 4.16 shows the saturated additional loss due to the H_2-diffusion in the silica-based fiber cavity.
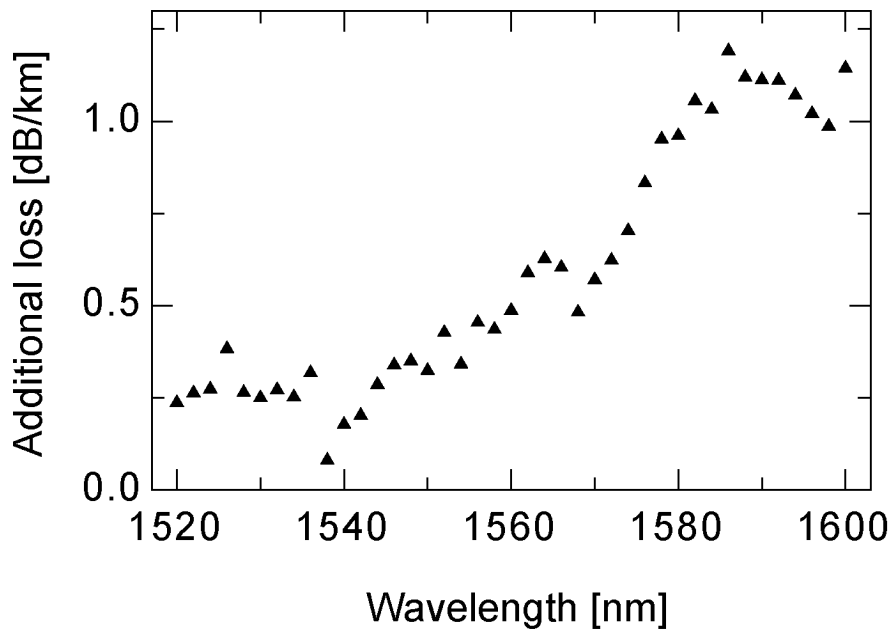

Figure 4.16: Additional loss caused by hydrogen absorption

A hydrogen saturated 10 m-long fiber cavity shows an reversible, enhanced loss.

The temporal evolution of the ringdown time during the out-diffusion process was investigated with the experimental arrangement introduced in section 4.4.2 by measuring the ringdown times at the wavelength of 1590 nm of ma-

ximum additional loss every 24 hours. During the diffusion process, the fiber was placed in an oven in a H_2-free atmosphere of ambient air at a temperature of 30° C. Based on Eq. (4.1), the time-dependent cavity ringdown time $\tau_{H_2}(t)$ of a hydrogen contaminated fiber cavity can be written as:

$$\tau_{H_2}(t) = \frac{t_r}{2\left[(1-R) + \alpha_o L + \alpha(t)L\right]} = \frac{Ln_{eff}}{c_o\left[(1-R) + \alpha_o L + \alpha(t)L\right]}, \quad (4.27)$$

where t_r is the photon transit time for a round trip in a cavity of length L. α_o denotes the intrinsic fiber loss coefficient ($\leq$ 0.3 dB/km @ 1550nm [Cor1]) and $\alpha(t)$ the time-dependent loss coefficient due to dissolved hydrogen diffusion in the fiber cavity.

We revert to the temperature-dependent diffusion coefficient $D_{H_2-silica} = 3.336 \cdot 10^{-15}$ m^2/s [Lem91] at 30° C and calculate $\alpha(t)$ according to Eq. (4.24) by using α_s from the measured ringdown times at 1590 nm. The calculated time-dependent additional absorption coefficients $\alpha(t)$ are converted to ringdown times by using the measured reflectivity and by solving Eq. (4.27). Finally, the calculated ringdown times are compared with the measured ringdown times during the dry-diffusion process at 1590 nm, i.e. at a peak of H_2-induced losses (see also Fig. 4.16). The measured ringdown time during the out-diffusion process and the result of the calculation are given in Fig. 4.17. Good agreement is found between the calculated and the measured ringdown times confirming our assumption of the linear correlation between the hydrogen concentration and the hydrogen-induced loss in a fiber and the neglect of the hydrogen diffusion process in the outer polymer jacket. The only parameters used for the calculation are $b = 62.5$ μm (given by the manufacturer specification), $D_{H_2-silica} = 3.336 \cdot 10^{-15}$ m^2/s [Lem91], and the initial and final measured ringdown times 6.7 μs and 10.2 μs, respectively.
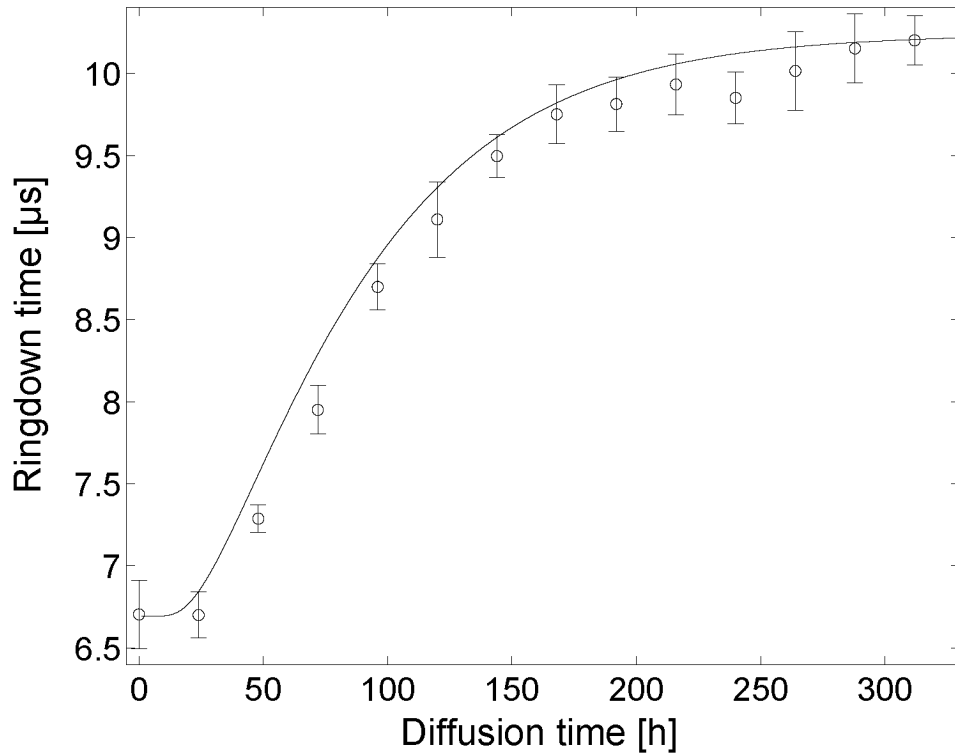
Figure 4.17: Ringdown times during H_2-out diffusion at 1590 nm
Ringdown times during H_2-diffusion out of the fiber cavity recorded at
1590 nm. Measured ringdown times (○), calculated ringdown times (—)
derived from H_2 diffusion modeling

The ringdown times were also measured at 1600 nm during the hydro-
gen dry-diffusion process indicating the reliability of the fiber cavity ringdown
method and of the theoretical consideration. The measurements are depicted
in Fig. 4.18. The ringdown times are shorter compared to the measured times
at 1590 nm due to the lower reflectivity of the mirrors at 1600 nm than at
1590 nm (see Fig. 4.15). Nevertheless, good agreement is found again between
the measured ringdown and calculated times.

We can reconceive the measured data and determine the diffusion coefficient
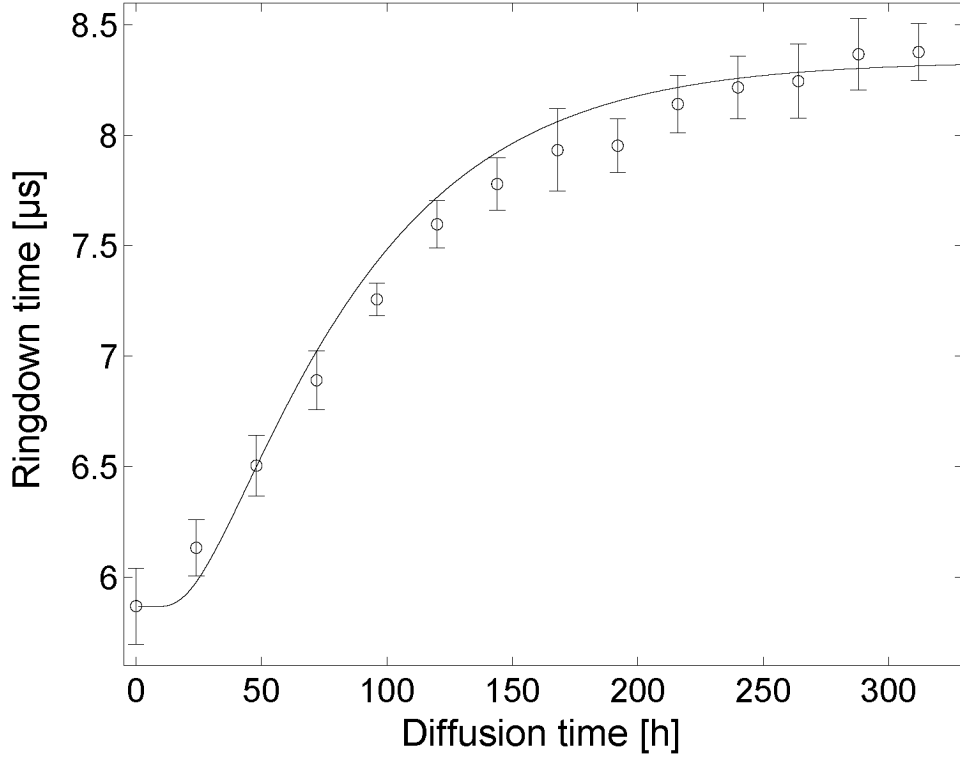$D_{H_2-silica}$ of hydrogen in silica at 30° C and approximate Eq. (4.17) as follows:

Figure 4.18: Ringdown times during H$_2$-out diffusion at 1600 nm

Ringdown times during H$_2$-diffusion out of the fiber cavity recorded at 1600 nm. Measured ringdown times (○), calculated ringdown times (—) derived from H$_2$ diffusion modeling

$$f(\frac{r}{b}, \frac{Dt}{b^2}) \approx 2\frac{J_o\left(j_1\frac{r}{b}\right)exp\left(-j_1^2\frac{Dt}{b^2}\right)}{j_1 J_1\left(j_1\right)}. \tag{4.28}$$

This approximation is justified since j_n (the nth zeros of the Bessel function $J_o\left(j_n\right) = 0$) significantly increases with increasing index n and thus, the exponential term rapidly decreases with progressed diffusion time. By taking into account the first two zeros of J_o ($j_1 = 2.4048$, $j_2 = 5.5201$ [Bro95]), the error of the approximation will be less than 1 % for times $t \geq 55$ h. In consideration

of $J_o(0) = 1$, the normalized concentration in the fiber core, i.e. Eq. (4.24), can be approximated as:

$$\frac{C\left(r=0,t\right)}{C_s} = \frac{\alpha(t)}{\alpha_s} \approx 2\frac{exp\left(-j_1^2\frac{Dt}{b^2}\right)}{j_1 J_1\left(j_1\right)} = Aexp\left(-\frac{t}{t_o}\right), \qquad (4.29)$$

where A and t_o denote two constant values. This approximation allows also an estimation of the saturation time t_s after which the concentration of hydrogen $C(r=0,t)$ reaches 95 % of the saturated hydrogen concentration in the fiber core. One gets:

$$t_s = \frac{0.6b^2}{D}. \qquad (4.30)$$

It results a saturation time of about $t_s = 193.8$ h $= 8.1$ d at 30° C for hydrogen in a silica-based fiber featuring a cladding radius of $b = 62.5$ μm. Consequently, the exposure time of the fiber to hydrogen in the container for 2 weeks was long enough to ensure a hydrogen saturation. But this long time also shows us the drawback of a potential use of the FCRD scheme as hydrogen sensor. The response time for the determination of hydrogen is very long due to the thick silica cladding layer surrounding the fiber core.

Figure 4.19 shows the measured time-dependent evolution of the normalized additional loss at 1590 nm owing to hydrogen and the corresponding fit-function based on Eq. (4.29). According to Eq. (4.24), a calculation of the concentration of diffused H_2-molecules inside the fiber per unit volume would also be possible. The number of hydrogen molecules dissolved in silica glass per unit volume under equilibrium condition can be set to be equal to the saturation concentration $C_s = 2.6 \cdot 10^{18}$ cm^{-3} at 30° C [Sha72]. The first

measured data point at the diffusion time $t = 0$ s is neglected. Furthermore, Fig. 4.19 depicts the absolute H_2-concentration during the dry-diffusion process in the fiber cavity. The extracted diffusion coefficient of hydrogen in silica from the measured data amounts to: $D_{H_2-silica} = (3.02 \pm 0.07)\cdot10^{-15}$ m^2/s at 30° C. Our result lies between the diffusion coefficients $D_{H_2-silica} = 3.336\cdot10^{-15}$ m^2/s [Lem91] and $D_{H_2-silica} = 1.5\cdot10^{-15}$ m^2/s [She77] for room temperature. This emphasizes the good agreement between the measurements, the theory including the assumption of the proportionality between H_2 concentrations and additional losses and the approximation (see Eq. (4.29)) as well as the data found in literature. Last but not least, the good agreement underlines the potential of the fiber cavity ringdown scheme.
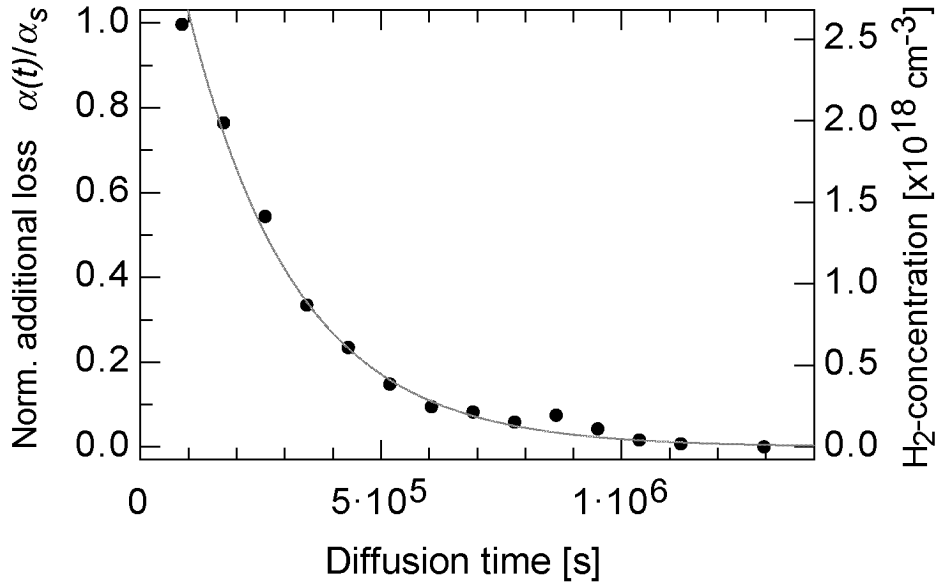

Figure 4.19: Additional loss during H_2-out diffusion at 1590 nm

Measured normalized additional loss (•) during H_2-dry-diffusion process in the fiber cavity at 1590 nm, exponential fit-function (——) from which the diffusion coefficient of H_2 in silica is determined as $(3.02 \pm 0.07)\cdot10^{-15}$ m^2/s.

4.4.4 Conclusion

We demonstrated the performance of a 10 m-long fiber cavity ringdown sensor for hydrogen diffusion. Compared to the well-known cut-back method [Mar81], this fiber cavity sensor requires only a short fiber cable to detect hydrogen. An appreciable increase of additional optical loss due to diffused hydrogen molecules in silica in the wavelength range of 1560 - 1600 nm was observed which can be attributed to wings of absorption peaks between 1590 nm and 2.5 μm. An induced maximum additional loss of 1.2 dB/km was found at 1586 nm. The difference of the ringdown times before and after the diffusion of gaseous hydrogen is 3.5 μs and the measured ringdown times during the diffusion showed good agreement with a theoretical diffusion model. Vice versa, this scheme can also be used to determine the diffusion coefficient of hydrogen in silica and to estimate the absolute hydrogen concentration inside the silica fiber.

4.5 State-of-the-art fiber cavity ringdown research

This subsection gives a short overview of actual and ongoing fiber cavity ringdown studies and summarizes the different fiber cavity realizations.

In 2002, fiber cavities were formed by fiber Bragg gratings (FBG) in a germanium/boron-co-doped fiber (100 dB/km intrinsic loss) and by hydrogen-loaded FBG in an ordinary silica-based fiber (intrinsic loss < 0.3 dB/km) [Gup02]. A finesse of 1276 was measured in the 2.9 cm-long Ge/B-doped fiber. Furthermore, a 10 m-long standard single-mode fiber cavity was used for loss measurement induced within the fiber by variation of the refractive index of the medium surrounding the fiber core, i.e. by exposing the evanescent wave of the core to a glycerin-water mixture. The optical loss was determined by the pulsed cavity ringdown scheme.

Also in 2002, pulsed, visible and near-infrared light was coupled into an optical fiber-loop [Bro02]. The loop was realized by splicing together a winded multi-mode fiber and laser pulses of a dye laser (780 - 840 nm) were coupled directly through the fiber cladding. The transmission of the optical splice and the light absorption by a liquid sample inserted into the optical loop were measured by the cavity ringdown technique. The determination of the ringdown time required a biexponential model to separate two discrete ringdown times attributed to separate components of light traveling in the cladding and in the core of the fiber. An absolute detection limit for 1,1'-diethyl-4,4'-dicarbocyanine of less than $2 \cdot 10^{-15}$ mol in dimethyl sulfoxide was achieved. The measurement with the same arrangement was expanded to the determination of macrobending losses and of displacement losses [Ton03]. In addition, a microchannel was realized in a polymer between the fiber ends and an absolute detection limit for 1,1'-diethyl-4,4'-dicarbocyanine of about 10^{-10} mol was detected in the this microfluidic device.

A fiber cavity ringdown pressure sensor was presented in 2004. Two identical 2 x 1 fiber coupler formed a 61 m-long fiber loop whereby the two one-leg ends and the two 99 % leg ends were spliced together [Wan04₁]. When a force was applied to a section of the fiber loop, an induced loss occurred which was proportional to both the change in the ringdown time and the applied pressure. The results were achieved by the use of a pulsed as well as a continuous-wave laser. The driver current of the laser was turned off when a ringup event was detected. A minimum detectable loss difference of 0.005 dB was measured.

In the same year, a cavity ringdown strain gauge with a biconical tapered single-mode fiber was reported [Tar04₁]. Again two fiber couplers formed a 2.2 km-long fiber cavity and the tapered fiber was spliced into the resonator. An amplitude-modulated near-infrared laser was coupled into the fiber resonator and a motorized translation stage shifted the tapered fiber in the micron range. A minimum detectable displacement of 74 nm was achieved over a 10 mm taper length. Furthermore, nearly the same setup was used to sense 1-octyne in a solvent [Tar04₂]. A 28 mm-long tapered fiber with a 10 μm waist

in a fiber loop allowed to measure a minimum detectable concentration of 1.05 % 1-octyne in a non-interacting solvent. Thereby, the loss per round trip pass was about 21.7 % resulting in a ringdown time of 52 μs in the 2.2 km long fiber loop.

Table III summarizes the different realizations of fiber cavities with their advantages and drawbacks.

Table III: Fiber cavity overview

Overview of the different fiber cavity realizations with their advantages and drawbacks

Realization	advantage	drawback	reference
Fiber Bragg grating	high finesse short cavity	narrowband expensive	[Gup02]
Fiber coating	broadband high finesse short cavity	expensive	[Vog03, Vog05]
Fiber couplers	broadband cheap	low finesse long loop	[Wan04$_1$] [Tar04$_1$, Tar04$_2$]
Fiber loop	broadband high finesse cheap	high incoupling loss time extraction	[Bro02, Ton03]

4.6 Outlook

The fiber cavity ringdown technique is a promising method in the exact determination of any kind of losses in a fiber. This opens a wide range of applications in the field of fiber characterization, fiber development and fiber sensor technology. We demonstrated that this technique can be used for the determination of minute bending losses in special bend insensitive fiber where other loss measurement techniques come to their limits. Therefore, it can play an important role in the further development of bend insensitive fibers featuring a special refractive index profile within the fiber. In addition, this method is also suitable for the characterization of any kind of fiber materials and forms. Especially the search for a fiber material with low losses in the mid-infrared is still an ongoing progress [Ngu03, San94], but also the research for materials well-suited for the last mile transmission in the near-infrared range or the search for characterization schemes of any kind of fiber forms like D-shaped fibers, fiber taper or photonic crystal fibers are ongoing [Sor01, Bag03].
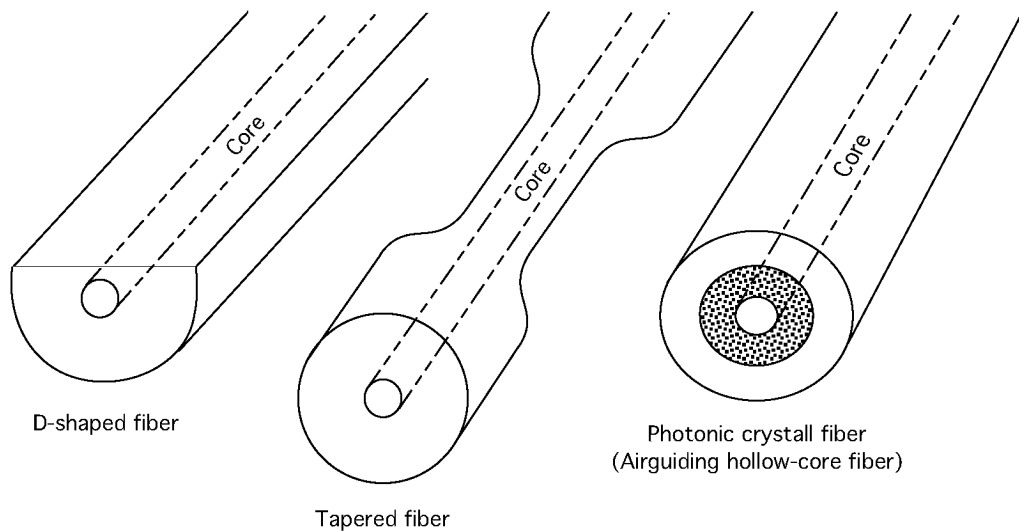

Figure 4.20: **Different types of fibers**

Beside the characterization of materials, the fiber cavity ringdown can also

be used in combination with special fibers like D-shaped fibers for example. A D-shaped fiber demonstrated already its use for evanescent wave detection of methane [Cul92]. But it was also pointed out that the sensitivity of gas detection systems using evanescently coupled waveguides is rather low due to the small optical absorption in the gas. Initial experimental results indicated a resolution of 1000 ppm methane by using a 5 m-long D-fiber. Later, a minimum detectable methane concentration of about 40 % methane was obtained in a 80 cm-long D-shaped fiber [Jin95]. The cavity ringdown scheme would enhance the interaction time of the light within the sensing element and thus improve the sensitivity of such an evanescent wave detector.

Another promising study is the combination of the ringdown technique with a tapered fiber sensor. In [Vil03], a palladium-coated single-mode tapered fiber was described for the detection of hydrogen. The fabricated tapered fibers had losses < 0.1 dB and consequently, they would be suitable for the cavity ringdown scheme. We could measure a maximum loss of about 1 dB per roundtrip (see section 4.3.3). The experiment was extended to cladded multimode fiber tapers [Vil04]. With the use of multimode fibers (graded-index fibers with core-diameter of 50 μm and 62.5 μm), the interaction between the evanescent field and the measurand was improved but at the cost of the fiber transmission. However, the loss did not exceed 0.8 dB in the fiber tapers with a taper length of 5 mm and a uniform taper waist diameter between 15 μm and 85 μm. It was observed that the tapering losses of parabolic tapers were higher (> 1 dB). In addition to refractive index measurements, fiber tapers were used to record a spectrum of water with a dissolved organic blue dye and they were also used to measure hydrogen. In the latter measurement, the tapered fiber part was coated with a palladium layer. A palladium coated taper was also implemented in a erbium-doped fiber laser cavity for hydrogen determination [Bar04]. Contrary to [Vil03], a taper loss of 10 dB was reported and a round-trip loss of approximately 24 dB. The change of hydrogen concentration affected the losses inside the cavity and hence the buildup time of the laser. A response time of about 90 s and a recovery time of 450 s were recorded. Tapers with such high losses are not suited for the fiber cavity ringdown scheme.

However, a connection between the coated fiber tapers and fiber cavity took place. Another promising hydrogen sensor contains tungsten oxide coated on a 200 μm quartz-core/plastic-cladding fiber [Oka03]. The sensor used platinic acid as a precursor. Thereby, 1 % hydrogen showed a loss of 75 %. All these former works could help in the implementation of a tapered cavity ringdown scheme.

A new type of evanescent fiber sensor was development in the last years. It consists of special fibers, the so-called holey or photonic crystal fibers. The light in its core is guided by very small air cylinders pervading the silica-cladding. By filling these holes with an absorbing material, the evanescent field is absorbed and the transmissions with and without the species gas can be compared resulting in a transmission spectrum. First implementation and measurement were reported by [Mon99, Hoo02, Hoo03]. Other studies showed the feasibility of holey fibers for gas sensing of species like acetylene, methane or ammonia but also biomolecules in aqueous solutions were measured in photonic crystal fibers[Rit04, Jen04]. A drawback of this method is the fact that the air lines are within the cladding which makes a filling of them with gas difficult. Nevertheless, a compact and stable gas cell within a photonic crystal fiber was reported recently [Ben05].

Chapter 5

Conclusion and Outlook

This thesis concerned open-path and fiber-based cavity ringdown techniques in the near-infrared range. An open-path cavity ringdown experiment was set up with reliable and cost-effective telecommunication devices and fibers. In addition, a new micro- and macro-scale length-variable cavity gas cell was designed and made in-house. The cell layout included the important feature of cavity mirror alignment from outside the gas cell. Moreover, the involvement of fiber-coupled devices eased the light handling and the alignment procedure. For the evaluation of the cavity ringdown time, a fast algorithm analyzing the exponential intensity decay was implemented in a newly-written LabView program by which also the experimental process was automated. A detection limit, e.g. for acetylene, of 67 ppbV in synthetic air in a hermetically sealed gas cell was achieved at at total pressure of 100 mbar and at 1530.37 nm. This limit is based on a minimum detectable absorption coefficient of $6.2 \cdot 10^{-6}$ m^{-1} (SNR = 3). With a collecting rate of ringdown events of 20 Hz, it results a sensitivity of $1.38 \cdot 10^{-8}$ cm^{-1} Hz$^{-1/2}$. Compared to other sensitivities reported in the near-infrared range, our value is in the same order or above. Hence, this sensitivity is not adequate in order to replace gas chromatographs in petrochemical facilities. An acetylene isotope ratio was also measured in the near-infrared range and a good agreement with literature data was achieved. In addition to acetylene measurements in synthetic air, acetylene - ethylene mixtures were also investigated as acetylene is sometimes

present as impurity in an ethylene gas stream in petrochemical industry. For these studies, the acetylene concentration was measured in steps of 250 ppbV or 500 ppbV in a gas flow configuration. Well-resolved absorption profiles were found during the flow measurements and an excellent linear relationship between the absorption coefficient and the concentration was found. However, the gas flow configuration increased the minimum detectable acetylene concentration to 175 ppbV and 460 ppbV, respectively, at a total pressure of 20 mbar and at room temperature. In order to improve the sensitivity of the setup, the cavity alignment system should be totally incorporated in the gas cell. Such a configuration would prevent a pressure difference on the mirrors and ensure a more stable fixing of the mirrors. Moreover, a self-alignment mechanism and a single-ended detection scheme could also be considered. Finally, the good spectral resolution of our cavity ringdown system could be demonstrated with isotope ratio measurements of C_2H_2 isotopomers. In particular, the isotope ratio ($H^{13}C$-^{12}CH / $H^{12}C$-^{12}CH) was determined and good agreement with literature data was found.

A fiber cavity ringdown scheme with coated fiber end facets was successfully implemented by our group for the first time. Bending losses in silica-based single-mode fiber cavities were accurately measured and confirmed by a theoretical model. Both, the experimental results and the model showed bending loss oscillations with respect to the curvature radius caused by a coherent coupling between the core-propagating field and the fraction of the field reflected by the cladding coating or coating air interfaces. A minimum loss detection limit per cavity roundtrip of $1.72 \cdot 10^{-3}$ dB was obtained in a 10 m-long silica-based fiber cavity. This value would allow a reliable determination of bending losses even in special bend-insensitive fibers where a bending loss of about $5 \cdot 10^{-2}$ dB occurs when the fiber is winded 30 times on a 20 mm-thick mandrel. Moreover, the good results were confirmed by bending loss measurements in shorter fiber cavities, namely 0.2 m and 1 m.

In addition to bending loss determinations in fiber cavities, an absorption spectrum of a 10 m-long hydrogen-saturated silica-based fiber cavity and

the absorption developing during the diffusion process of hydrogen out of the fiber cavity were recorded. The absorption values found in the spectrum were confirmed by literature data. The theoretical diffusion aspect in fibers was considered and adapted to the new fiber cavity ringdown scheme in order to understand the absorption decrease during the hydrogen out-diffusion process. A good agreement between the derived theoretical model and the recorded ringdown times was found. Vice versa, the fiber cavity ringdown technique was also used to determine the diffusion coefficient of hydrogen in silica ($D_{H_2-silica}$ = $(3.02 \pm 0.07) \cdot 10^{-15}$ m^2/s at 30° C) and to estimate the absolute hydrogen concentration inside the silica fiber. The value of the determined diffusion constant lay between diffusion coefficients $D_{H_2-silica}$ found in literature.

Convinced by the excellent agreements between the recorded fiber cavity ringdown measurements and the theoretical models and literature data, it is believed that the ability of minute loss measurements within a fiber cavity combined with different fiber types will open a wide application range of the fiber cavity ringdown scheme. The cavity-enhanced effect of this method can improve evanescent-wave absorption measurements in, e.g., D-shaped or tapered fibers. Moreover, cavities can be formed in crystal fibers filled with a gas sample whereby the cavity ringdown technique can be used for accurate gas measurements totally embedded in fibers. Therefore, we believe this technique will stimulate researchers for new and exciting studies in the future.

Appendix

Beer-Lambert law

Various detection schemes have been introduced for spectroscopic gas studies in the history of gas analysis. One of them is the multipass absorption spectroscopy based on the well-known Beer-Lambert law which relates the unitless absorbance A with the concentration of the absorbing medium c_M [M] and the optical path length z within the medium [Dem03]:

$$A(\lambda, z) = \epsilon(\lambda)c_M z, \tag{1}$$

where λ denotes the actual wavelength and ϵ denotes the molar absorptivity $[\text{cm}^{-1}\text{M}^{-1}]$ also called the molar extinction coefficient. In the case of several species in a mixture absorbing at the same wavelength, the different absorbances are additive. The Beer-Lambert law can also be written in terms of light intensities irradiated on the medium (I_{inc}) and transmitted through the absorbing species (I_{trans}) after the optical path length z:

$$
\begin{aligned}
I_{trans}(\lambda, z) &= I_{inc}\exp\left[-\alpha(\lambda)z\right] = I_{inc}\exp\left[-\alpha_m(\lambda)Cz\right] \\
&= I_{inc}\exp\left[-N\sigma(\lambda)z\right],
\end{aligned}
\tag{2}
$$

where $\alpha(\lambda)$ $[\text{cm}^{-1}]$, $\alpha_m(\lambda)$ $[\text{cm}^{-1}]$ denote the absorption and the molecular

absorption coefficients, respectively, C denotes the concentration in numbers of the absorbing molecules, N [cm^{-3}] is the molecule density of the absorbing gas and $\sigma(\lambda)$ [cm^2] is the molecular cross section. Equation (2) implies that $\alpha(\lambda) = \alpha_m(\lambda) = N\sigma(\lambda)$. Often, we are interested in the ratio between the transmitted and the incident intensities, i.e. in the transmission T defined as:

$$T(\lambda, z) = \frac{I_{trans}(\lambda, z)}{I_{inc}(\lambda)} = \exp\left(-\alpha(\lambda)z\right) = \exp\left(-N\sigma(\lambda)z\right). \tag{3}$$

Hence, the transmission is not proportional to the concentration but proportional to the absorbance A. The absorbance and the transmission are related as follows:

$$A(\lambda, z) = -\log_{10} T(\lambda, z) = \frac{\alpha_m(\lambda)cz}{\ln(10)} = \frac{N\sigma(\lambda)z}{\ln(10)}. \tag{4}$$

The sensitivity and the accuracy of gas measurements depend on the gas sample $\sigma(\lambda)$ and on the absorption path length z of light. Therefore, long-path or multipass cells have been introduced for sensitive gas studies. The most common cells are the so-called Herriot cells and White cells [Her65, Whi42]. The Herriot cell is formed by two spherical or aspherical mirrors reflecting the light in an elliptical or Lissajous arrangement whereby the light is coupled into the cell by a hole in a mirror. The White cell contains three concave mirrors making the alignment stability more critical than in a Herriot cell. The White cell features a better volume path length ratio and the light coupling into the cell is realized by transfer mirrors. Consequently, the mirror alignment is less critical in a Herriot cell but the volume path length ratio is larger in a White cell. However, interference fringes caused by the cell windows in a White cell are hardly to prevent.

List of abbreviations and mathematical symbols

Abbreviations

Abbreviaton	Meaning
AOM	acousto-optical modulator
AR	anti-reflection
C_2H_2	acetylene
C_2H_4	ethylene
CAPS	cavity-attenuated phase-shift
CO	carbon monoxide
CO_2	carbon dioxide
CRD	cavity ringdown
CRDS	cavity ringdown spectroscopy
cw	continuous-wave
ECDL	external cavity diode laser
EDFA	erbium doped fiber amplifier
FBG	fiber Bragg grating
FC	fiber collimator
FCP	fiber coupler
FC/PC	fiber connector/physical contact
FCRD	fiber cavity ringdown
FT	Fourier transform
Ge	germanium
H_2	hydrogen
H_2O	water
HeNe	helium-neon
InGaAs	indium-gallium-arsenid
IR	infrared
ITU	internation telecommunication union

Abbreviaton	Meaning
KW	total hydrocarbons
L	lens
LM	Levenberg-Marquardt
MEAN	mean value
MH	Matheson-Halmer
MIR	middle-infrared range
N_2	nitrogen
Nd^{3+}	neodym
NIR	near-infrared range
NO_x	nitrogen oxides
O_2	oxygen
OH	hydroxyl
OHD	optical heterodyne detection
PC	polarization controller
PD	photodiode
PET	polyethylene terephthalate
ppmV	parts per million per volume
ppbV	parts per billion per volume
PZT	piezo transducer
SEM	standard error of the mean
Si	silicon
SiO_2	silica, quartz
SNR	signal to noise ratio
TEM	transverse electromagnetic mode
TIR	total-internal-reflection
TNT	trinitrotoluene
TATP	triacetone triperoxide
UV	ultraviolet

Mathematical symbols (Latin symbols)

Mathematical symbol	Meaning
a	core radius of a fiber
Ai	Airy-function
$\mathcal{A}_B$	bending loss [dB/m]
Bi	Airy-function

Mathematical symbol	Meaning
b	fiber cladding expansion
c	speed of light
c_o	speed of light in vacuum
C	concentration
C_s	saturated concentration
D	diffusion coefficient
E	electric field amplitude
f	frequency
$\mathcal{F}$	finesse
g	g-parameter
h	Planck's constant
i	imaginary number
I	intensity
I_a	maximal output current
j_n	n^{the} zero of the Bessel function J_o
J_o	Bessel function
k	wavevector
k_B	Boltzmann constant
K	capacitance
K_1	modified Bessel function
l	length within a cavity
L	cavity length
L_{eff}	effective path length
m	mass
n	refractive index
n_1	refractive index of a fiber core
n_2	refractive index of a fiber cladding
n_3	refractive index of a fiber coating
n_{eff}	effective refractive index in a fiber
n_{res}	resulting refractive index in a fiber
N_s	number of solubility sites available per unit volume
p	hydrogen partial pressure
q	longitudinal mode number
r	radius
r_c	fiber core radius
R	gas constant
R	intensity reflection coefficient

Mathematical symbol	Meaning
$\tilde{R}$	measure of the mirror reflectivities
$\mathcal{R}_o$	experimental (= geometric) curvature radius of a bent fiber
$\mathcal{R}_{eff}$	effective curvature radius of a bent fiber
$\mathcal{R}_F$	curvature radius of a bent fiber
$\mathcal{R}_M$	curvature radius of a mirror
s	diffusion rate per unit area
t	time
t_r	round trip time of light within a cavity
t_s	saturation time
T	absolute temperature
T	intensity transmission coefficient
$\mathcal{T}$	cavity transmission
u	azimuth mode number
U_{max}	maximal bias
V	normalized frequency
V_o	binding energy
w	radial mode number
W_o	waist radius of a Gaussian beam
W_e	end mirror spot radius of a Gaussian beam

Mathematical symbols (Greek symbols)

Mathematical symbol	Meaning
α	intensity absorption coefficient
α_o	intrinsic loss coefficient of a straight fiber
α_B	additional absorption coefficient in a fiber
$\alpha(t)$	total loss coefficient of a hydrogen saturated fiber
α_s	additional absorption coefficient in a hydrogen saturated fiber
α_t	mean loss factor
β	propagation constant
Δ	Laplace operator
$\mathcal{E}$	Young's modulus
$\triangle\zeta$	phase shift

Mathematical symbol	Meaning
λ	wavelength
ν	frequency
ν_F	free spectral range
ν_T	mode space between neighboring transverse mode
ω	angular frequency
ρ	total intensity attenuation per round trip within a cavity
σ	tensile strength
τ_o	ringdown time of a cavity with no absorbing medium between the mirrors
τ	cavity ringdown time
τ_B	fiber cavity ringdown time with additional loss
τ_{H_2}	cavity ringdown time of hydrogen-saturated fiber
$\triangle\tau$	minimum accurately detectable ringdown time
ϕ	elasto-optic coefficient

List of Figures

List of Tables

Bibliography

Chapter 1

[AlA04] L. Al-Amoodi, C.A. Roberts. J. Workman, J.B. Reves III. *Near-infrared spectroscopy in agriculture*, American Society of Agronomy ASA, Madison WI (2004)

[Bla98] M. Blanco, J. Coelle, H. Iturriaga, S. Maspoch, and C. de la Pezuela. *Near-infrared spectroscopy in the pharmaceutical industry*, Analyst **123**, 135R-150R (1998)

[Bas03] G. von Basum, H. Dahnke, D. Halmer, P. Hering, and M. Mürtz. *Online recording of ethane traces in human breath via infrared laser spectroscopy*, J. Appl. Physiol. **95**, 2583-2590 (1998)

[Bun01] A.F. Bunkin and K.I. Voliak *Four-photon Raman spectroscopy as a method of the ocean remote sounding*, Proceedings of SPIE **4749**, 75-85 (2001)

[Cas04] A. Castrillo, G. Casa, M. van Burgel, D. Tedesco, and L. Gianfrani. *First field determination of the $^{13}C/\,^{12}C$ isotope ratio in volcanic CO_2 by diode-laser spectrometry*, Opt. Express **12**, 6515-6523 (1998)

[Con03] Personal conversation with Dr. H. Brändle, ABB Corporate Research Ltd. Switzerland, Baden-Daettwil (2003)

[DeL05] F.C. DeLucia Jr., A.C. Samuels, R.S. Harmon, R.A. Walters, K.L. McNesby, A. LaPointe, R.J. Winkel Jr., and A.W. Miziolek. *Laser-induced breakdown spectroscopy (LIBS): A promising versatile chemical sensor technology for hazardous material detection*, IEEE Sens. J. **5**, 681-689 (2005)

[Dem01] J. Demaison, K. Sarka, and E.A. Cohen. *Spectroscopy from space*, Kluwer Academic Publishers, London (2001)

[Dem03] W. Demtröder. *Laser spectroscopy*, Springer, Berlin (2003)

[Din51] H. Dingle. *A hundred years of spectroscopy*, Blackwell scientific publications, Oxford (1951)

[EBS]   Encyclopaedia Britannica. *Spectroscopy*, Encyclopaedia Britannica Online (2005)

[Eyr02]   M.B. Eyring. *Spectroscopy in forensic science*, in: R. Meyers, editor. *Encyclopedia of physical science and technology*, Academic Press, San Diego (2002)

[Fer00]   N. Ferrer. *Forensic science, applications of IR spectroscopy*, in: G. Tranter, H. Holmes, J. Lindon, editors. *Encyclopedia of spectroscopy and spectrometry*, Academic Press, London (2000)

[Fis04]   C. Fischer. *Trace-gas sensing with a pulsed difference frequency laser spectrometer and three different detection schemes*, Mensch & Buch Verlag, Berlin (2004)

[Fre03]   T. Freeman. *Speciality fibre: component opportunities beckon*, FibreSystems, September, 22-26 (2003)

[Joh91]   S. Johnston. *Fourier transform infrared*, Ellis Horwood, London (1991)

[Koe01]   J.L. Koenig. *Infrared and Raman spectroscopy of polymers*, in S. Ward, editor. *Rapra Review Reports 134*, Rapra Technology, Shawbury (2001)

[Mai60]   T.H. Maiman. *Stimulated optical radiation in ruby*, Nature **187**, 493-494 (1960)

[Mar03]   D. Marinov and M.W. Sigrist. *Monitoring of road-traffic emission with mobile photoacoustic system*, Photochem. and Photobiol. Sciences **2**, 774-778 (2003)

[Mar05]   D. Marinov and M.W. Sigrist. *Human breath analysis employing DFG laser spectroscopy*, Dig. CLEO-Europe 2005, Paper CD-3-Mon, Munich (D), June 12-17 (2005)

[McC03]   W.F. McClure. *204 years of near infrared technology: 1800-2003*, J. Near Infrared Spetrosc. **11**, 487-518 (2003)

[Mel52]   T. Melvill. *Observation of Light andColours*, Physical and Literary Essays, Edinburgh, (1752)

[Mur05]   M. Mürtz. *Breath diagnostics using laser spectroscopy*, Opt. Photon. News **16**, 30-35 (2005)

[Mic03]   K.H. Michaelian. *Photoacoustic infrared spectroscopy*, John Wiley & Son, New York (2003)

[OKe88]   A. O'Keefe and D.A.G. Deacon. *Cavity ring-down optical spectrometer for absorption measurements using pulsed laser sources*, Rev. Sci. Instrum. **59**, 2544-2551 (1988)

[Pau05] A.N. Paunel, A. Dejam, S. Thelen, M. Kirsch, M. Horstjann, P. Gharini, M. Mürtz, M. Kelm, H. de Groot, V. Kolb-Bachofen, and C.V. Suschek. *Enzyme-independent nitric oxide formation during UVA challenge of human skin: characterization, molecular sources, and mechanisms*, Free Radical Biology and Medicine **38**, 606-615 (2005)

[San03] I.E. Santosa, L.J.J. Laarhoven, J. Harbinson, S. Driscoll, and F.J.M. Harren. *Laser-based trace gas detection of ethane as a result of photo-oxidative damage in chilled cucumber leaves*, Rev. Sci. Instrum. **74**, 680-683 (2003)

[Sig94] M.W. Sigrist. *Introduction to environmental sensing*, in: M.W. Sigrist, editor. *Air monitoring by spectroscopic technique*, John Wiley & Son, New York (1994)

[Suva] Suva. *Grenzwerte am Arbeitsplatz 2005*, Schweizerische Unfallversicherungsanstalt, CH (2005)

[Tod02] M.W. Todd, R.A. Provencal, T.G. Owano, B.A. Paldus, A. Kachanov, K.L. Vodopyanov, M. Hunter, S.L. Coy, J.I. Steinfeld, and J.T. Arnold. *Application of mid-infrared cavity-ringdown spectroscopy to trace explosives vapor detection using a broadly tunable (6-8 μm) optical parametric oscillator*, Appl. Phys. B **75**, 367-376 (2002)

[Wei05] D. Weidmann, G. Wysocki, C. Oppenheimer, and F.K. Tittel. *Development of a compact quantum cascade laser spectrometer for field measurements of CO_2 isotopes*, Appl. Phys. B **80**, 255-260 (2005)

[Wor96] J. Workman. *A brief review of near infrared in petroleum product analysis*, J. Near Infrared Spetrosc. **4**, 69-74 (1996)

Chapter 2

[And84] D.Z. Anderson, J.C. Frisch, and C.S. Masser. *Mirror reflectometer based on optical cavity decay time*, Appl. Opt. **23**, 1238-1245 (1984)

[Ber00] G. Berden, R. Peeters, and G. Meijer. *Cavity ring-down spectroscopy: Experimental schemes and applications*, Int. Rev. Phys. Chem. **19**, 565-607 (2000)

[Bro95] I.N. Bronstein, K.A. Semendjajew, G. Musiol, and H. Mühlig. *Taschenbuch der Mathematik*, Verlag Harri Deutsch,Frankfurt am Main, 1995

[Bus99]   K.W. Busch and M.A. Busch. *Introduction to cavity-ringdown spec-troscopy*. In: K.W. Busch, M.A. Busch, editors. *Cavity-ringdown spec-troscopy*, Washington: ACS, 1999

[Eng96]   R. Engeln and G. Meijer. *A Fourier transform cavity ring down spec-trometer*, Rev. Sci. Instrum. **67**, 2708-2713 (1996)

[Hal02]   A.J. Hallock, E.S.F. Berman, and R.N. Zare. *Direct monitoring of absorption in solution by cavity ring-down spectroscopy*, Anal. Chem. **74**, 1741-1743 (2002)

[He00]   Y. He and B.J. Orr. *Ringdown and cavity-enhanced absorption spec-troscopy using a continuous-wave tunable diode laser and a rapidly swept optical cavity*, Chem. Phys. Lett. **319**, 131-137 (2000)

[He01]   Y. He and B.J. Orr. *Optical heterodyne signal generation and detec-tion in cavity ringdown spectroscopy based on a rapidly swept cavity*, Chem. Phys. Lett. **335**, 215-220 (2001)

[He02]   Y. He and B.J. Orr. *Rapidly swept, continuous-wave cavity ringdown spectroscopy with optical heterodyne detection: single- and multi-wavelength sensing of gas*, Appl. Phys. B **75**, 267-280 (2002)

[Her80]   J.M. Herbelin, J.A. McKay, M.A. Kwok, R.H. Ueunten, D.S. Urevig, D.J. Spencer, and D.J. Benard. *Sensitive measurement of photon life-time and true reflectances in an optical cavity by a phase-shift method*, Appl. Opt. **19**, 144-147 (1980)

[Her81]   J.M. Herbelin and J.A. McKay. *Development of laser mirrors of very high reflectivity using the cavity-attenuated phase-shift method*, Appl. Opt. **20**, 3341-3344 (1981)

[Jon95]   R.T. Jongma, M.G.H. Boogaarts, I. Holleman, and G. Meijer. *Trace gas detection with cavity ringdown spectroscopy*, Rev. Sci. Instrum. **66**, 2821-2828 (1995)

[Kwo82]   M.A. Kwok, J.M. Herbelin, and R.H. Ueunten. *Cavity phase shift method for high reflectance measurements at mid-infrared wave-lengths*, Opt. Eng. **21**, 979-982 (1982)

[Lab94]   M. de Labachelerie, K. Nakagawa, and M. Ohtsu. *Ultranarrow $^{13}C_2H_2$ saturated-absorption lines at 1.5 μm*, Opt. Lett. **19**, 840-842 (1994)

[Ler00]   T. von Lerber and A. Romann. *A method for measuring at least one physical parameter using an optical resonator*, European patent ap-plication No. 00121314.9 (9. Oct. 2000)

[Mar96] J. Martin, B.A. Paldus, P. Zalicki, E.H. Wahl, T.G. Owano, J.S. Harris Jr., C.H. Kruger, and R.N. Zare. *Dynamic response of a Fabry-Perot interferometer*, J. Opt. Soc. Am. B **16**, 523-532 (1999)

[OKe88] A. O'Keefe and D.A.G. Deacon. *Cavity ring-down optical spectrometer for absorption measurements using pulsed laser sources*, Rev. Sci. Instrum. **59**, 2544-2551 (1988)

[Pal00] B.A. Paldus, C.C. Harb, T.G. Spence, R.N. Zare, C. Gmachl, F. Capasso, D.L. Sivco, J.N. Baillargeon, A.L. Hutchinson, and A. Y. Cho. *Cavity ringdown spectroscopy using mid-infrared quantum-cascade lasers*, Opt. Lett. **25**, 666-668 (2000)

[Pip97₁] A.C.R. Pipino, J.W. Hudgens, and R.E. Huie. *Evanescent wave cavity ring-down spectroscopy with a total-internal-reflection minicavity*, Rev. Sci. Instrum. **68**, 2978-2989 (1997)

[Pip97₂] A.C.R. Pipino, J.W. Hudgens, and R.E. Huie. *Evanescent wave cavity ring-down spectroscopy for probing surface processes*, Chem. Phys. Lett. **280**, 104-112 (1997)

[Rem92] G. Rempe, R.J. Thompson, H.J. Kimble, and R. Lalezari. *Measurement of ultralow losses in an optical interferometer*, Opt. Lett. **17**, 363-365 (1992)

[Rom97₁] D. Romanini, A.A. Kachanov, N. Sadeghi, and F. Stoeckel. *CW cavity ring down spectroscopy*, Chem. Phys. Lett. **264**, 316-322 (1997)

[Rom97₂] D. Romanini, A.A. Kachanov, and F. Stoeckel. *Diode laser cavity ringdown spectroscopy*, Chem. Phys. Lett. **270**, 538-545 (1997)

[San77] V. Sanders. *High-precision reflectivity measurement technique for low-loss laser mirrors*, Appl. Opt. **16**, 19-20 (1977)

[Sch95] J.J. Scherer, D. Voelkel, D.J. Rakestraw, J.B. Paul, C.P. Collier, R.J. Saykally, and A. O'Keefe. *Infrared cavity ringdown laser absorption spectroscopy (IR-CRLAS)*, Chem. Phys. Lett. **245**, 273-280 (1995)

[Sch97] J.J. Scherer, J.B. Paul, A. O'Keefe, and R.J. Saykally. *Cavity ring-down laser absorption spectroscopy: History, development, and application to pulsed molecular beams*, Chem. Rev. **97**, 25-51 (1997)

[Sie86] A.E. Siegmann. *Lasers*, University Science Books, Mill Valley, California, 1986

[Whe98] M.D. Wheeler, S.M. Newman, A.J. Orr-Ewing, and M.N.R. Ashfold. *Cavity ring-down spectroscopy*, J. Chem. Soc. Faraday Trans. **94**, 337-351 (1998)

[Xu02] S. Xu, G. Sha, and J. Xie. *Cavity ring-down spectroscopy in the liquid phase*, Rev. Sci. Instrum. **73**, 255-258 (2002)

[Zal95] P. Zalicki and R.N. Zare. *Cavity ring-down spectroscopy for quantitative absorption measurements*, J. Chem. Phys. **102**, 2708-2717 (1995)

Chapter 3

[Bae02] D.S. Baer, J.B. Paul, M. Gupta, and A. O'Keefe. *Sensitive absorption measurements in the near-infrared region using off-axis integrated-cavity-output spectroscopy*, Appl. Phys. B **75**, 261-265 (2002)

[Con03] Personal conversation with Dr. H. Brändle, ABB Corporate Research Ltd. Switzerland, Baden-Daettwil (2003)

[Dem88] W. Demtröder. *Laser spectroscopy*, Springer, Berlin (1988)

[EBE] Encyclopaedia Britannica. *Ethylene*, Encyclopaedia Britannica Online (2005)

[Gil01] S.L. Gilbert and W.C. Swann. *Acetylene $^{12}C_2H_2$ absorption reference for 1510 nm to 1540 nm wavelength calibration-SRM 2517a*, NIST Publication 260-133, (2001)

[Hac02] R. El Hachtouki and J. Vander Auwera. *Absolute line intensities in acetylene: the 1.5-μm region*, J. Mol. Spectrosc. **216**, 355-362 (2002)

[Hal04] D. Halmer, G. von Basum, P. Hering, and M. Mürtz. *Fast fitting algorithm for real-time instrumental use*, Rev. Sci. Instr. **75**, 2187-2191 (2004)

[He02] Y. He and B.J. Orr. *Rapidly swept, continuous-wave cavity ringdown spectroscopy with optical heterodyne detection: single- and multi-wavelength sensing of gas*, Appl. Phys. B **75**, 267-280 (2002)

[Hit03] L.S. Rothman et al. *The HITRAN molecular spectroscopic database: edition of 2000 including updates through 2001*, J. Quant. Spectros. Rad. Trans. **82**, 4-55 (2003)

[LGI] *Cavity ringdown mirror reflectivity curve.* Los Gatos Inc., Mountain View, CA (2001)

[Mat87] I.B.C. Matheson. *The method of successive integration: a general technique for recasting kinetic equations in a readily soluble form which is linear in the coefficients and sufficiently rapid for real time instrumental use*, Anal. Instrum. **16**, 3345-373 (1987)

[Pie98] *Amplifiers, D/A converters, electronic HV-switchesfor piezoactuators.* Piezomechanik GmbH, München, D (1998)

[Sie86] A.E. Siegmann. *Lasers*, University Science Books, Mill Valley, CA (1986)

Chapter 4

[Agr92] G.P. Agrawal. *Fiber-Optic Communication Systems*, John Wiley & Son, New York (1992)

[Bag03] J.C. Baggett, T.M. Monro, K. Furusawa, V. Finazzi, and D.J. Richardson. *Understanding bending losses in holey optical fibers*, Opt. Commun. **227**, 317-335 (2003)

[Bar04] Y.O. Barmenkov, A.Ortigosa-Blanch, A. Diez, J.L. Cruz, and M.V. Andres. *Time-domain fiber laser hydrogen sensor*, Opt. Lett. **29**, 2461-2463 (2004)

[Bea83] K.J. Beales, D.M. Cooper, and J.D. Rush. *Increased attenuation in optical fibres caused by diffusion of molecular hydrogen at room temperature*, Electron. Lett. **19**, 917-919 (1983)

[Ben05] F. Benabid, F. Couny, J.C. Knight, T.A. Birks, and P. St J. Russell. *Compact, stable and efficient all-fibre gas cells using hollow-core photonic crystal fibre*, Nature **434**, 488-491 (2005)

[Böh93] R.Böhm, A. Stephani, V.M. Baev, and P.E. Toschek. *Intracavity absorption spectroscopy with a Nd^{3+}-doped fiber laser*, Opt. Lett. **18**, 1955-1957 (1993)

[Bro95] I.N. Bronstein, K.A. Semendjajew, G. Musiol, and H. Mühlig. *Taschenbuch der Mathematik*, Harri Deutsch, Frankfurt am Main (1995)

[Bro02] R.S. Brown, I. Kozin, Z. Tong, R.D. Oleschuk, and H.P. Loock, *Fiber-loop ring-down spectroscopy*, J. Chem. Phys. **117**, 10444-10447 (2002)

[Bus99] K.W. Busch and M.A. Busch. *Introduction to cavity-ringdown spectroscopy*, in: K.W. Busch, M.A. Busch, editors. *Cavity-ringdown spectroscopy*, ACS, Washington (1999)

[Cor1]   *Corning SMF-28 Optical Fiber, product Information*. Corning Inc., Corning, NY (2001)

[Cor2]   *Material safety data sheet for corning optical fibers with colored CPC coating*. Corning Inc., Corning, NY (2000)

[Cra75] J. Crank. *The mathematics of diffusion*, Clarendon Press, Oxford (1975)

[Cul92]   B. Culshaw, F. Muhammad, G. Stewart, S. Murray, D. Pinchbeck, J. Norris, S. Cassidy, M. Wilkinson, D. Williams, I. Crisp, R. Van Ewyk, and A. McGhee. *Evanescent wave methane detection using optical fibres*, Electron. Lett. **28**, 2232-2234 (1992)

[Fau97]   L. Faustini and G. Martini. *Bend loss in single-mode fibers*, J. Lightwave Technol. **(15)** 671-679 (1997)

[Fra81]   D.L. Franzen and E. M. Kim. *Long optical-fiber Fabry-Perot interferometers*, Appl. Opt. **20**, 3991-3992 (1981)

[Fre03]   T. Freeman. *Speciality fibre: component opportunities beckon*, FibreSystems, September, 22-26 (2003)

[Fri83]   H.L. Frisch and S.A. Stern. *Diffusion of small molecules in polymers*, Crit. Rev. in Sol. State and Mat. Sci. **11**, 123-187 (1983)

[Hoo02]   Y.L. Hoo, W. Jin, H.L. Ho, D.N. Wang, and R.S. Windeler. *Evanescent-wave gas sensing using microstructure fiber*, Opt. Eng. **41**, 8-9 (2002)

[Hoo03]   Y.L. Hoo, W. Jin, C. Shi, H.L. Ho, D.N. Wang, and S.C. Ruan. *Design and modeling of a photonic crystal fiber gas sensor*, Appl. Opt. **42**, 3509-3515 (2003)

[Gra00]   K.T.V. Grattan and T. Sun. *Fiber-optic sensor technology: Introduction and overview*, in: K.T.V. Grattan, B.T. Meggit, editors. *Optical fiber sensor technology*, Kluwer Academic Publisher, London (2000)

[Gup02]   M. Gupta, H.Jiao, and A. O'Keefe. *Cavity-enhanced spectroscopy in optical fibers*, Opt. Lett. **27**, 1878-1880 (2002)

[Hum96]   O. Humbach, H. Fabian, U. Grzesik, U. Haken, and W. Heitmann. *Analysis of OH absorption bands in synthetic silica*, J. Non-Cryst. Solids **203**, 16-26 (1996)

[Iln90]   A. Ilno, M. Kuwabara, and K. Kokura. *Mechanism of hydrogen-induced losses in silica-based optical fibers*, J. Lightwave Technol. **8**, 1675-1679 (1990)

[Ito85]   H. Itoh, Y. Ohmori, and M. Nakahara. *Loss increase due to chemical reactions of hydrogen in silica glass optical fibers*, J. Lightwave Technol. **Lt-3**, 1100-1104 (1985)

[Jen04]   J.B. Jensen, L.H. Pedersen, P.E. Hoiby, L.B. Nielsen, T.P. Hansen, J.R. Folkenberg, J. Riishede, D. Noordegraaf, K. Nielsen, A. Carlsen, and A. Bjarklev. *Photonic crystal fiber based evanescent-wave sensor for detection of biomolecules in aqueous solutions*, Opt. Lett. **29**, 1974-1976 (2004)

[Jin95]   W. Jin, G. Stewart, M. Wilkinson, B. Culshaw, F. Muhammad, S. Murray, and J.O.W. Norris. *Compensation for surface contamination in a D-fiber evanescent wave methane sensor*, J. Lightwave Technol. **6**, 218-224 (1988)

[Kuw88]   M. Kuwazuru, Y. Namihira, K. Mochizuki, and Y. Iwamoto. *Estimation of long-term loss increase in silica-based opticcal fibers under hydrogen atmosphere*, J. Lightwave Technol. **Lt-3**, 1100-1104 (1985)

[Lee01]   S.T. Lee, P. Suresh Kumar, K.P. Unnikrishnan, V.P.N. Nampoori, C.P.G. Vallabhan, S. Sugunan, and P. Radhakrishnan. *Evanescent wave fibre optic sensors for trace analysis of Fe^{3+} in water*, Meas. Sci. Technol. **14**, 858-861 (2003)

[Lee03]   S.T. Lee S, N.A. George, P. Sureshkumar, P. Radhakrishnan, C.P.G. Vallabhan, and V.P.N. Nampoori. *Chemical sensing with microbent optical fiber*, Opt. Lett. **26**, 1541-1543 (2001)

[Lem91]   P.J. Lemaire. *Reliability of optical fibers exposed to hydrogen: prediction of long-term loss increases*, Opt. Eng. **30**, 780-789 (1991)

[Ler00]   T. von Lerber and A. Romann. *A method for measuring at least one physical parameter using an optical resonator.* European patent application No. 00121314.9 (9. Oct. 2000)

[Ler02₁] T. von Lerber and M. W. Sigrist. *Cavity-ring-down principle for fiber-optic resonators: experimental realization of bending loss and evanescent-field sensing*, Appl. Opt. **41**, 3567-3575 (2002)

[Ler02₂] T. von Lerber and M. W. Sigrist. *Time constant extraction from noisy cavity ring-down signals*, Chem. Phys. Lett. **353**, 131-137 (2002)

[Mar76]   D. Marcuse. *Curvature loss formula for optical fibers*, J. Opt. Soc. Am. **66**, 216-220 (1976)

[Mar81]   D. Marcuse. *Principles of optical fiber measurements*, Academic Press, New York (1981)

[Mit84]   Y. Mitsunaga, T. Kwabara, T. Abe, and Y. Ishida. *Molecular hydrogen behavior for loss increase of silica fiber in cable filled with water*, Electron. Lett. **19**, 917-919 (1984)

[Miu85]   K. Miura, M. Miyagi and S. Kawakami. *Study of vectorial properties of optical-fiber modes using a fiber resonator*, J. Lightwave Technol. **LT-3** , 361-367 (1985)

[Mon99]   T.M. Monro, D.J. Richardson, and P.J. Bennett. *Developing holey fibres for evanescent field devices*, Electron. Lett. **35**, 1188-1189 (1999)

[Mro01] J. L. (Armstrong) Mrotek, M.J. Matthewson, and C.R. Kurkjian. *Dif-fusion of moisture through optical fiber coatings*, J. Lightwave Technol. **19**, 988-993 (2001)

[Mur78] Y. Murakami and H. Tsuchiya. *Bending losses of coated single-mode optical fibers*, IEEE J. Quantum Electron. **14**, 495-501 (1978)

[Mur83] Y. Murakami, N. Uesugi, K. Noguchi, and Y. Mitsunaga. *Optical fiber loss increase in the infrared wavelength region induced by electric current*, Appl. Phys. Lett. **43**, 896-897 (1983)

[Nag78] K. Nagano, S. Kawakami, and S. Nishida. *Change of the refractive index in an optical fiber due to external forces*, Appl Opt **17**, 2080-2085 (1978)

[Ngu03] V.Q. Nguyen, J.S. Sanghera, P.C. Pureza, and I.D. Aggarwal. *Effect of heating on the optical loss in the As-Se glass fiber*, J. Lightwave Technol. **21**, 122-126 (2003)

[Nog83] K. Noguchi, Y. Murakami, and K. Ishihara. *Infra-red loss spectrum of hydrogen molecules in a silica fiber*, Electron. Lett. **19**, 1045-1046 (1983)

[Nog85] K. Noguchi, N. Shibata, N. Uesugi, and Y. Negishi. *Loss increase for optical fibers exposed to hydrogen atmosphere*, J. Lightwave Technol. **Lt-3**, 237-243 (1985)

[Ohm83] Y. Ohmori, H. Itoh, M. Nakahara, and N. Inagaki, *Loss increase in silicone-coated fibers with heat treatment*, Electron. Lett. **19**, 1006-1008 (1983)

[Oka03] S. Okazaki, H. Nakagawa, S. Asakura, Y. Tomiuchi, N. Tsuji, H. Murayama, and M. Washiya. *Sensing characteristics of an optical fiber sensor for hydrogen detection*, Sens. Actuators B **93**, 142-147 (2003)

[Pet81] S.J. Petuchowski, T.G. Giallorenzi, and S.K. Sheem, *A sensitive fiber-optic Fabry-Perot interferometer*, IEEE J. Quantum Electron. **QE-17**, 2168-2170 (1981)

[Pic004] G. Pickrell, W. Peng, and A. Wang. *Random-hole optical fiber evanescent-wave gas sensing*, Opt. Lett. **29**, 1476-1478 (2004)

[Pip97₁] A.C.R. Pipino, J.W. Hudgens, and R.E. Huie. *Evanescent wave cavity ring-down spectroscopy with a total-internal-reflection minicavity*, Rev. Sci. Instrum. **68**, 2978-2989 (1997)

[Pip97$_2$] A.C.R. Pipino, J.W. Hudgens, and R.E. Huie, *Evanescent wave cavity ring-down spectroscopy for probing surface processes*, Chem. Phys. Lett. **280**, 104-112 (1997)

[Pri59]   W. Primak and D. Post. *Photoelastic constants of vitreous silica and its elastic coefficient of refractive index*, J. Appl. Phys. **30**, 779-788 (1959)

[Rit04]   T. Ritari, J. Tuominen, H. Ludvigsen, J.C. Petersen, T. Sørensen, T.P. Hansen, and H.R. Simonsen. *Gas sensing using air-guiding photonic bandgap fibers*, Opt. Express **12**, 4080-4087 (2004)

[Rom99]   D. Romanini. *Cavity-ringdown spectroscopy versus intra-cavity laser absorption*, in: K.W. Busch, M.A. Busch, editors. *Cavity-ringdown spectroscopy*, ACS, Washington (1999)

[San94]   J.S. Sanghera, V.Q. Nguyen, P.C. Pureza, F.H. Kung, R. Miklos, and I.D. Aggarwal. *Fabrication of low-loss IR-transmitting $Ge_{30}As_{10}Se_{30}Te_{30}$ glass fibers*, J. Lightwave Technol. **12**, 737-741 (1994)

[Sar]   *Sartomer application bulletin, refractive index and product selection.* Sartomer Company Inc., Exton, PA (1999)

[Sch89]   Schwierz H. *Wellenausbreitung in gekrümmten ein- und zweiwelligen optischen Glasfaserleitungen mit beliebigem radialem Brechzahlprofilverlauf*, Ph.D. dissertation, Bergische Universität Wuppertal, Wuppertal (1989)

[Sha72]   J.F. Shackelford, P.L. Studt, and R.M. Fulrath. *Solubility of gases in glass. II. He, Ne, and H_2 in fused silica*, J. Appl. Phys. **43**, 1619-1626 (1972)

[She77]   J. E. Shelby. *Molecular diffusion and solubility of hydrogen isotopes in vitreous silica*, J. Appl. Phys. **48**, 3387-3394 (1977)

[Sor01]   T. Sørensen, J. Broeng, A. Bjarklev, E. Knudsen, and S.E. Barkou Libori. *Macro-bending loss properties of photonic crystal fibre*, Electron. Lett. **37**, 287-289 (2001)

[Ste01]   G. Stewart, K. Atherton, H. Yu, and B. Culshaw. *An investigation of an optical fibre amplifier loop for intra-cavity and ring-down cavity loss measurements*, Meas. Sci. Technol. **12**, 843-849 (2001)

[Sto82$_1$] L.F. Stokes, M. Chodorow, and H.J. Shaw. *All-single-mode fiber resonator*, Opt. Lett. **7**, 288-290 (1982)

[Sto82₂] J. Stone, A.R. Chraplyvy, and C.A. Burrus. *Gas-in-glass–a new Raman-gain medium: molecular hydrogen in solid-silica optical fibers*, Opt. Lett. **7**, 297-299 (1982)

[Sto] *Bend insensitive fiber, BIF-1550-L2, BIF-RC-1550-L2.* StockerYale Inc., Salem, NH (2003)

[Tan84] T. Tanifuji, M. Matsumoto, M. Tokuda, and M. Miyauchi. *Wavelength dependent optical loss increase in graded-index optical fiber transmission lines*, Electron. Lett. **20**, 13-14 (1984)

[Tar04₁] P.B. Tarsa, D.M. Brzozowski, P. Rabinowitz, and K.K. Lehmann. *Cavity ringdown strain gauge*, Opt. Lett. **29**, 1339-1341 (2004)

[Tar04₂] P.B. Tarsa, P. Rabinowitz, and K.K. Lehmann. *Evanescent field absorption in a passive optical fiber resonator using continuous-wave cavity ring-down spectroscopy*, Chem. Phys. Lett. **383**, 297-303 (2004).

[Ton03] Z. Tong, M. Jakubinek, A. Wright, Al Gillies, and H.P. Loock. *Fiber-loop ring-down spectroscopy: a sensitive absorption technique for small liquid samples*, Rev. Sci. Instrum. **74**, 4818-4826 (2003)

[Uch86] N. Uchida and N. Uesugi. *Infrared optical loss increase in silica fibers due to hydrogen*, J. Lightwave Technol. **Lt-4**, 1133-1138 (1986)

[Udd91] E. Udd. *Fiber optic sensors*, John Wiley & Son, New York (1991)

[Vil03] J. Villatoro, A. Diez, J.L. Cruz, and M.V. Andres. *In-line highly sensitive hydrogen sensor based on palladium-coated single-mode tapered fibers*, IEEE Sensors J. **3**, 533-537 (2003)

[Vil04] J. Villatoro, D. Monzon-Hernandez, and D. Luna-Moreno. *In-line optical fiber sensors based on cladded multimode tapered fibers*, Appl. Opt. **43**, 5933-5938 (2004)

[Vog03] D.E. Vogler, M. Müller, and M.W. Sigrist. *Fiber-optic cavity sensing of hydrogen diffusion*, Appl. Opt. **42**, 5413-5417 (2003)

[Vog05] D.E. Vogler, A. Lorencak, J.M. Rey, and M.W. Sigrist. *Bending loss measurement using fiber cavity ringdown scheme*, Opt. Lasers Eng. **43**, 527-535 (2005)

[Wan04₁] C. Wang and S.T. Scherrer. *Fiber ringdown pressure sensor*, Opt. Lett. **29**, 352-354 (2004)

[Wan04₂] C. Wang and S.T. Scherrer. *Fiber loop ringdown for physical sensor development: pressure sensor*, Appl. Opt. **43**, 6458-6464 (2004)

[Yos82] T. Yoshino, K. Kurosawa, K. Itoh, and T. Ose. *Fiber-optic Fabry-Perot Interferometer and its sensor applications*, IEEE J. Quantum Electron. **QE-18**, 1624-1632 (1982)

Appendix

[Dem03] W. Demtröder. *Laser spectroscopy*, Springer, Berlin (2003)

[Her65] D.R. Herriot and J.H. Schulte. *Folded optical delay lines*, Appl. Opt. **4**, 883-889 (1965)

[Whi42] J.U. White. *Long paths of large aperture*, J. Opt. Soc. Am. **32**, 285-288 (1942)

Acknowledgements

Michel Müller, Ana Lorencak, Peter Kaspar and Ian Norris supervised students for contributing to the completion of this thesis with their excellent works.

The physics department at the Swiss Federal Institute of Technology for the support of my thesis and ASVZ for offering such a diversity of sweaty sports.

My two brothers, Roger and Iwan, and all friends for supporting me at some stressful days and for the great time in Zurich and in Obwalden.

Thank you very much!

What a wonderful world !

List of Publications and Presentations

All publications, talks and conference contributions resulted from the Ph.D. study are listed below.

Refereed journals

J. M. Rey, D. Marinov, D. E. Vogler, and M. W. Sigrist. *Investigation and optimisation of a multipass resonant photoacoustic cell at high absorption levels*, Appl. Phys. B **80**, 261-266 (2005)

D. E. Vogler, A. Lorencak, J. M. Rey, and M. W. Sigrist. *Bending loss measurement using fiber cavity ringdown scheme*, Opt. Lasers Eng. **43**, 527-535 (2005)

D. E. Vogler, M. Müller, and M. W. Sigrist. *Fiber-optic cavity sensing of hydrogen diffusion*, Appl. Opt. **42**, 5413-5417 (2003)

Invited talk

D. E. Vogler and M. W. Sigrist. *Fiber optical cavity sensor*, ABB Corporate Research Ltd., Baden-Daettwil (CH), July 10 (2003)

Conference proceedings and abstracts

D. E. Vogler and M. W. Sigrist. *Trace gas sensing using near-infrared cavity ringdown spectroscopy*, Dig. SPG Meeting, Paper 232, Bern (CH), July 14-15 (2005)

D. E. Vogler, H. Wächter, and M. W. Sigrist. *Cavity ringdown spectroscopy for petrochemical process monitoring*, Dig. CLEO-Europe 2005, Paper CH2-2-THU, Munich (D), June 12-17 (2005)

D. E. Vogler and M. W. Sigrist. *Cavity ringdown technique in fibers*, Dig. CLEO 2004, Paper CMN-510, San Francisco (US), May 16-21 (2004)

D. E. Vogler and M. W. Sigrist. *Fiber cavity ringdown technique: A novel promising method for sensitive loss measurements ?*, Dig. SPG Meeting,Paper 236, Neuchâtel (CH), March 3-4 (2004)

D. E. Vogler and M. W. Sigrist. *Fiber optical cavity monitoring of hydrogen diffusion*, Dig. CLEO-Europe 2003, Paper CI5-4-WED, Munich (D), June 22-27 (2003)

D. E. Vogler and M. W. Sigrist. *Fiber optical cavity sensor*, Dig. SPG Meeting, Paper 224, Basel (CH), March 20-21 (2003)

Contributed oral presentations at conferences

D. E. Vogler, H. Wächter, and M. W. Sigrist. *Cavity ringdown spectroscopy for petrochemical process monitoring*, Dig. CLEO-Europe 2005, Munich (D), June 12-17 (2005)

D. E. Vogler and M. W. Sigrist. *Cavity ringdown technique in fibers*, Dig. CLEO 2004, San Francisco (US), May 16-21 (2004)

C. Fischer, D. Marinov, J. M. Rey, D. E. Vogler, H. Wächter, and M. W. Sigrist. *Laser spectroscopy in sensing applications*, Optical Science Mini-Symposium, ETH Zurich, March 17 (2004)

D. E. Vogler and M. W. Sigrist. *Fiber cavity ringdown technique: A novel promising method for sensitive loss measurements ?*, Dig. SPG Meeting, Neuchâtel (CH), March 3-4 (2004)

D. E. Vogler and M. W. Sigrist. *Fiber optical cavity monitoring of hydrogen diffusion*, Dig. CLEO-Europe 2003, Munich (D), June 22-27 (2003)

D. E. Vogler and M. W. Sigrist. *Fiber optical cavity sensor*, Dig. SPG Meeting, Basel (CH), March 20-21 (2003)

Poster contributions at conferences

D. E. Vogler and M. W. Sigrist. *Trace gas sensing using near-infrared cavity ringdown spectroscopy*, Dig. SPG Meeting, Bern (CH), July 14-15 (2005)

D. E. Vogler, H. Wächter, and M. W. Sigrist. *Near-infrared cavity ringdown spectroscopy for industrial process monitoring applications*, 4rd CRDS User Meeting, Heeze (NL), October 7-8 (2004)

D. E. Vogler. *Fiber cavity ringdown technique*, 3rd CRDS User Meeting, Lille (F), October 10 (2003)

Student Supervisions

All students supervised during this Ph.D. study are listed below.

Supervised diploma students

Ian Norris   *Cavity ringdown spectroscopy*, June - August (2003)

Ana Lorencak *Krümmungsverluste in Faserkavitäten*, November - March (2002/2003)

Supervised semester students

Peter Kaspar   *Wavelength-dependence of bending loss in a fiber cavity*, March (2003)

Michel Müller   *Wasserstoff induzierter optischer Verlust in Faserkavitäten*, August (2002)

Curriculum Vitae

Personal data

Name	Daniel Edgar Vogler
Date of birth	27th February 1975
Citizen	Lungern (Obwalden)
Nationality	Swiss

Education

Nov. 2005	Ph.D. examination (Dr. sc. nat.) at the Swiss Federal Institute of Technology (ETH) in Zurich. *Open-path and fiber-based Cavity Ringdown Spectroscopy* accepted on the recommendation of Prof. Dr. Markus W. Sigrist (examiner), Prof. Dr. Ursula Keller (co-examiner), and Dr. Hubert Brändle (co-examiner)
2001 - 2005	Ph.D. study in the Laser Spectroscopy and Sensing Group of Prof. Dr. Markus W. Sigrist at the ETH Zurich
Aug. 2001	Graduation (Dipl. Phys. ETH) at the Swiss Federal Institute of Technology (ETH) in Zurich
1996 - 2001	Study of experimental physics with main emphasis in quantum electronics at the ETH Zurich
	Diploma thesis in the Photonic Communication Group of Prof. Dr. Georg Guekos (emerit.) at the Institute of Quantum Electronics (IQE) under the supervision of Dr. Laurent Schares. *Dynamische Untersuchungen des 'Ultrafast Nonlinear Interferometer' bei 10 GHz*
June 1995	Matura Typus B
1988 - 1995	High school Kantonsschule Obwalden in Sarnen OW (Switzerland)

Professional experiences

2001 - 2005   Research and teaching assistant at the ETH in Zurich
1995 - 1996   Employment at PAT Messtechnik AG in Giswil OW (Switzerland)

Further education

2001 - 2005   Höheres Lehramt, ETH Zurich
2005   Language course at the Milner International College of English in Perth (Australia): Certificate in Advanced English (CAE), Business English Certificate (BEC Vantage)
2005   Course in basic management skills, ETH Zurich
2003   Course in project management, ETH Zurich

University activities

2003 - 2005   Representative of the Institute of Quantum Electronics assistants at the Physics Department Conference
2002 - 2003   Supervisor of different semester and diploma students

Military activities

2002   Promotion to Wachtmeister
1996   Promotion to Korporal
1996   Uem/Na UOS/RS 13 in Fribourg
1995   Uem/Na RS 213 in Fribourg

Memberships

Swiss Physical Society (SPS)
Swiss Society of Optics and Microscopy (SSOM)
ALUMNI ETH Zurich

Zurich, November 2005

Daniel E. Vogler